UC Irvine
UC Irvine Electronic Theses and Dissertations

Title
Investigation of Novel Laser Treatments for Glaucoma and Meibomian Gland Dysfunction

Permalink
https://escholarship.org/uc/item/4dk1v6g8

Author
Luo, Shangbang

Publication Date
2023

Peer reviewed|Thesis/dissertation

eScholarship.org Powered by the California Digital Library
University of California

UNIVERSITY OF CALIFORNIA,
IRVINE

Investigation of Novel Laser Treatments for Glaucoma and Meibomian Gland Dysfunction

DISSERTATION

submitted in partial satisfaction of the requirements
for the degree of

DOCTOR OF PHILOSOPHY

in Biomedical Engineering

by

Shangbang Luo

Dissertation Committee:
Professor Tibor Juhasz, Chair
Professor James V. Jester
Professor Liangzhong Xiang

2023

Chapter 3 © 2022 Optica Publishing Group
All other materials © 2023 Shangbang Luo

TABLE OF CONTENTS

LIST OF FIGURES

LIST OF TABLES

ACKNOWLEDGEMENTS

I would like to express my deepest gratitude to my advisor, Professor Tibor Juhasz, who always supported me during my PhD study on femtosecond laser trabeculotomy and OCT imaging. Without his guidance and persistent help, this dissertation would not have been possible.

I would like to thank Professor James Jester, with whom I have been working on meibomian gland dysfunction. We have spent hours and hours modeling meibum secretion and trying to use laser treatment for meibomian gland dysfunction. Also, thanks to Dr. Gagik P. Djotyan from the Institute for Particle & Nuclear Physics, Wigner Research Center, Budapest, Hungary, for his suggestions in meibum secretion modeling.

In addition, thank you to Professor Donald Brown, who introduced me to anything that I didn't know in the field of biology. He also provided some engineering ideas on how to make custom-built tools for different eye experiments.

I'd also like to thank Professor Liangzhong (Shawn) Xiang for reviewing my thesis and invaluable suggestions for my thesis.

My lab mates were also indispensable in this work. Dr. Eric Mikula spent hundreds of hours showing me how to prepare human cadaver eyes and conduct eye surgery experiments, and he was always willing to teach me all he knew. Mr. Guy Holland spent hours and hours with me on OCT image processing and the surgical system, some LabView coding, or even suggested how to buy benchtop optical blocks. Dr. Reza Khazaeinezhad always helped me with the surgical system. Our postdoc, Dr. Samantha Bradford, helped me with tissue sectioning, confocal imaging, and different eye experiments. Mr. Rohan Joshi helped with eye experiments. Yilu Xie was always willing to help me with section samples. Emily taught me how to perform different stains and fluorescent imaging, and cell cultures. Dr. Jung Su b Kim, our recent postdoc, spent hours teaching me how to do statistics for scientific data.

Chapter 3 of this dissertation is published material as it appears in Optica Continuum [1], used with permission from Optica Publishing Group. The co-authors listed in this publication are Guy Holland, Eric Mikula, Samantha Bradford, Reza Khazaeinezhad, James V. Jester, and Tibor Juhasz.

Lastly, the following grants are gratefully acknowledged: NIH/NEI R01EY030304 (TJ), NIH/NEI R01EY021510 (JVJ), NIH/NEI P30EY034070, Discovery Eye Foundation, an unrestricted Grant from Research to Prevent Blindness, Inc. (RPB-203478), Skirball Program in Molecular Ophthalmology and Basic Science, and the Student Research Grant from the American Society for Laser Medicine and Surgery, Inc. (S0123).

VITA

Shangbang Luo

2018-19	Graduate Student Researcher, Department of Biomedical Engineering, University of California, Irvine
2019	Teaching Assistant, Department of Biomedical Engineering, University of California, Irvine
2019-23	Graduate Student Researcher, Department of Ophthalmology and Department of Biomedical Engineering University of California, Irvine
2023	Ph.D. in Biomedical Engineering, University of California, Irvine

FIELD OF STUDY

Femtosecond laser trabeculotomy for glaucoma treatment, optical coherence tomography, meibomian gland dysfunction

PUBLICATIONS

Samantha Bradford, **Shangbang Luo**, Donald Brown, Tibor Juhasz, James Jester, "A review of the epithelial and stromal effects of corneal collagen crosslinking", The Ocular Surface, **30**: 150-159 (2023)

Shangbang Luo, Guy Holland, Reza Khazaeinezhad, Samantha Bradford, Rohan Joshi, Tibor Juhasz, "Iridocorneal angle imaging of a human donor eye by spectral-domain optical coherence tomography", Sci Rep **13**, 13861 (2023). https://doi.org/10.1038/s41598-023-37248-0

Shangbang Luo, Guy Holland, Eric Mikula, Samantha Bradford, Reza Khazaeinezhad, James V. Jester, Tibor Juhasz, "Dispersion compensation for spectral domain optical coherence tomography by time-frequency analysis and iterative optimization", Opt. Continuum **1**(5): 1117-1136 (2022)

CONFERENCES

Shangbang Luo, Eric R. Mikula, Samantha Bradford, Rohan Joshi, Fengyi Zhang, Emily Farrah, Yilu Xie, Donald J. Brown, James V. Jester, Zhongping Chen, Tibor Juhasz, "Evaluating

the Effect of Pulse Energy on Femtosecond Laser Trabeculotomy (FLT) Drainage Channels in Human Cadaver Eyes", ARVO 2023 abstract

Eric R. Mikula, Gagik Djotyan, **Shangbang Luo**, James V. Jester, Tibor Juhasz, "Femtosecond Laser Image Guided High-precision Trabeculotomy (FLigHT): a thermal collateral damage study", ARVO 2023 abstract

Samantha Bradford, Rohan Joshi, **Shangbang Luo**, Emily Farrah, Yilu Xie, Donald J. Brown, Tibor Juhasz, James V. Jester, "In Vivo Femtosecond Laser Machined Transepithelial Nonlinear Optical Corneal Crosslinking Compared to In Vivo Femtosecond Laser Machined Transepithelial Ultraviolet Corneal Crosslinking", ARVO 2023 abstract

Rohan Joshi, Samantha Bradford, **Shangbang Luo**, Emily Farrah, Yilu Xie, Donald J. Brown, Tibor Juhasz, James V. Jester, "Enhanced Riboflavin Stromal Delivery Using Microchannel-assisted Iontophoresis for Corneal Crosslinking (CXL)", ARVO 2023 abstract

ABSTRACT OF THE DISSERTATION

Investigation of Novel Laser Treatments for Glaucoma and Meibomian Gland Dysfunction

by

Shangbang Luo

Doctor of Philosophy in Biomedical Engineering

University of California, Irvine, 2023

Professor Tibor Juhasz, Chair

This thesis provides a comprehensive summary of my PhD studies, investigating the potential application of diverse laser technologies in treating two prevalent eye conditions: glaucoma and meibomian gland dysfunction (MGD).

Glaucoma is the leading cause of irreversible blindness affecting approximately 80 million individuals worldwide. We explored the use of femtosecond lasers for precise photodisruption of the trabecular meshwork, a vital surgical region within the human eye. The dissertation begins with an examination of the optimization of pulse energy levels in femtosecond laser trabeculoplasty (FLT), enhancing its effectiveness as a treatment for glaucoma. Additionally, the temperature variations observed during FLT surgeries and evaluation of potential collateral damage in human cadaver eyes have been investigated. To enhance targeting precision in surgical interventions, we have developed a micron-scale spectral domain optical coherence tomography system tailored for iridocorneal angle imaging. The thesis highlights the use of short-time Fourier transform to compensate for dispersion, a crucial step in achieving superior axial resolution. Moreover, advanced imaging

processing techniques and hardware implementations are presented to demonstrate the comprehensive and detailed visualization of the surgical area within the angle.

In the second part of the dissertation, attention is shifted towards our research endeavors focused on addressing MGD. Firstly, methods leveraging numerical modeling and analytical derivations are discussed, shedding light on alternative mechanisms underlying the development of obstructive MGD. Additionally, an innovative treatment approach called selective photothermal ablation (SPA) is introduced, showcasing its potential in selectively targeting the meibomian glands while preserving the overlying conjunctival integrity.

Introduction

Glaucoma, Ocular Outflow Pathways, and Iridocorneal Angle

Glaucoma is the leading cause of irreversible blindness and is responsible for the second most common cause of visual loss in the world. Approximately 64.3 million people worldwide were affected in 2013, and this number is estimated to increase from 76.0 million in 2020 to 111.8 million in 2040 [2]. Glaucoma is a neuropathic disease characterized by optic nerve damage or optic disc cupping and is indicated by high intraocular pressure (IOP), which is caused by increased resistance to the normal outflow of aqueous humor (AH) from the eye [3].

The AH, secreted by the ciliary body, drains into the posterior chamber, then travels through the pupil into the anterior chamber (AC). At the iridocorneal angle (ICA), where the iris and cornea meet, the AH exits the eye through two different outflow pathways: conventional and uveoscleral outflow pathways (Fig. 0.1). Only 10% of the AH flows to the ciliary body surface and iris root, toward the surrounding veins and tissues in the uveoscleral outflow pathway [4]. The majority of the remaining AH fluid passes through the trabecular meshwork (TM) into Schlemm's canal (SC) (Fig. 0.2). From there, the fluid drains into a series of collector channels (CCs) and is finally absorbed by the episcleral veins [5].

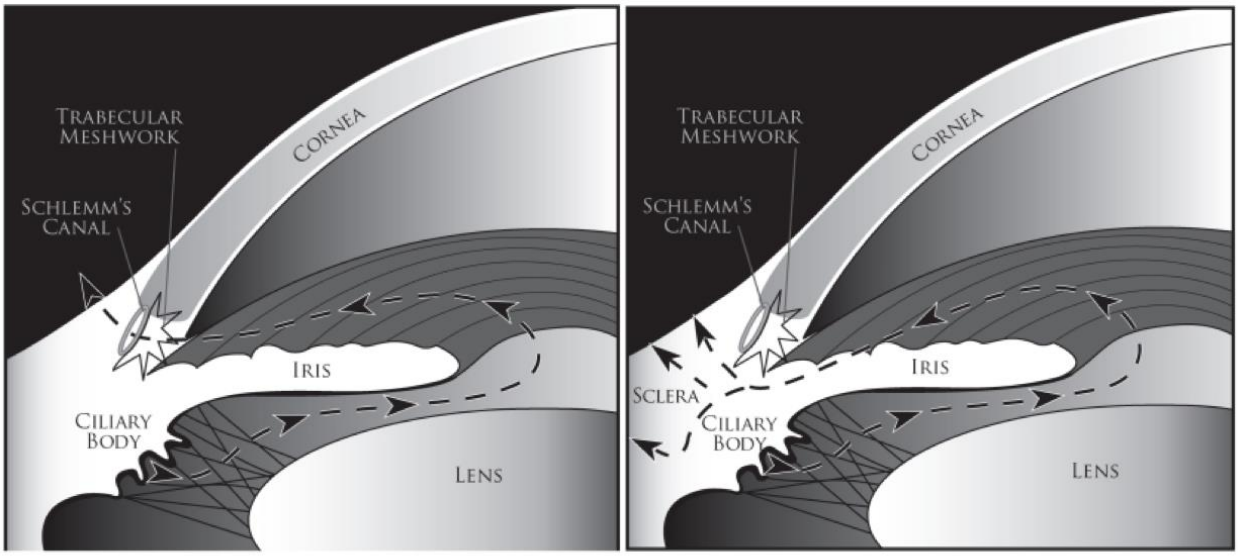

(a) conventional outflow pathway (b) uveoscleral outflow pathway

Figure 0.1: Schematic illustrating the ocular outflow pathways. Aqueous humor passes through (A) the conventional and (B) the uveoscleral outflow pathways [4].

The TM is a porous, sieve-like structure consisting of laminar beams located in the inner portion of the scleral sulcus, a groove that encircles the ICA. The TM comprises three distinct layers, from the innermost uveal layer to the corneoscleral layer, culminating in the outermost juxtacanalicular tissue (JCT) (Fig. 0.2). The SC is an adjoining, endothelium-lined, lymphatic-like circular channel situated in the outer part of the scleral sulcus [6]. Studies have found that the JCT and the inner wall of the SC are the major sources of proximal outflow resistance, leading to an increase in IOP and can cause harm to the optic nerve in the retina [5]. Typically, each human eye contains 20 to 30 CCs with an average diameter of 30 μm, although there are significant variations among them [7].

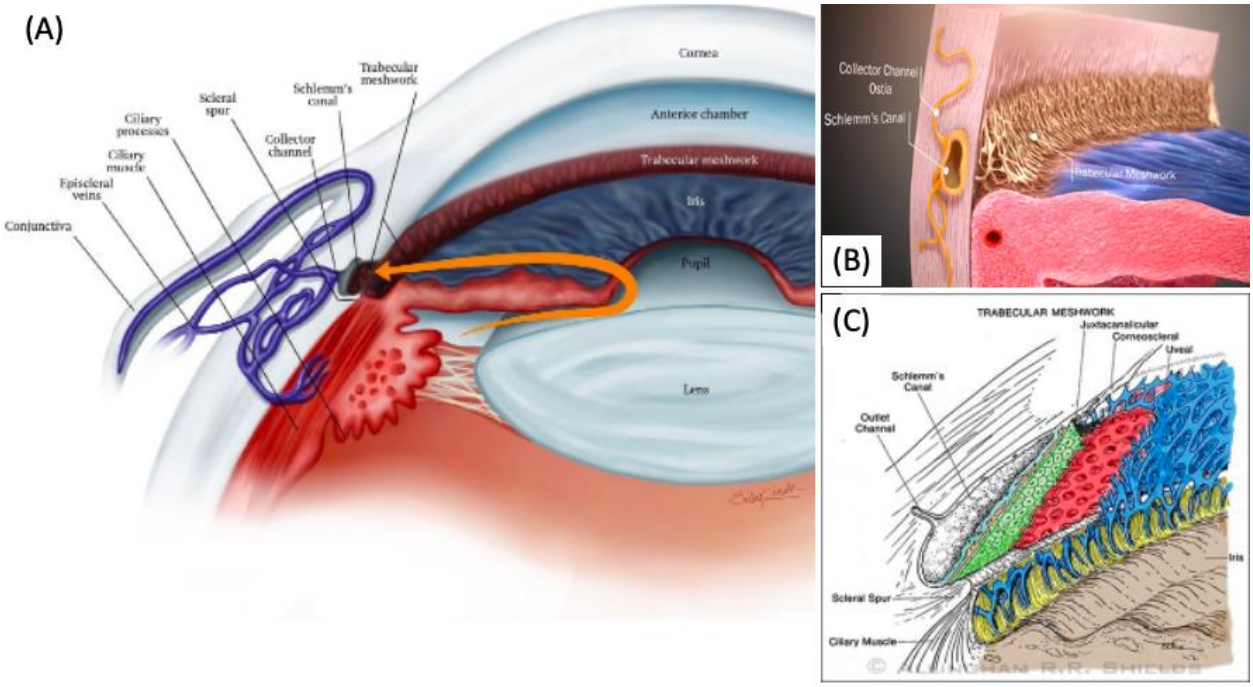

Figure 0.2: Schematic of the iridocorneal angle [8]. (A) Depicts the trabecular meshwork, Schlemm's canal, and collector channels at the iridocorneal angle, while (B) offers a closer view of these structures. (C) Demonstrates the three layers of the trabecular meshwork, progressing from the innermost uveal layer (depicted in blue) to the corneoscleral layer (depicted in red), with the outermost layer being the juxtacanalicular tissue (depicted in green).

Motivation for Glaucoma Treatment

The only modifiable risk factor for glaucoma treatment is to reduce intraocular pressure or IOP, either by decreasing the production of aqueous humor (AH) or increasing its outflow using medications, laser therapy, conventional surgery, or minimally invasive glaucoma surgery (MIGS). However, these approaches all have limitations, including issues with patient compliance, reduced or short-term efficacy, and invasiveness. This report explores a completely non-invasive, non-incisional surgery termed femtosecond laser trabeculotomy (FLT) for the treatment of glaucoma.

Different Glaucoma Surgeries

Current Managements for Glaucoma Treatment:

Topical drugs are usually the first choice in managing glaucoma, aiming to reduce IOP by increasing outflow facility and/or decreasing the production of AH from the ciliary body [9]. There are five categories of IOP-lowering drugs for glaucoma treatment: prostaglandin analogues, β-blockers, diuretics, cholinergic agonists, and α-agonists. Among these, prostaglandin analogues are the most widely used drugs. Although many anti-glaucoma medications are available, currently, there is no drug that specifically targets impaired trabecular outflow, which is the most common pathogenic cause of elevated IOP [9]. Other major challenges in pharmacological treatment include patient compliance issues [10, 11], reduced efficacy over time [9], uncontrolled IOP [9, 12] and adverse effects such as corneal diseases, conjunctival scarring, and reduced cardiac and pulmonary function [13-15].

Argon laser trabeculoplasty (ALT), which was studied in the 1970s, was the first laser treatment modality for glaucoma [16, 17]. It employs a continuous-wave Argon laser with a 50-μm beam diameter to deliver burns of 1,000 to 1,500 milliwatts to the TM in a 360-degree pattern over 0.1 seconds [17]. This process causes tissue heating, scarring, and contraction. The photocoagulation damage to the TM results in the stretching of adjacent tissues, thereby improving the outflow rate of AH [17-20]. Complementary theories [21] suggest that mechanical changes in the trabecular ring [22], induced phagocytosis [18], increased cell division [23-26], and TM repopulation [23, 27] all contribute to structural changes in the TM, leading to improved outflow. However, various studies have reported that the heating and coagulation effects can lead to the formation of a cellular membrane that covers the TM, potentially obstructing outflow and leading to a frequent failure of glaucoma treatment [28-

31]. Some reports have shown a 68% failure rate of ALT retreatment with uncontrolled IOP [31], and a success rate of 44% at 2 years after treatment [32]. Drawbacks also include IOP spikes [33, 34], inflammation [35], peripheral anterior synechiae [33, 36, 37], and decreased efficacy over time [38, 39]. Although ALT has demonstrated its efficacy in multicenter clinical studies [32, 40], its usage has decreased significantly due to the growing popularity of selective laser trabeculoplasty (SLT) [41, 42].

SLT is a noninvasive and repeatable glaucoma treatment invented by Latina et al. in 1998 [41, 42]. It employs a frequency-doubled Q-switched 532-nm Neodymium:YAG laser to deliver pulses with an energy range of 0.6 to 1.2 mJ, a spot size of 400 μm, and a duration of 3 ns over 180 degrees of the TM [42]. SLT's mechanism is based on the selective photothermolysis theory [43], wherein the laser selectively targets pigmented trabecular cells, and the pulse duration is shorter than the thermal relaxation time to minimize adjacent tissue damage [41, 42, 44]. Biologically, SLT leads to the release of cytokines that bind to and regulate the permeability of Schlemm's canal's endothelial cells [45, 46], an increased recruitment of monocytes that develop into phagocytes, clearing the obstructed meshwork at the laser burn sites [47], and induction of matrix metalloproteinases responsible for remodeling the extracellular matrix, thereby increasing outflow conductivity [48]. Using short-duration, low-energy pulses compared to ALT, SLT is believed to avoid coagulative necrosis in the TM [44], making SLT treatments safe and repeatable [42, 44, 49-53]. However, Cvenkal et al. reported comparable disruptive damages after ALT and SLT, with the latter causing slightly smaller damaged trabecular tissues and better preservation of endothelial cells and long-spacing collagens [54]. The long-term success rates were similar for ALT and SLT, both requiring further medical or surgical intervention [55]. Additionally,

the efficacy of SLT diminishes over time [56, 57]. Reported adverse events include transient elevated IOP, iritis, hyphemia, macular edema, corneal complications, and peripheral anterior synechiae [58].

As the last line of treatment, conventional filtration surgeries, such as trabeculectomy and glaucoma drainage implants, are used for moderate to advanced glaucoma patients. Trabeculectomy is a surgical operation that creates a channel in the TM and SC area as underneath the scleral tissue and sutures back the scleral flap. AH flows via this new route and drains into a filtering bleb underneath the conjunctiva. For drainage implants, such as the Baerveldt shunt (Abbott Medical Optics, Inc., Santa Ana, California), is used to divert AH fluid from the anterior chamber (AC) to an external reservoir. Given the invasive nature of filtration surgery, careful consideration should be given to the decision between surgical benefits and risks. Filtration surgeries are highly invasive, complicated, and have a failure rate around 50% at 5 years and are associated with a host of complications such as hypotony (24%), flat AC (24%), hyphema (25%), and bleb leak (18%) [59-63].

To bridge the gap between medical/laser treatments and more invasive surgeries like trabeculectomy or drainage implants, a new management option, typically aimed at patients with mild to moderate glaucoma, has emerged in recent years. This approach is known as minimally invasive glaucoma surgery (MIGS). While there is a variety of MIGS devices available, they can generally be categorized into three main groups based on their target routes: subconjunctival, Schlemm's canal, and suprachoroidal space [64] (Fig. 0.3). However, they all share a common drawback, which requires opening the eye to either insert surgical instrumentation or an implant.

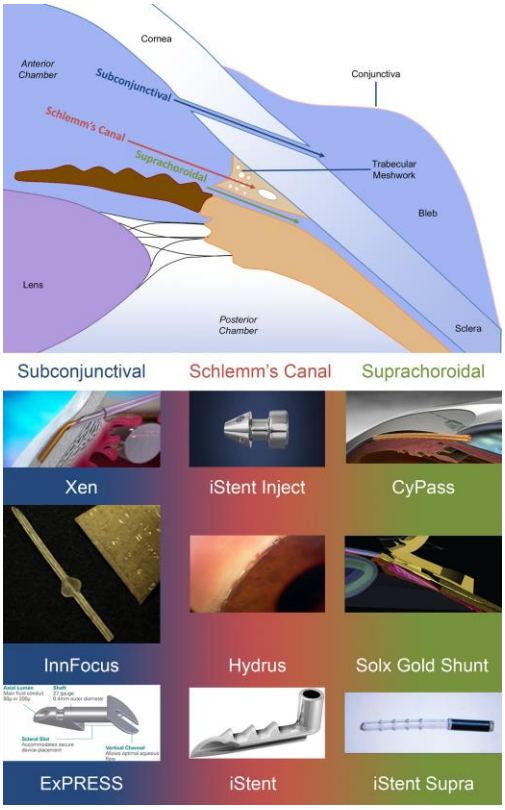

Figure 0.3: Schematic of the potential aqueous outflow routes following the implantation of minimally invasive glaucoma surgery devices [64].

MIGS devices that target the Schlemm's canal route include the Hydrus microstent (Ivantis Inc., Irvine, CA, USA), iStent or iStent Inject (Glaukos Inc., Laguna Hills, CA, USA), trabectome (MST, Redmond, WA), and excimer laser trabeculotomy (ELT). The iStent or iStent Inject is a tiny drainage device used to bypass outflow pathways through the TM, allowing AH to flow from the AC into the SC. A Hydrus microstent is typically inserted into the TM and scaffolds 90° of the SC through a preloaded stainless-steel cannula via a clear cornea incision. Trabectome is generally considered a MIGS procedure that employs a customized electrocautery device through a 1.6 mm corneal incision to remove a strip of TM along with the SC. While it boasts a high success rate, MIGS implants require an invasive corneal incision and are therefore primarily indicated for use in conjunction with cataract surgery. ELT uses a 308 nm Xenon Chloride excimer laser to ablate the TM through a

corneoscleral incision via a thin quartz probe. By moving the probe, a series of drainage holes are created to facilitate aqueous outflow into the SC, resulting in a significant decrease in IOP. Although the ELT procedure operates in the ultraviolet range and minimizes thermal damage to surrounding tissues, the corneal incision remains invasive.

In summary, while a range of strategies for glaucoma treatment is available, all these procedures have shortcomings, including limited longevity (SLT, ALT), a high complication rate (filtration surgery), invasiveness (filtration surgery, MIGS), indication primarily in conjunction with cataract surgery (MIGS), a lack of precise IOP control (SLT, ALT), and associated high medication costs alongside these procedures.

Femtosecond Laser Trabeculotomy (FLT):

The first portion of this thesis (Chapters 1 to 4) focuses on the optimization of pulse energy for FLT, the collateral damage associated with FLT, and the improvement of OCT imaging of the iridocorneal angle for FLT.

FLT is a novel innovative approach non-invasively establishes a conduit between the anterior chamber (AC) and Schlemm's canal (SC), thus providing an unobstructed aqueous humor outflow channel. The use of femtosecond lasers to perform trabeculotomy enables dynamic delivery of tightly focused laser pulses through the cornea, across the anterior chamber, photodrsrupting the trabecular meshwork into SC [65-68].

The use of a femtosecond laser for glaucoma treatment has several advantages. Firstly, a tightly focused femtosecond laser enables photodisruption to occur only at a well-defined focal spot, resulting in localized and confined tissue removal [69]. Secondly, the pulse duration and plasma expansion time associated with femtosecond lasers is shorter than the

local thermal diffusion time, leading to limited thermal damage [70]. Lastly, experimental studies on human ocular tissues have demonstrated that femtosecond lasers produce reduced shock wave and cavitation bubble effects compared to lasers with longer pulse durations, resulting in further localized tissue damage [69]. These favorable properties, coupled with the ability to non-invasively deliver the laser pulse and the precise scanning and delivery control enabled by modern computer systems, make femtosecond lasers an ideal technique for trabecular bypass surgery. Furthermore, the safety and efficacy of femtosecond laser have been demonstrated over the last twenty years for various procedures, including flap creation in corneal refractive surgery, capsulotomy, lens fragmentation, and corneal incisions during cataract surgery [71-74].

The underlying mechanism of using femtosecond lasers to create channels in the trabecular meshwork tissues can be described by the phenomenon called laser-induced optical breakdown (LIOB) [65]. During the LIOB process, the extremely focused and narrow laser pulse generates a high-intensity local electric field that strips valence electrons from atoms, creating a mixture of electrons and ions, or plasmas, in tissues. These plasmas then expand and stretch the adjacent tissues with supersonic velocity. As the temperature decreases, the plasma expansion slows down, and the supersonic displacement wavefront continues to propagate throughout the tissues as a shock wave. This shock wave ultimately transforms into a normal acoustic wave, dissipating in the surrounding tissues. Since the expansion duration of the plasma is much shorter than the local thermal relaxation time, thermal damage is localized, thus avoiding collateral damage to the surrounding tissues. As the plasma cools down during the entire process, cavitation bubbles are formed and diffuse throughout the tissues (Fig. 0.4).

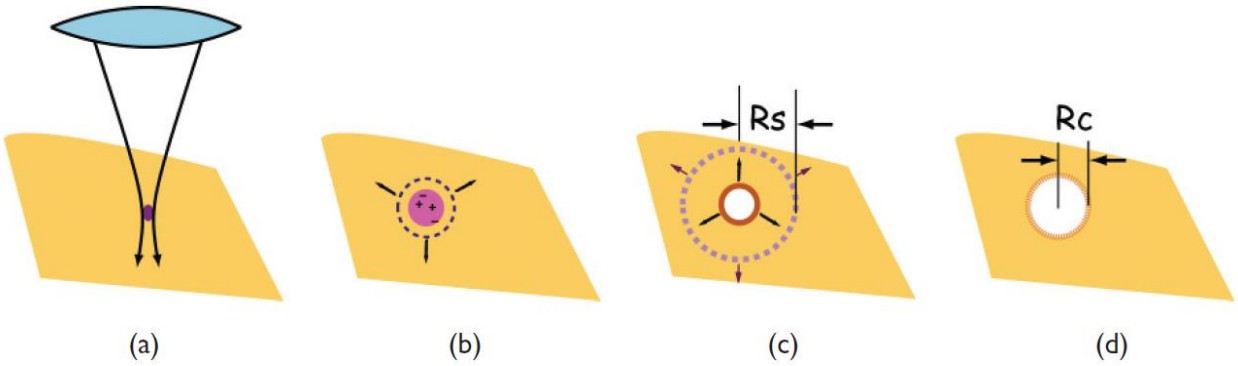

Figure 0.4: Principle of laser-induced optical breakdown [70]. (a) A focused laser pulse travels through the tissue with intensity calibrated to trigger optical breakdown only at the beam's focal point. (b) Optical breakdown generates a high-density plasma that rapidly expands outward at supersonic speeds, forming a shock wave at its leading edge. (c) The rapidly cooling plasma condenses, creating an expanding cavitation gas bubble. (d) The cavitation bubble reaches its maximum size, subsequently collapses and rebounds. Eventually, a small, stationary bubble remains for a brief duration. Rs represents the radial distance at which the velocity of the shock wave propagation slows to typical acoustic wave speeds, while "Rc" denotes the maximum radius of the cavitation bubble.

Selective Photothermal Ablation (SPA) for Meibomian Gland Dysfunction (MGD)

The second part of this thesis, comprising Chapters 5 and 6, centers on the exploration of novel alternative mechanisms underlying obstructive MGD and introduces a new treatment method, called selective photothermal ablation (SPA), for MGD treatment.

Meibomian gland dysfunction (MGD) is a chronic and diffuse condition affecting the meibomian glands, typically identified by obstructions in the terminal ducts and alterations in the quality or quantity of glandular secretions [75]. Obstructive MGD can lead to signs and symptoms of dry eye disease (DED); a common disorder characterized by burning of the eye and blurry vision related to tear film abnormalities, increased tear evaporation, and ocular surface inflammation [76]. It is estimated that more than 16 million US adults have DED, with an annual cost of $55.4 billion [77, 78].

Traditional management techniques for MGD-related dry eye include warm compresses, eyelid hygiene, meibomian gland expression, and pharmacotherapy [79-96]. While drug-based treatments for MGD can be effective, they require patient compliance and pose potential side effects. Additionally, hot compresses, eyelid washes, and meibum expression, although easy to perform, either require patient compliance or lack long-term efficacy. This collective evidence suggests the need for alternative methods to treat this disease.

Recent efforts have focused on the study of applying novel laser-based therapies for dry eye caused by MGD. For example, intense pulsed light (IPL) therapy uses a broadband light source covering wavelengths from 500 to 1200 nm, which is delivered to the periocular surface, causing thermal effects on the irradiated tissue and inducing blood vessel ablation and meibum melting [97-121]. Low-level light therapy (LLLT), also referred to as photobiomodulation, uses red or near-infrared light irradiation from lasers or light-emitting diodes on both closed lids and the periorbital area, with the use of eye shields either in-office or at home [122-125]. It has been shown to be effective in treating dry eye syndromes [122-124]. Additionally, a combined IPL/LLLT therapy has been introduced, where IPL is first performed on the lower periorbital area, followed by LLLT over both the closed lids and periorbital area [126-134]. While all these approaches have been found to be effective and safe, the long-term treatment efficacy remains unknown and controversial, and there is a lack of standardization. Therefore, more standardized, large sample, randomized, multi-centered clinical trials are needed. Additionally, one potential concern in designing a broadband laser source is that it can induce comparable photothermal effects on the surrounding tissue as well, leading to undesirable outcomes.

This indiscriminate tissue damage problem is attributed to its wide spectral range and can be solved by using a relatively narrow bandwidth laser tuned to a local absorption peak, which separates the heating effect between the target and the surrounding tissue to the largest extent. Such a laser can result in preferential or selective damage to the target with minimal insult to adjacent tissues.

In this study, a novel narrow bandwidth surgical 1726 nm laser was introduced for the feasibility study of selective photothermal ablation (SPA) for the treatment of dry eye due to MGD. Ex-vivo mice eyelids were used for the SPA treatment, and different imaging modalities, such as H&E and fluorescent imaging, were used to verify the proposed method. Our results indicate that SPA can be a promising treatment for MGD, but future in-vivo studies are needed.

Chapter 1: Pulse Energy Optimization on FLT

Introduction

The first part of my dissertation (Chapters 1 to 4) aims to explore the use of femtosecond lasers for the treatment of glaucoma. The initial key question is what constitutes a suitable pulse energy for femtosecond laser trabeculotomy (FLT) – a completely non-invasive, non-incisional glaucoma surgery developed in our group. In this chapter, we will establish a methodology for conducting laser tissue cutting experiments using human cadaver eyes. The optimization of pulse energy for FLT is determined by the quality of the outflow channels created, as assessed by OCT imaging.

Materials and Methods

FLT Delivery System:

The FLT system consists of several components, including a femtosecond laser, a gonioscopic camera, a low power HeNe aiming laser, and a series of optics, as depicted in Fig. 1.1. For our experiments, we utilized a commercial amplified diode pumped Ytterbium-based femtosecond laser (Origami-10XP Femtosecond Laser, NKT Photonics, Denmark). This laser emits pulses with a duration of 400 fs, a wavelength of 1.03 μm, and a pulse repetition frequency of 10 kHz.

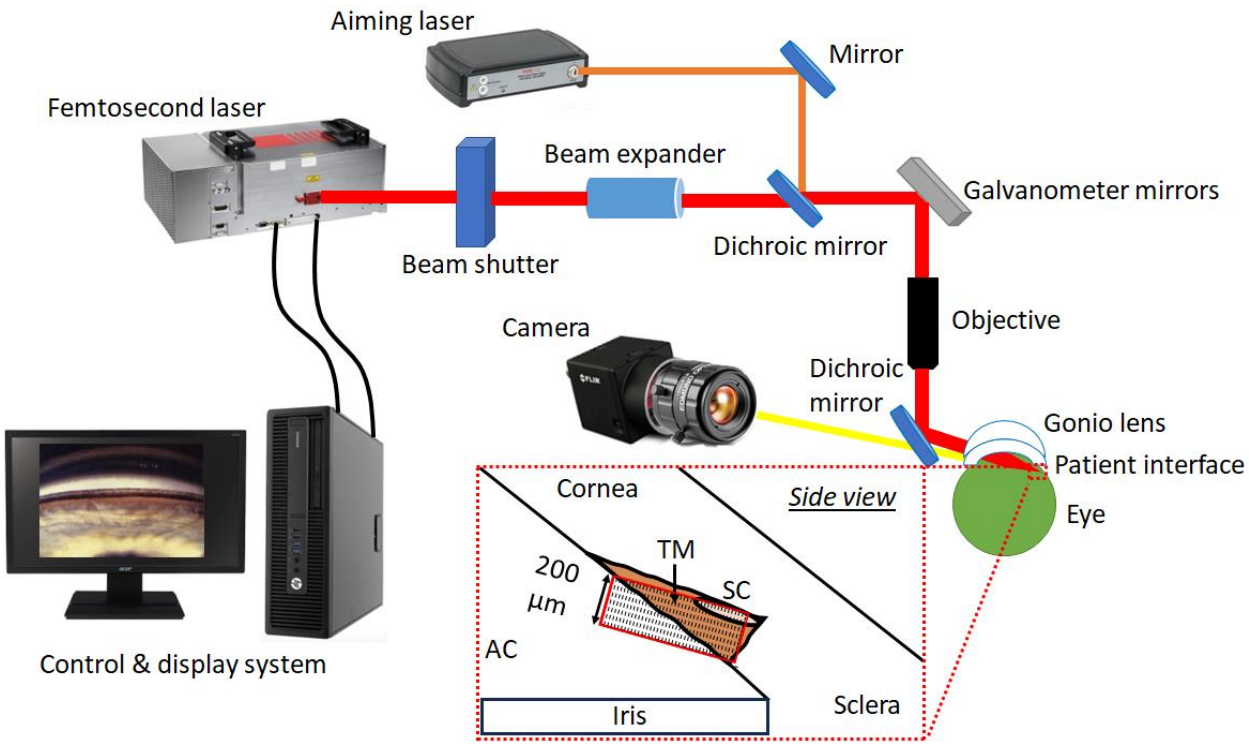

Figure 1.1: The components of the FLT surgical system. A commercial femtosecond laser was guided by a dual aiming beam, where the convergence of the dual beams to a single point on the trabecular meshwork indicates the focal point of the femtosecond laser. The gonio camera light passes through a dichroic mirror and then transmits through a custom-built gonio lens, a custom-built patient interface, and the transparent cornea. It eventually focuses onto the trabecular meshwork at the iridocorneal angle of a human eye. In the close-up image, the FLT laser is seen scanning across the entire trabecular meshwork, starting from inside SC and extending into the AC. The scan pattern is designed with a width of 500 μm and a height of 200 μm. However, it should be noted that the 500 μm cutting width along the circumferential direction of the corneoscleral rim (perpendicular to the paper direction) is not depicted in the image. FLT: femtosecond laser trabeculotomy; AC: anterior chamber; TM: trabecular meshwork; SC: Schlemm's canal.

The laser light passes through a beam expander (a|BeamExpander, Asphericon, Germany) to dilate the beam radius and fill the aperture of the objective. The beam scanning in the TM area is controlled by a pair of galvo-scanners, which determine the horizontal (X-axis) and vertical (Y-axis) directions. An objective lens focuses the laser beam through a custom gonioscopic lens into iridocorneal angle (spot size < 10μm). Additionally, a video camera is integrated into the system to facilitate real-time guidance by providing direct visualization of the iridocorneal angle structures. The femtosecond surgical beam is guided by a coaxial 5 mW, 632.8 nm HeNe dual aiming laser (Thorlabs, Inc., Newton, NJ, USA). The

convergence of the dual beams onto the TM serves as an indication of the focal plane of the femtosecond laser.

Figure 1.2 provides a schematic diagram illustrating the creation of the femtosecond channel and its dimensional relationship to the structures in the iridocorneal angle. The photodisruption occurs within a confined region corresponding to the beam focus size. This process is repeated as the femtosecond laser focus is scanned in a continuous rectangular volume through the TM tissues, resulting in the creation of a patent femtosecond channel connecting the anterior chamber (AC) to SC. The dimensions of the channel are determined by the channel width W in the horizontal direction (X-axis), and the channel height H in the vertical direction (X-axis).

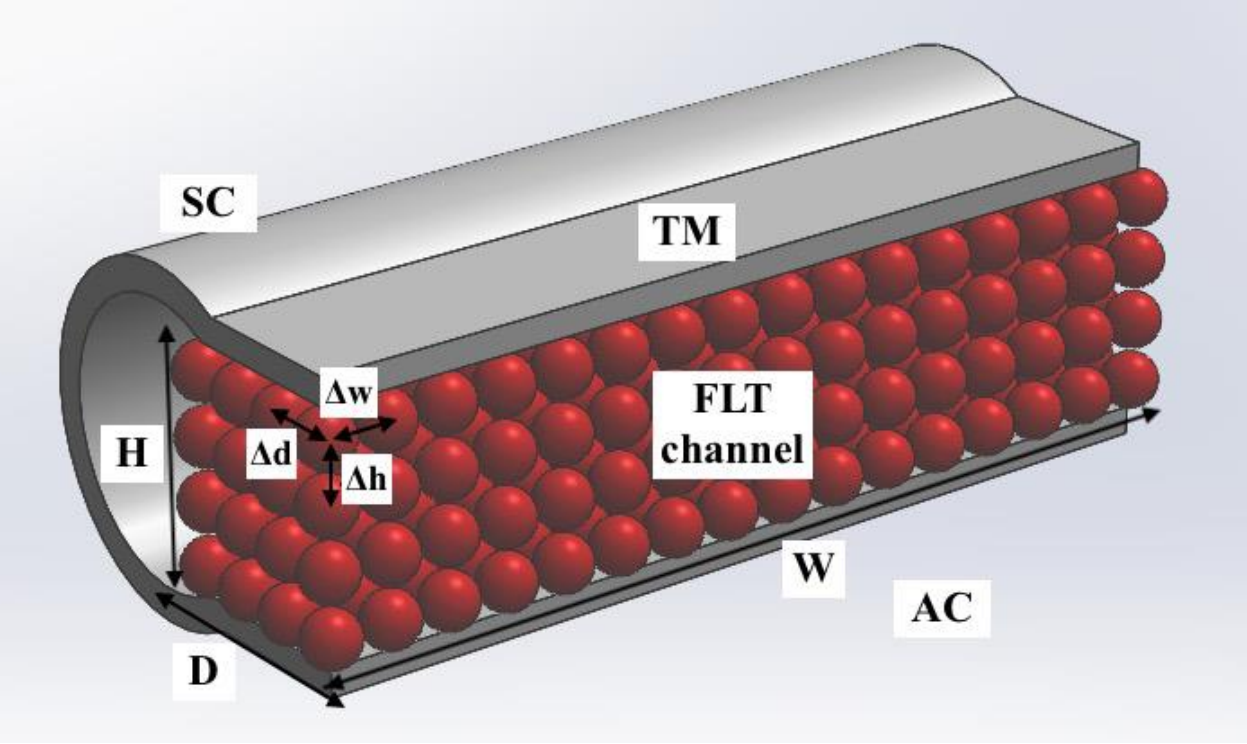

Figure 1.2: A schematic diagram illustrates a femtosecond-created channel penetrating through the TM, establishing a connection between the AC and SC. The geometry of the channel is determined by its width (W), height (H), and depth (D), while the laser spot, line, and layer separations are represented by Δw, Δh, and Δd, respectively. The red spots indicate the focal spots of the femtosecond laser arranged in a raster pattern, effectively photodisrupting the TM tissues. SC: Schlemm's canal; TM: trabecular meshwork; AC: anterior chamber.

Human Cadaver Eye Sample Preparation:

Six human cadaver eyes not suitable for transplant were obtained from the San Diego Eye Bank within 24 hours postmortem. Careful dissection was performed to preserve the TM while removing other ocular components, including the posterior segment, vitreous, lens, iris, ciliary body, choroid, and uveal tissues (Fig. 1.3A). Subsequently, the prepared eyes were stored in Optisol GS corneal transplant medium (Chiron Intraoptics, Irvine, CA) and refrigerated at 4°C (Fig. 1.3B). The experimental procedures adhered to the principles outlined in the Declaration of Helsinki.

To assess morphology and viability, the cadaver eyes were examined under an optical microscope before being mounted on a custom sample holder. The eyes were then perfused with Dulbecco's modified Eagle's medium (DMEM) containing 5 µg/mL amphotericin B and 100 µg/mL streptomycin (MilliporeSigma, MO) in a sterile tissue culture incubator (Sheldon Manufacturing, Inc., Cornelius, OR) at 37°C, 5% CO_2, and 95% humidity for 30 minutes (Fig. 1.3C). The corneal epithelium was removed due to irregularities in the surface quality. It should be noted that the perfusion system was strictly monitored to ensure the absence of bubbles or leakage, as this could impede the subsequent surgical procedure.

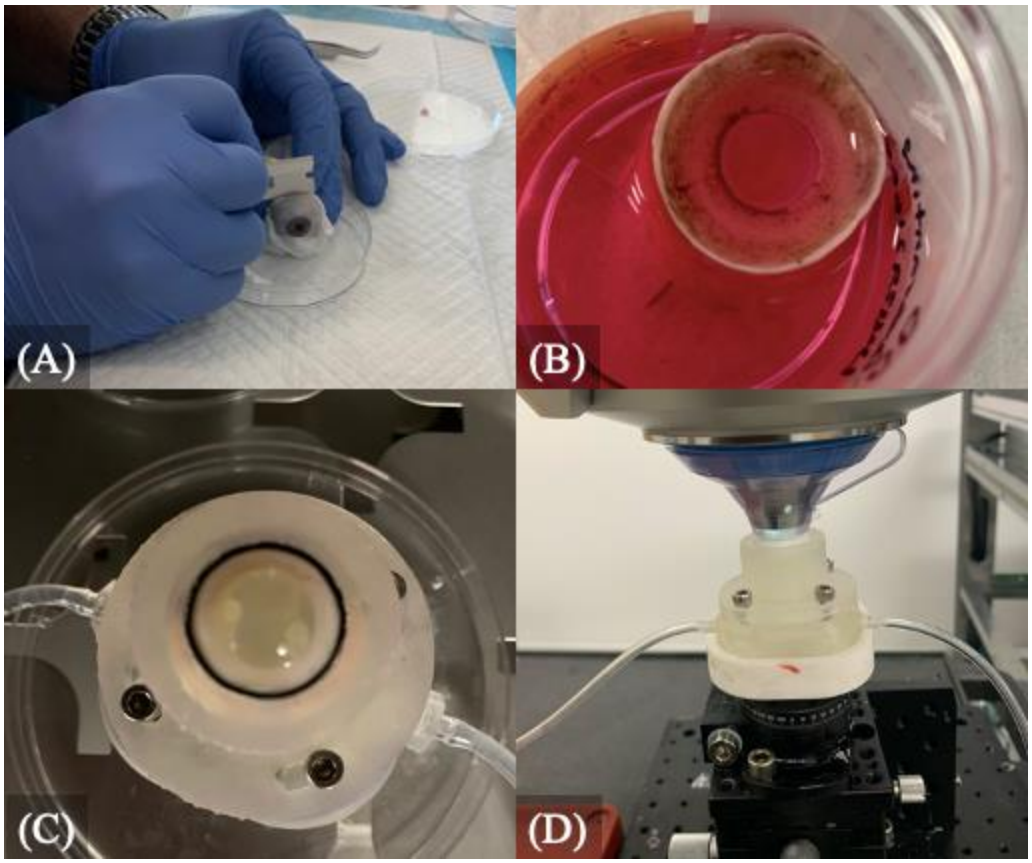

Figure 1.3: Sample preparation for the FLT surgery. (A) Human donor eyes were obtained from the San Diego Eye Bank within 24 hours postmortem. (B) An anterior segment with an intact trabecular meshwork was dissected and (C) carefully mounted on a custom ocular perfusion device in an incubator. (D) The eye was docked to the FLT surgical system via a custom-built patient interface between them. FLT: femtosecond laser trabeculotomy.

Femtosecond Laser Channel Creations in Human Cadaver Eyes:

The eye was subsequently positioned on a movable mechanical stage/sample holder equipped with five degrees of freedom, including x, y, z translations, rotation, and tilting, within the FLT laser surgery system (Fig. 1.3D). To optimize optical performance and provide a protective barrier, a custom-built patient interface was utilized between the laser system and the human cadaver eye, minimizing aberrations and reflective losses. Moreover, a drop of index matching gel GenTeal Gel (Novartis, Basel, Switzerland) was applied between the patient interface and the gonioscopic lens to reduce optical reflections at the interfaces.

To ensure clear visualization of the TM and surrounding tissues at the iridocorneal angle, a drop of 20% dextran was directly applied to the eye to mitigate corneal edema.

Prior to initiating the surgical procedure, meticulous adjustment of the gonioscopic camera and sample holder was performed to visualize the TM at the iridocorneal angle. Once the TM was visualized, the dual aiming beams were adjusted to overlap onto the TM surface, thus aiming the treatment laser. In this study, pulse energies of 10, 15, and 20 μJ were employed, and channels with dimensions of W×H=500×200 μm^2 were generated. Upon opening the laser shutter, the femtosecond laser beam initiated photodisruption through the TM, starting from inside SC and moving out towards the anterior chamber (AC), following a preprogrammed raster pattern controlled by the computer. The formation of an outflow channel took several seconds, depending on the laser scanning parameters and drainage geometry. Each eye received 5 channels at a particular energy.

Upon completion of the surgical procedure, the surgical position was marked to facilitate subsequent OCT imaging. Following the treatments, the eyes were fixed in 4% PFA (Mallinckrodit Baker, Inc., Phillipsburg, NJ) in phosphate-buffered saline (PBS) and dissected for post-surgery OCT imaging experiments.

OCT Imaging:

In this study, we used a spectral domain OCT to evaluate the created channels. The imaging system operates at an A-line rate of 50 kHz and a central wavelength of 890 nm, offering a theoretical axial resolution of 2.4 μm [135]. The tissue sample was immersed in

the PBS solution and carefully adjusted so that the OCT beam was scanned approximately perpendicular to the width of the surgical site.

Quantifying and Visualizing the Created Channels by OCT:

To assess the efficacy and precision of channel creation using the femtosecond beam, we conducted an evaluation of the OCT image stacks corresponding to the FLT channel (Fig. 1.4D). The evaluation was performed by analyzing the image slices individually (Fig. 1.4). We defined a continuous cutting width (W_c) of at least 200 µm within the desired 500 µm channel width as a complete drainage channel connecting to the SC, indicating a full thickness cut. Any width below this threshold indicated either partial thickness cuts or the absence of observable outflow channels (refer to Fig. 1.5).

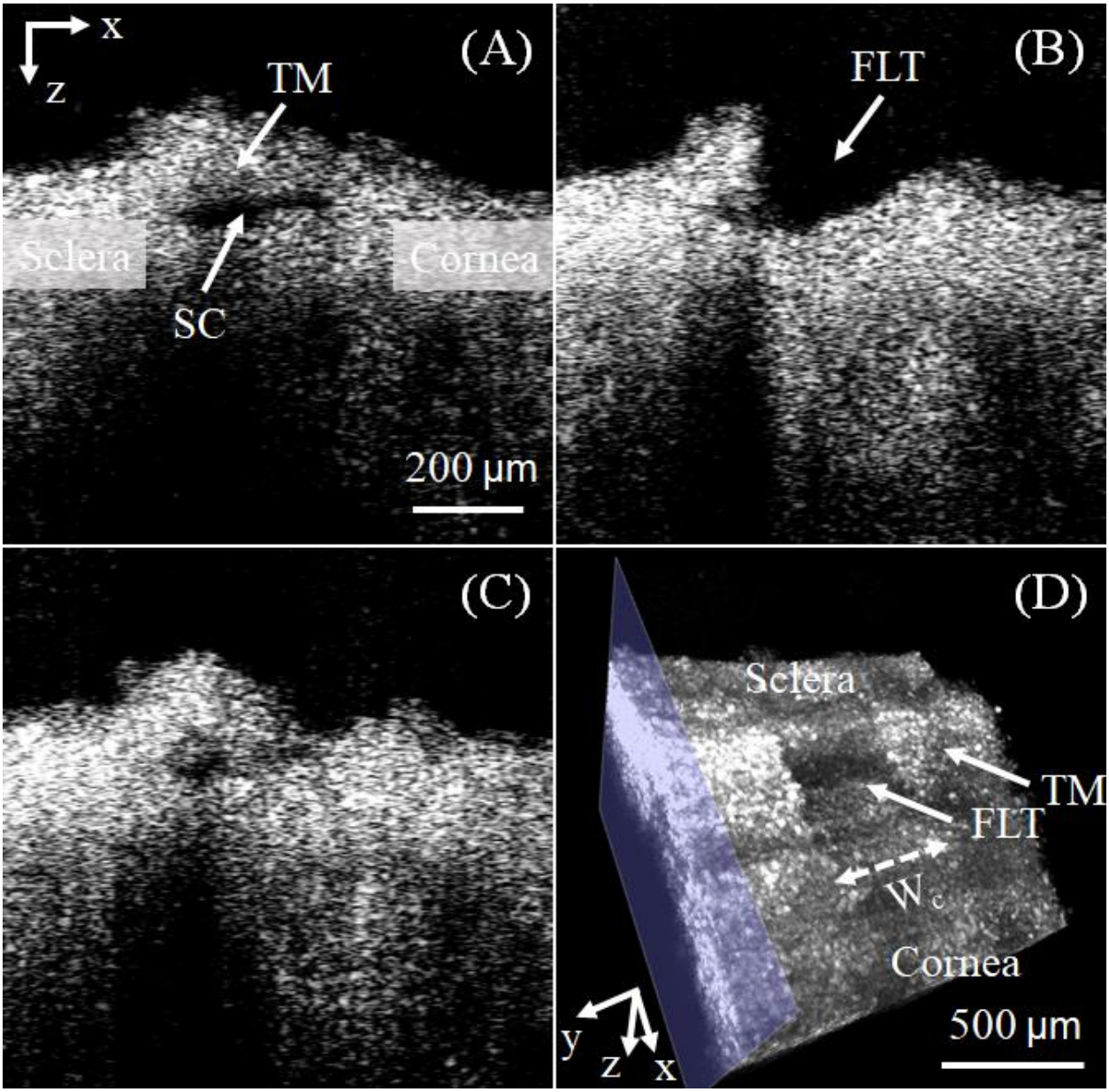

Figure 1.4: Representative OCT B-scan images at different slow-scanning locations and the 3D reconstructed image stack. As the sliding plane moves along the y-direction, the B-scan images show (A) an intact TM tissue, (B) a full-thickness cut creating an FLT channel connecting to SC, and (C) a partial-thickness cut in the TM tissue. The cutting width (W_c), analyzed from individual B-scans along the y-axis, serves as an evaluation metric detailed in Fig. 1.5. TM: trabecular meshwork; FLT: femtosecond laser trabeculotomy.

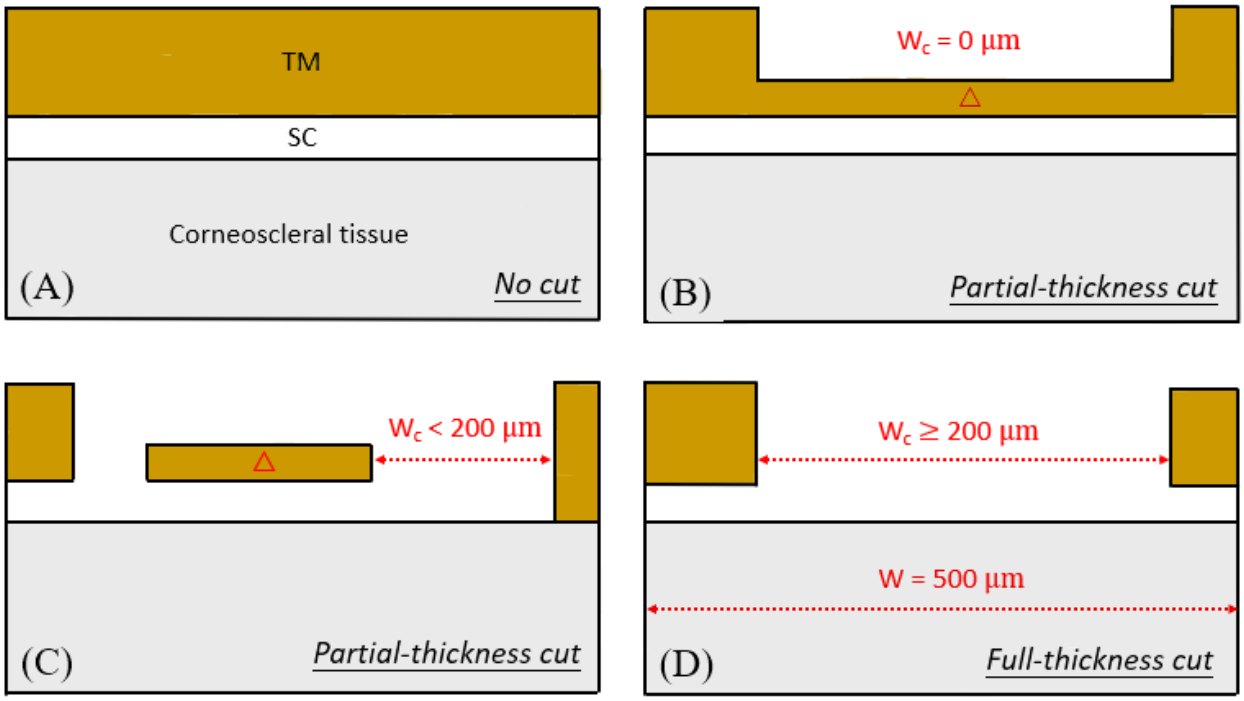

Figure 1.5: Illustration of how to evaluate the FLT outflow channels. The 0 µm cutting width was considered (A) when the trabecular meshwork is completely intact or (B) when it is partially cut through at any location along the circumferential direction (Y-axis). A partial thickness cut was also defined as a maximum continuous cutting width (W_c) below 200 µm (C), whereas a full thickness cut was characterized by a continuous cutting width of at least 200 µm (D). Note that the presence of marks '△' on the remaining trabecular meshwork in (B) and (C) indicates an incomplete cut through the trabecular meshwork. As a result, these areas were unable to connect to the SC and were not included in the calculation of the cutting width. FLT: femtosecond laser trabeculotomy; TM: trabecular meshwork; SC: Schlemm's canal.

Furthermore, the acquired image stacks were cropped to a volume size of V_{xyz} =1x1x1 mm^3, with the FLT outflow channel positioned at the center of the selected volumetric image. In the context of OCT imaging, z represents the depth direction, x corresponds to the fast scan direction, and y indicates the slow scan direction between B-scans. Subsequently, the image stacks were imported into FluoRender 2.25.2 software (Scientific Computing and Imaging Institute, Salt Lake City, UT, USA) for 3-D rendering. To enhance the visual representation, the 'Hot Effect' was applied along the depth in the software settings, facilitating the three-dimensional visualization.

Statistics:

Unpaired t-tests using GraphPad Prism 10 (GraphPad Software, Boston, MA, USA) was conducted to examine potential significant differences in the cutting widths associated with different FLT pulse energies (10 μJ vs. 15 μJ, 10 μJ vs. 20 μJ, and 15 μJ vs. 20 μJ).

Results

Representative Outflow Channels Under a Light Microscope:

Images of outflow channels taken through an operating microscope are shown in Fig. 1.6; channels are indicated by double arrows. These channels were created by irradiating the brownish TM with 15 μJ pulse energy using FLT surgery in a human donor eye. The corneoscleral shell was imaged at an angle, with the endothelium facing upward, allowing for direct capture of the TM by the optical microscope. While these images nicely demonstrate the location of the outflow channels, a more detailed assessment is required to determine whether the channels were fully cut by the FLT surgery. This evaluation can be achieved through a closer and deeper examination using a 3D OCT imaging modality, as reported below.

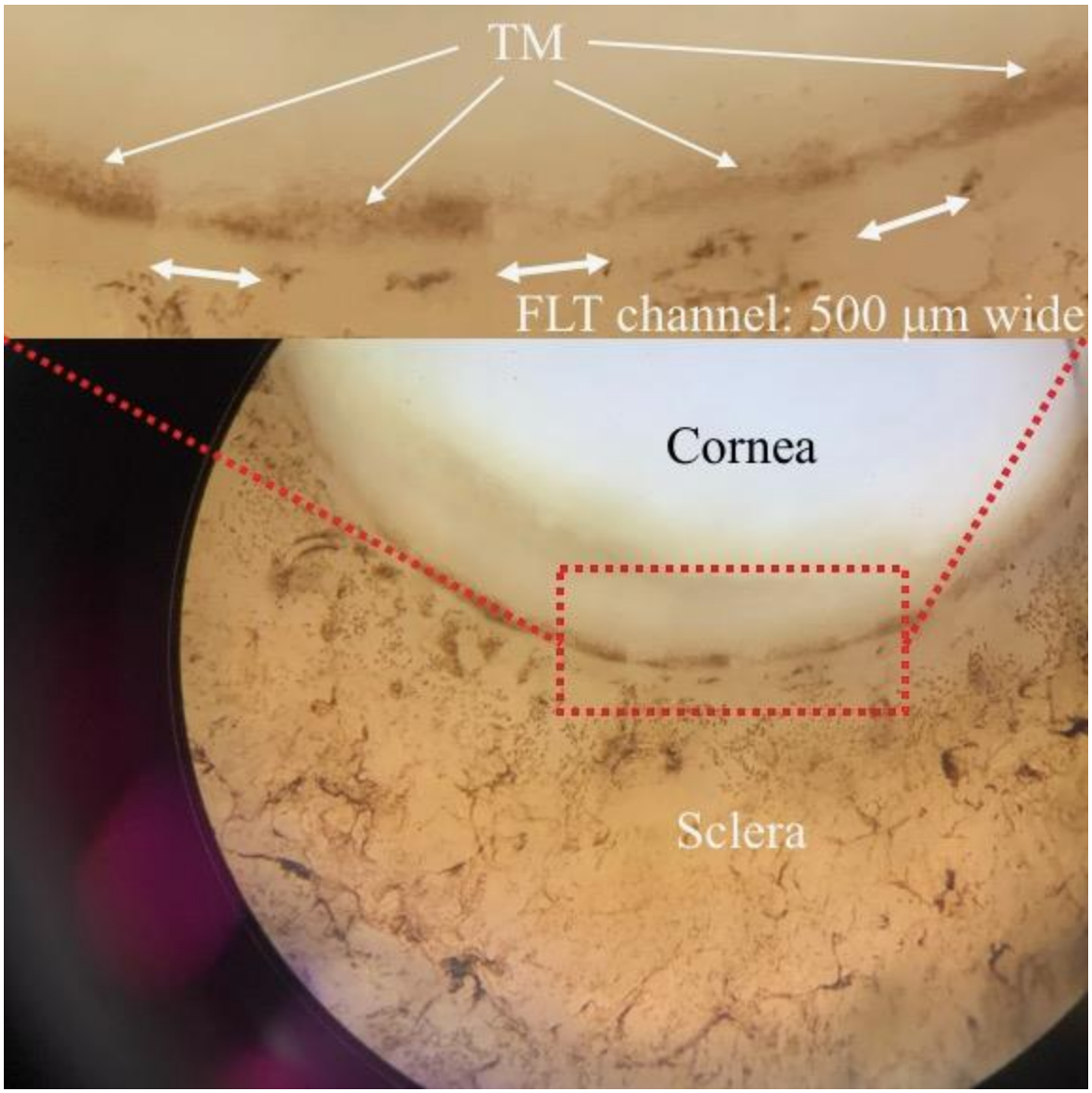

Figure 1.6: Three representative 500x200 µm^2 outflow channels (double arrows) were cut with 15 µJ through the brownish trabecular meshwork and observed under an optical microscope. FLT: femtosecond laser trabeculotomy; TM: trabecular meshwork.

OCT Evaluation of Femtosecond Laser Channel Creations at Varying Pulse Energies:

Figure 1.7 shows sample OCT images of FLT outflow channels at different pulse energies. In this specific case, the representative FLT channel created at 10 µJ pulse energy

was partially cut by the femtosecond laser, while the channels at 15 μJ and 20 μJ cut through the entire TM into SC.

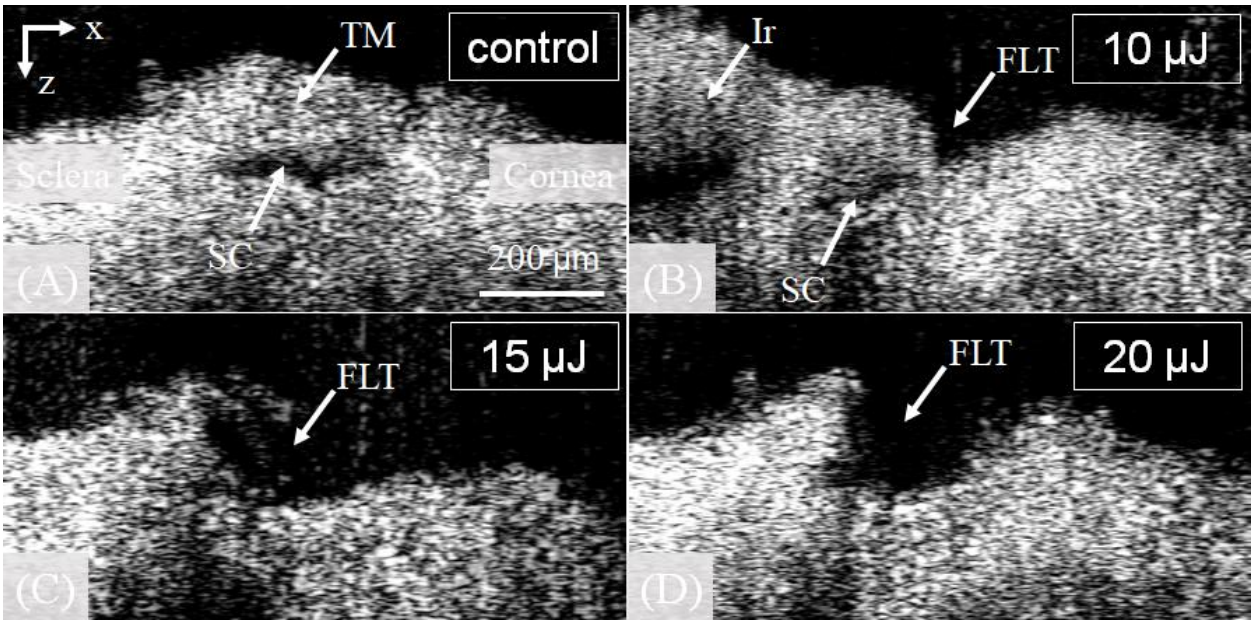

Figure 1.7: Sample OCT images of FLT outflow channels at varying pulse energies. A 10 μJ energy results in a partial-thickness outflow channel while both 15 μJ and 20 μJ energies result in full-thickness channels. FLT: femtosecond laser trabeculotomy; TM: trabecular meshwork; SC: Schlemm's canal.

The mean ± standard deviation cutting widths of the outflow channels through the TM were 74 ± 157, 403 ± 89, and 368 ± 99 μm for the 10 μJ, 15 μJ, and 20 μJ energy groups, respectively. These results are summarized in Fig. 8. Significantly different cutting widths were observed between the 10 μJ and 15 μJ groups ($P < 0.0001$), as well as between the 10 μJ and 20 μJ groups ($P < 0.0001$). However, there was no significant difference between the 15 μJ and 20 μJ groups ($P = 0.416$).

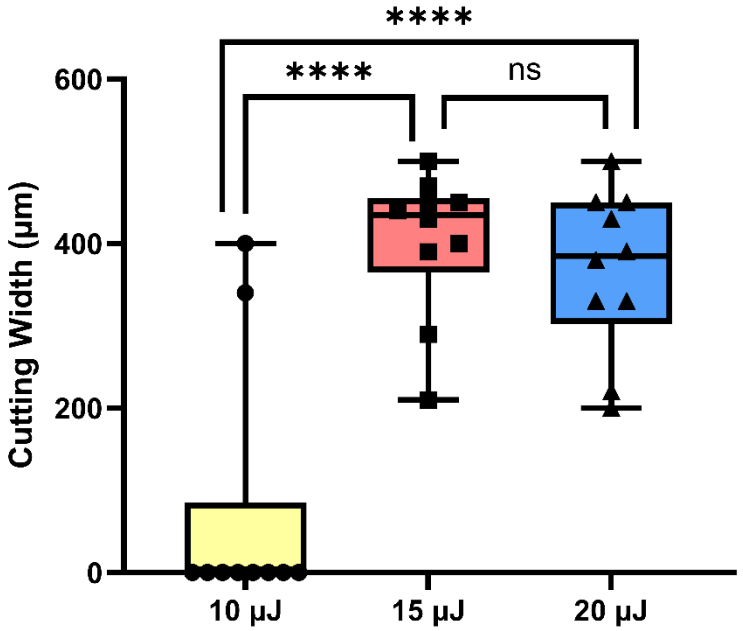

Figure 1.8: Statistics of the cutting width in the trabecular meshwork by different pulse energies. A significant difference in cutting width was observed either between 10 µJ and 15 µJ or between 10 µJ and 20 µJ (**** P<0.0001). However, there was no significant difference in the cutting width of the trabecular meshwork between 15 µJ and 20 µJ (ns: P>0.05). A pulse energy of 15 µJ is determined to be optimal for femtosecond laser trabeculotomy (FLT).

Table 1.1: OCT Evaluation of FLT Channels Created at Different Pulse Energies

	10 µJ		15 µJ		20 µJ	
	Cutting width (µm)	Result	Cutting width (µm)	Result	Cutting width (µm)	Result
CH #01	0	No	390	Full	450	Full
CH #02	0	No	440	Full	330	Full
CH #03	0	No	470	Full	380	Full
CH #04	0	Partial	450	Full	200	Full
CH #05	340	Full	400	Full	330	Full
CH #06	400	Full	430	Full	450	Full
CH #07	0	No	500	Full	390	Full
CH #08	0	No	450	Full	430	Full
CH #09	0	Partial	290	Full	500	Full
CH #10	0	No	210	Full	220	Full

Comprehensive data regarding all FLT channel creations are presented in Table 1.1. The results indicate that pulse energies of 15 µJ and 20 µJ achieved a 100% success rate in

creating full FLT channels with a continuous cutting width of at least 200 μm, as confirmed by OCT imaging. In contrast, the use of 10 μJ pulse energy resulted in the absence of channels in 6 cases, partial thickness channels in 2 cases, and complete FLT channels in 2 cases.

Three-Dimensional OCT Representation of the Femtosecond Laser Outflow Channels and Iridocorneal Angle Structures:

For a comprehensive understanding of the complete profile of the FLT channel at the iridocorneal angle, a three-dimensional visualization of a 1x1 mm^2 segment of the corneoscleral rim is provided in Fig. 1.9. In this representation, the SC appeared as a patent tube (Fig. 1.9A and B), accompanied by the overlaying TM tissue. Importantly, the OCT reconstruction clearly reveals a wedge-shaped channel created by the femtosecond laser. The TM is fully penetrated with sharp edges, resulting in direct exposure of SC to the aqueous humor in the anterior chamber (AC).

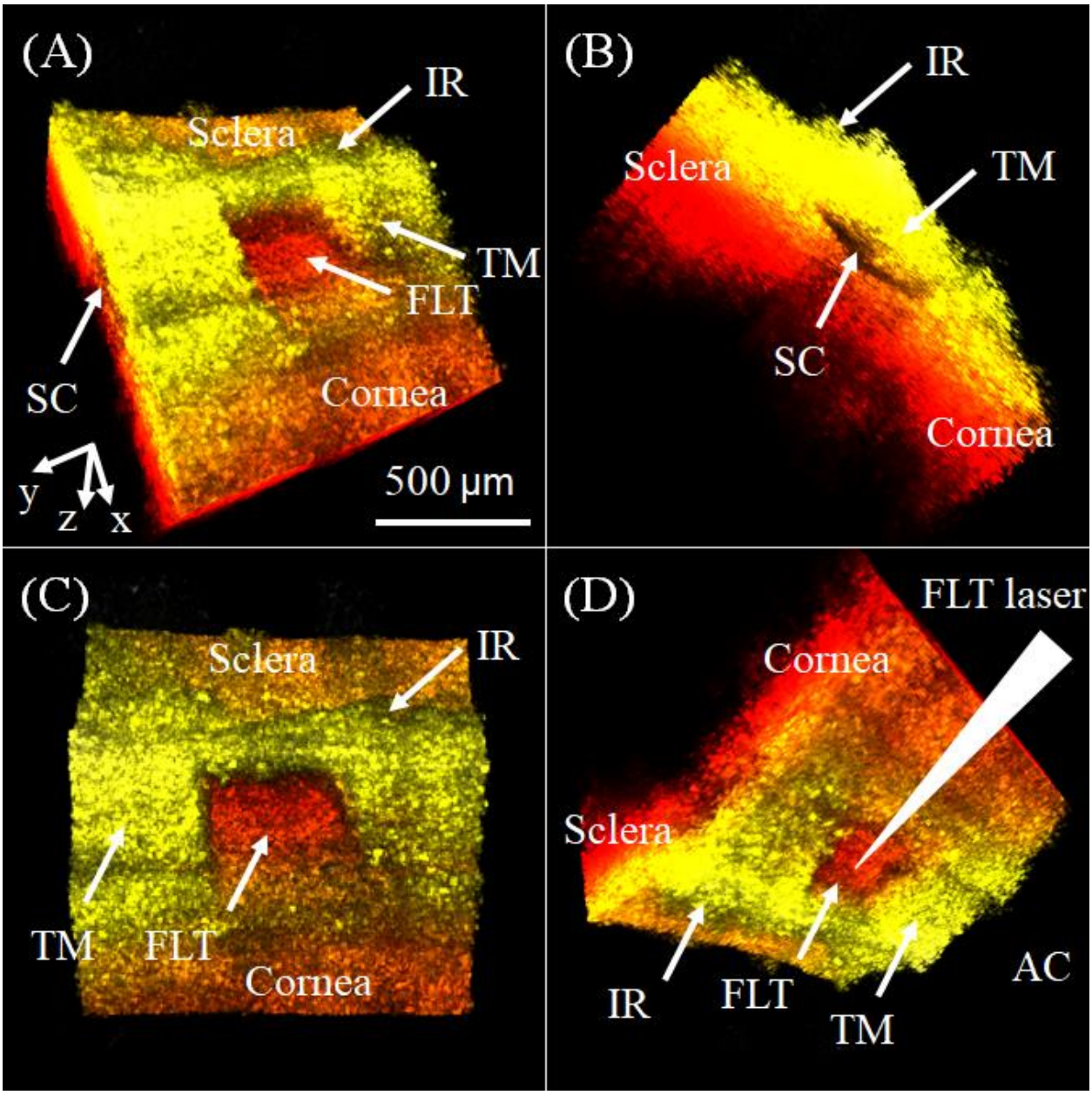

Figure 1.9: A representative 3D image stack of the iridocorneal angle, oriented at different perspectives, demonstrates a wedge-shaped FLT outflow channel cut through the trabecular meshwork (TM) and extending into Schlemm's canal (SC). This channel was created using a pulse energy of 20 µJ, effectively establishing a direct connection between SC and the aqueous fluid in the anterior chamber (AC). The relationship between the angle structures and the FLT surgical laser is illustrated in (D). FLT: femtosecond laser trabeculotomy; IR: iris root.

Discussion

In this study, we employed OCT to assess the impact of pulse energy on the creation of outflow channels during FLT surgery in human cadaver eyes. Our aim was to determine the optimized energy level for the surgical procedure. Overall, the present study demonstrated that pulse energy significantly influenced the creation of outflow channels during FLT surgery in human cadaver eyes,10 resulting in variations such as full thickness, partial thickness, or absence of observable channels, as observed through the spectral domain OCT imaging (see Table 1.1, Fig. 1.7). By evaluating the OCT images, we have determined that a pulse energy of 15 μJ reliably achieves the creation of outflow channels by photodisrupting the TM tissues in human cadaver eyes. Conversely, lower energy levels, such as 10 μJ, do not guarantee the attainment of full thickness cutting through the TM tissues. Typically, using the least amount of energy to accomplish a surgery is considered optimal. Any amount of energy over the minimum necessary, though it may not be damaging, is unneeded. These findings have potential implications for guiding the choice of pulse energy in the clinical setting.

Previous groups had explored using femtosecond laser to non-invasively bypass aqueous outflow resistance with limited success. Researchers have employed 800 nm femtosecond laser pulses focused directly through air onto the exposed TM within a 4-mm excised strip of the porcine corneoscleral rim [136]. Histological analysis revealed successful photodisruption of the TM, including the juxtacanalicular tissue, using moderate pulse energies of 7 to 14 μJ and short exposure times ranging from 0.5 to 2 seconds. Though this study successfully removed TM with a femtosecond laser, it was not done in a clinically relevant manner through the intact cornea. The same group also investigated the feasibility

of photodisrupting the TM using femtosecond laser pulses focused through a goniolens with significantly higher energies of 60-480 μJ [137]. However, histological results indicated that they were unable to reach the innermost layer of the TM known as the juxtacanalicular tissue and the inner wall of SC, which are believed to contribute to the greatest resistance to aqueous outflow [5, 6]. This failure may be attributed to the lack of necessary optimization of the focal spot size of the femtosecond laser beam propagating through the gonioscopic contact lens, cornea, and anterior chamber, as well as the absence of proper visualization of the iridocorneal angle structures.

It has been reported that researchers used two-photon or histological imaging to evaluate the femtosecond laser created channels [136-138]. However, both imaging techniques necessitate tissue sectioning and face challenges in determining the continuous and overall cutting profile of the entire FLT channel. OCT demonstrated its capability of three-dimensional imaging of the entire femtosecond-created channels in human cadaver eye tissues [66]. Moreover, our previous experience utilizing a custom-built spectral domain OCT to provide detailed visualization of the iridocorneal angle structures [1, 139], supports the suitability of OCT for this investigation. As previously discussed in this study, OCT has been employed as an effective tool to evaluate the impact of pulse energy on the generation of outflow channels during FLT surgery in human cadaver eyes. Furthermore, OCT has successfully aided in determining the optimal energy level for the FLT procedure. A three-dimensional OCT reconstruction clearly depicted the location of the outflow channel within the TM, thus establishing a direct connection between SC to aqueous fluid in the anterior chamber (see Fig. 1.9). This poses a possibility that OCT can be translated for evaluations of

the clinical laser surgery for the treatment of glaucoma. Further investigation of OCT imaging follow-ups is needed to assess the long-term outcomes after surgery [140].

It is important to discuss the acceptance criteria defined in this study for a "full channel", which was defined as a channel with a continuous cutting width of at least 200 μm fully penetrating the TM into SC. Since the channel width defined in the experiment is 500 μm, one would reasonably expect that the success criteria would be closer to 500 μm. The criteria of 200 μm or greater is borne from prior laboratory experience in passing femtosecond pulse obliquely through the cadaver cornea, across the anterior chamber, and to the TM [141, 142]. Though we employed strict acceptance criteria and handling procedures regarding the donor cadaver tissue, there still exists uncontrollable variability in the quality of the corneas, specifically the viability of the endothelium and surface quality of the cornea. Endothelial function directly affects corneal clarity and edema. Additionally, cadaver corneoscleral rims are subject to wrinkling on the posterior corneal surface. The consequence of these defects is variability in the quality of the trabeculotomy in the tissue. Taking into consideration the variability of these tissues, one would not expect full width cuts all the time, as shown by the data in Table 1.1. For example, in living tissue, the corneas could be expected to be clearer than cadaver corneas and therefore may achieve more complete cuts in lower energies.

Chapter 2: Thermal Collateral Damage During FLT: an Ex-vivo Study

Introduction

Another question that arises regarding femtosecond laser trabeculotomy (FLT) is: Is it safe, and what are the temperature variations and potential collateral damage during FLT? This chapter aims to answer these questions.

Materials and Methods

Human eye globes were received from the San Diego Eye Bank within 24 hours of death. Eyes were dissected before being mounted to an artificial anterior chamber which was then docked to the FLT surgical device. The artificial anterior chamber (Fig. 2.1) is described in more detail in past preclinical studies [66, 142]. Eyes were bisected along the equator before removing the choroid, vitreous, lens, iris and aqueous humor leaving a corneoscleral hemisphere/shell. The artificial anterior chamber and corneoscleral shell were perfused with low glucose Dulbecco's modified eagle's medium (DMEM). The DMEM was supplemented with 5 μg/mL amphotericin-b (antifungal) as well as 100 U/mL penicillin (concentration of penicillin reported in arbitrary units per milliliter [U/mL]) and 100 μg/mL streptomycin. The corneoscleral shells underwent FLT using following system parameters: pulse energy (21 μJ), height (200 μm), width (500 μm).

Figure 2.1: Artificial anterior chamber.

Human cadaver tissues that had undergone FLT were imaged using light microscopy, and second harmonic generation (SHG) imaging. Seven 5 mm by 2.5 mm trabecular meshwork samples from 2 eyes were used in the temperature measurement study. Two eyes were used for the structural thermal damage imaging analysis, one channel per eye per modality.

Light Microscopy/Histology:

Tissue samples were fixed in 4% paraformaldehyde. Sample thin slices (1 μm) for light microscopy were sectioned from the tissue. Slices were stained with H&E and imaged with standard light microscopy. Regions containing the femtosecond trabeculotomy as well

as untreated tissues adjacent to the trabeculostomy were evaluated. Light microscopy was performed by the University of California, Irvine Department of Ophthalmology.

Second Harmonic Generation Imaging (SHG) and Autofluorescence:

SHG is an imaging method particularly useful for studying thermal denaturization of collagen[143, 144] since there is a direct loss of SHG signal associated with thermal damage to collagen. The outer wall of Schlemm's canal is adjacent to the sclera, which is primarily composed of collagen, making this tissue region suitable for SHG imaging. Furthermore, the trabecular meshwork generates a strong auto fluorescent signal due to the pigmented endothelial cells lining the trabecular meshwork. Tissue was fixed in paraformaldehyde and sectioned into 250 μm thick radial slices. A multiphoton microscope (Leica STELLARIS 8 FALCON, Wetzlar, Germany) was used to perform SHG imaging. The wavelength of the femtosecond excitation laser was set to 820 nm while the collection band for SHG and autofluorescence were set to 390-420 nm and 450-550 nm, respectively. Images were taken both with the region of the trabeculostomy and in untreated adjacent tissues at 20x magnification. SHG imaging was performed by the University of California, Irvine Department of Ophthalmology.

Thermal Measurements:

A section of tissue containing trabecular meshwork measuring approximately 5 mm x 2.5 mm was dissected from a cadaver eye. The tissue sample was fixed to a custom sample holding fixture such that an FLT procedure could be performed on the sample using the FLT

system. A thermocouple was positioned adjacent to the treatment site on the tissue sample such that the tip of the probe was abutting the laser treatment site. A schematic of the experimental setup is provided in Fig. 2.2. A standard treatment was initiated while measuring the temperature of the tissue immediately adjacent to the laser treatment site. Laser treatment parameters are indicated in Fig. 2.2. The temperature was sampled at 100 Hz for 5 seconds prior to the initiation of the treatment and over the total duration of the procedure.

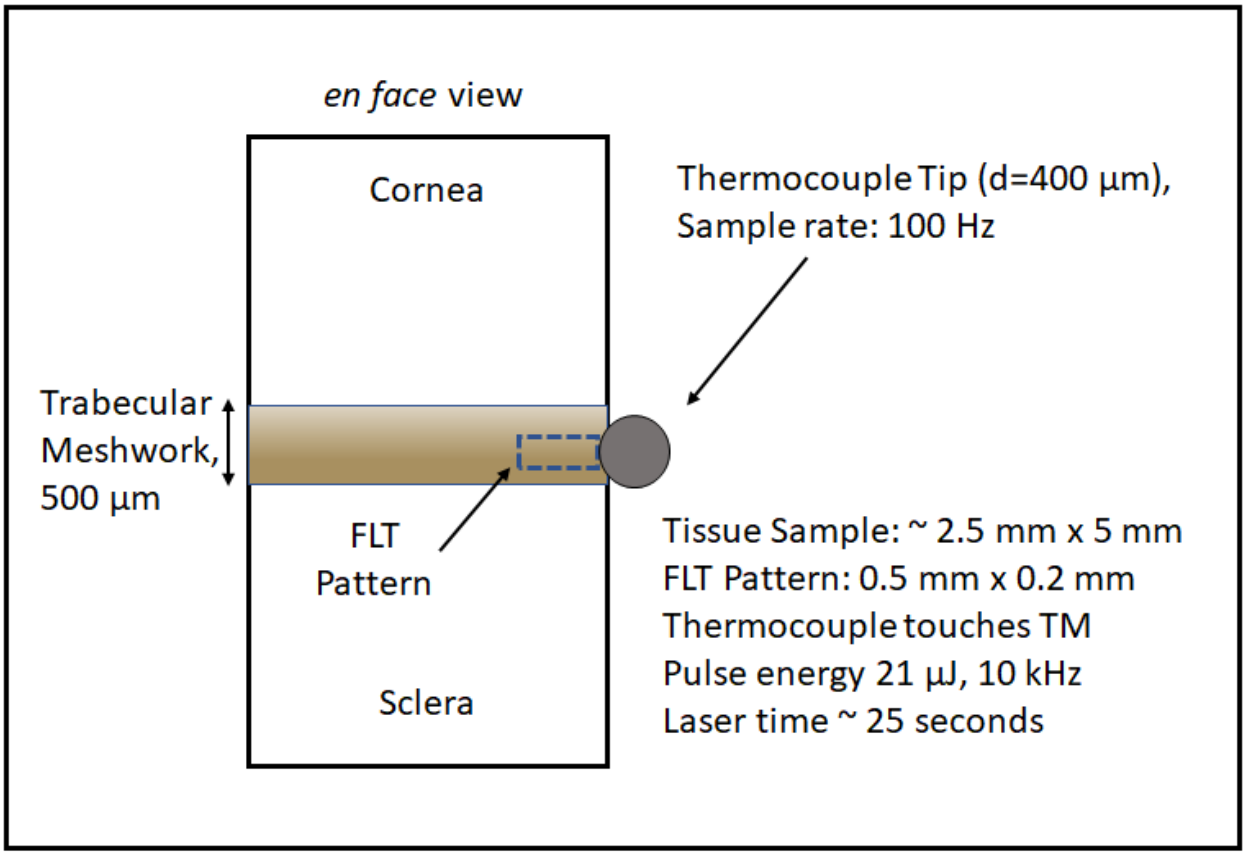

Figure 2.2: Heating measurement and sample positioning.

Results

Temperature Measure:

The maximum recorded temperature was 3.1°C (5.6 °F) [see 'sample a' plot in Fig. 2.3] above baseline. The average maximum temperature across all 7 measurements was 2.2 ± 0.6 °C (4.0 ± 1.1 °F) above baseline. It is also noted that the temperature change decays to less than 1°C after about 5 seconds after the procedure. Fig. 2.3 shows the temperature rise plots for all samples.

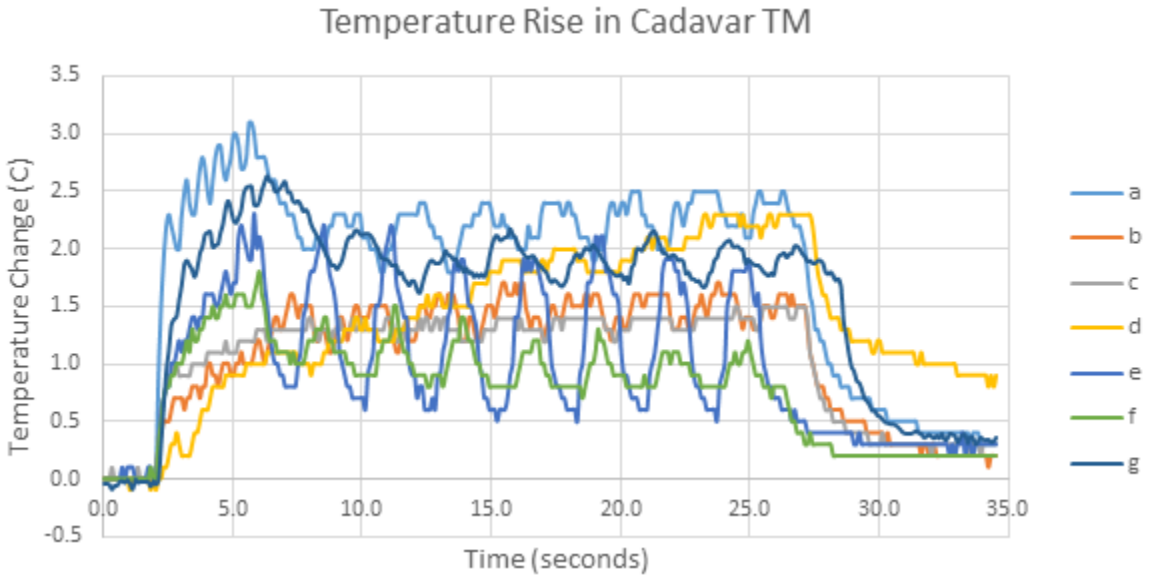

Figure 2.3: Temperature rise plots.

Light Microscopy/Histology:

H&E histology at 400x magnification showed continuous eosin-stained collagen fibers (asterisks) along the outer wall of the Schlemm's canal and into the FLT region; hematoxylin-stained nuclei (arrows) were also visible along the outer wall of Schlemm's canal in the FLT channel (Fig. 2.4). Trabecular beams were identified in the TM distal to the

treatment area. Intact collagen fibers and the presence of Schlemm's canal endothelial cells in the immediate vicinity of the FLT channel indicate there is no thermal damage.

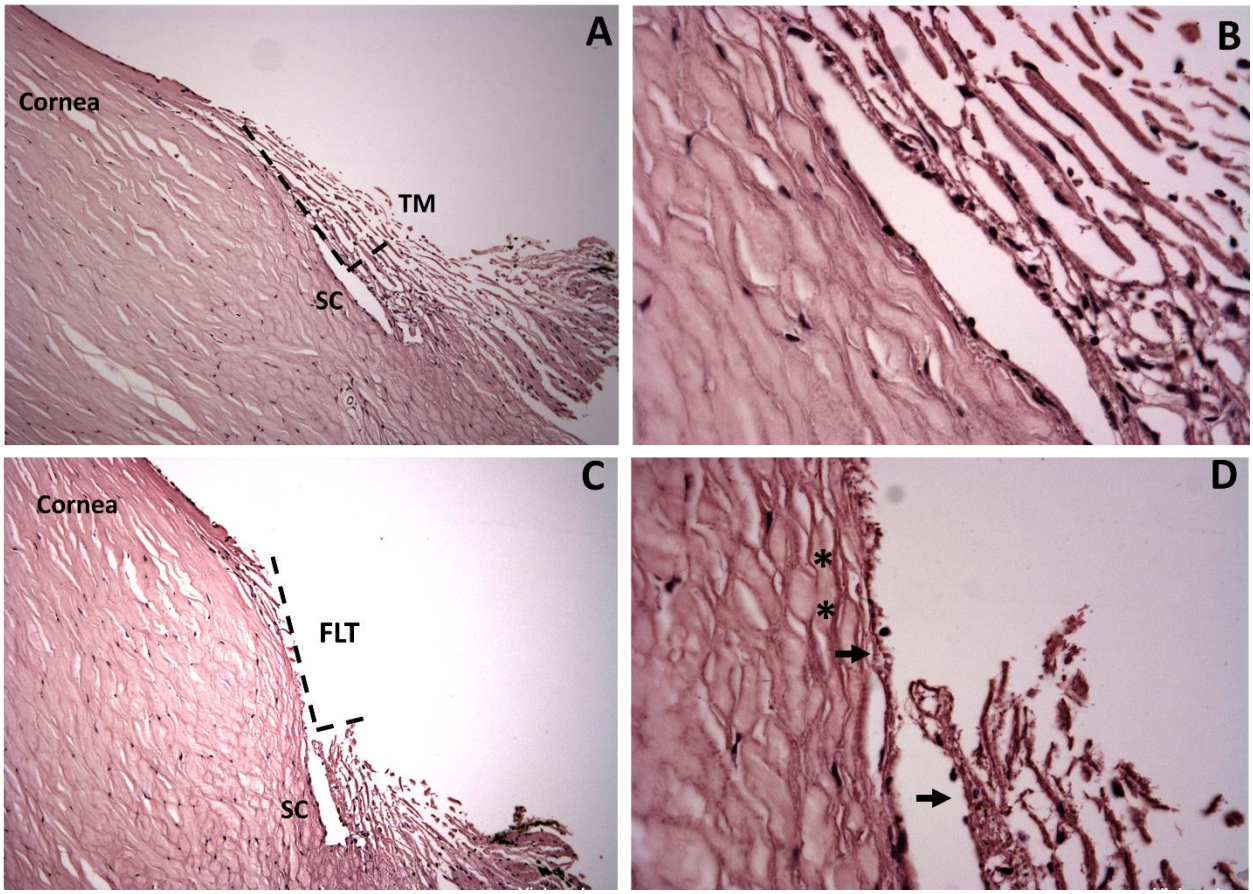

Figure 2.4: H&E stain histology. A) 100x magnification of untreated TM. B) 400x magnification of untreated TM. C) 100x magnification of FLT channel and surrounding tissue. D) 400x magnification of FLT channel. '*' demarcate intact collagen fibers distal to FLT. Arrows point to Schlemm's canal endothelial cells in the vicinity of FLT.

SHG and Autofluorescence:

Figure 2.5 depicts a two-photon autofluorescence (Red)/SHG (Green) image, illustrating both the intact trabecular meshwork (TM) region adjacent to the FLT channel (A) and the region containing the FLT channel itself (B). Panel A, captured with a ×20 objective, showcases the pristine TM, Schlemm's canal, collector channel, and Schwalbe's line, with an untouched and continuous outer wall. Panel B, also captured with a ×20 objective, reveals

the FLT drainage channel passing through the TM and into Schlemm's canal, with Schwalbe's line and the outer wall of Schlemm's canal remaining undisturbed. The asterisks denote an uninterrupted tissue layer on the surface of the outer wall, which starts within Schlemm's canal and extends outward without disruption into the region of the FLT drainage channel. The continuous collagen fibers from beneath Schlemm's canal to the FLT channel region indicate no thermal collateral damage to the tissue.

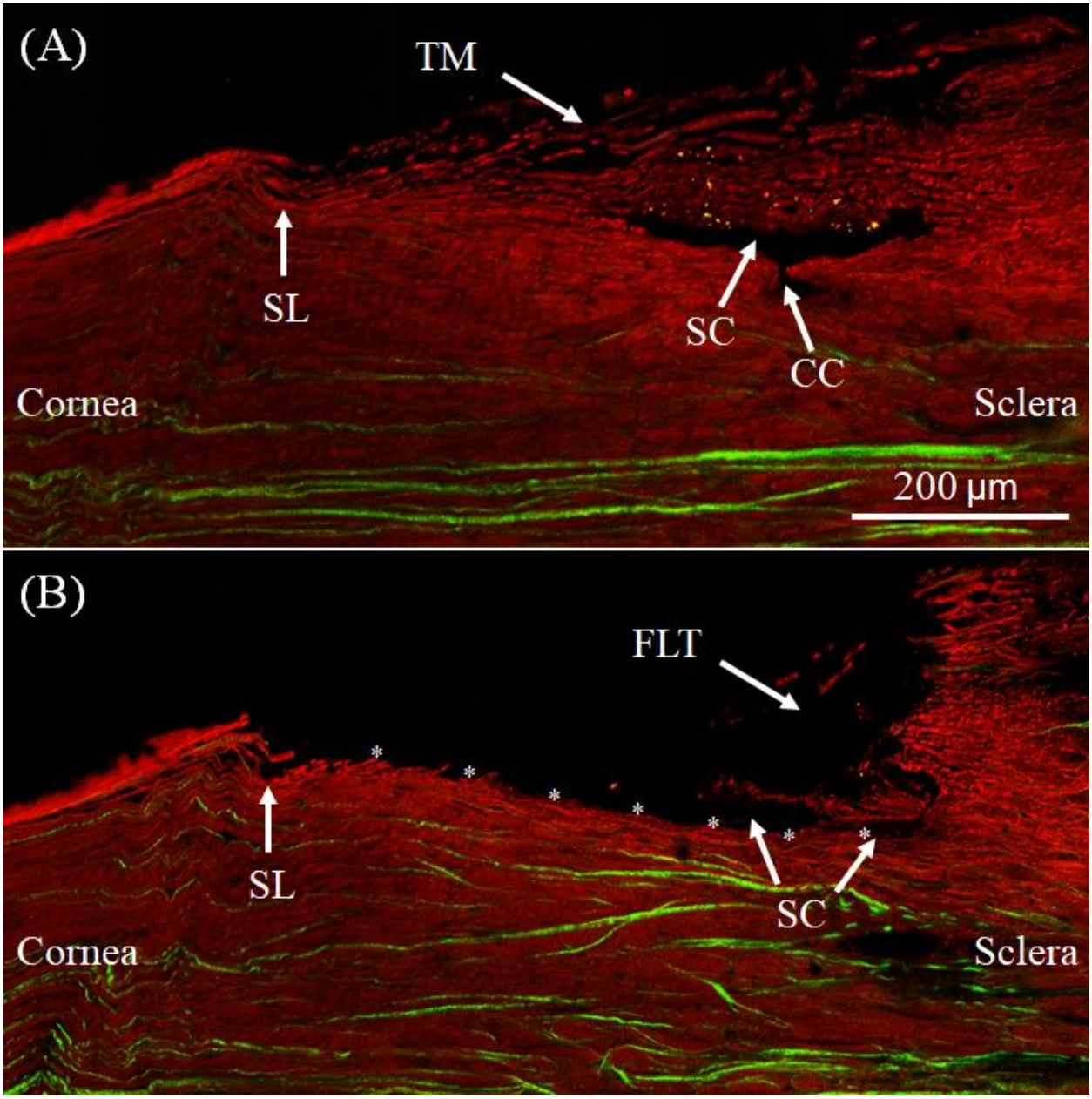

Figure 2.5: (A) An image combining autofluorescence (Red) and SHG (Green) captured using a 20x objective, displaying the intact trabecular meshwork (TM), Schlemm's canal, collector channel (CC), and Schwalbe's line (SL). (B) A 20x objective image merging autofluorescence and SHG, revealing the FLT drainage channel, Schlemm's canal (SC), remaining TM, and Schwalbe's line (SL). The asterisks delineate an undisturbed tissue layer connecting the FLT channel region to the inner region of SC. The abnormal curvature of the posterior side (endothelium and TM facing up) in both (A) and (B) results from tissue swelling.

Discussion

The onset of thermal denaturization of collagen has been measured to be on average 58°C, while the main transition to a denatured state occurs at 65°C [145]. Another study assessing collagen denaturization/damage as a function of collagen crimp contrast found 80% reduction in contrast signal after 1900 seconds at 55°C and the same amount of damage after just 16 seconds at 70°C. Decay was minimal under 50°C [146]. In the present study a maximum temperature rise of 3.1°C was measured during FLT while the average temperature during FLT was about 2 degrees above baseline. In the in-vivo case this would mean approximately 3 degrees above body temperature resulting in a maximum temperature of about 40°C. This is well below the reported temperatures required for protein denaturization and the resulting thermal collateral damage. Additionally, the presence of an intact collagen fiber on the outer wall of SC, adjacent to the FLT channel, in Figure 2.5B (SHG) indicates no tissue heating. It is well established that the ability of collagen to generate a second harmonic signal is drastically diminished after thermal insult [147]. Any significant heating would result in the inability to resolve individual fibrils which appear as clusters of dots in figure 2.5B near or below the 'star'.

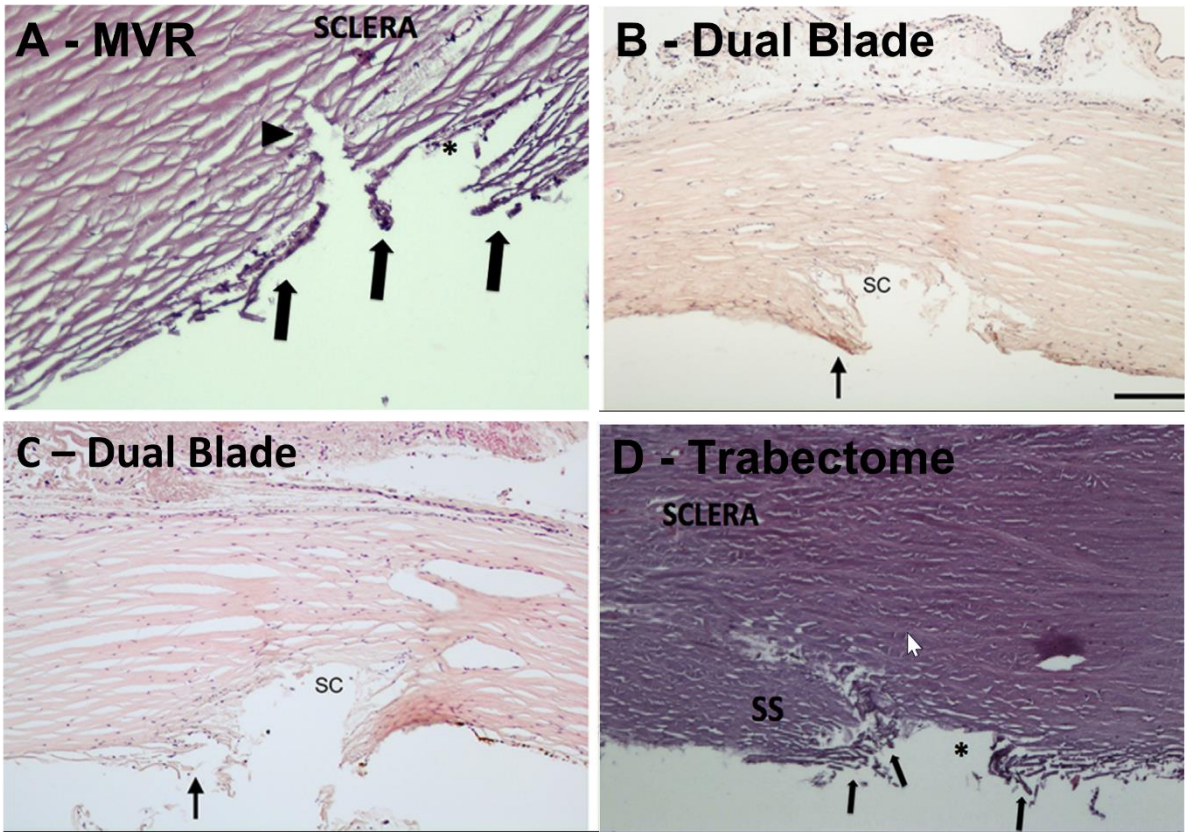

Figure 2.6: A comparison of histology from cadaver experiments using various SC based procedures [148, 149]. SC: Schlemm's canal; SS: scleral spur.

In general, the results of this study have demonstrated that FLT spares the outer wall of SC and adjacent tissues. It is also interesting to compare against other SC based procedures and the integrity of the outer wall following the procedures. Figure 2.6 is a histological summary of microvitreoretinal (MVR), dual blade goniotomy, and the Trabectome [148, 149]. Panel A shows a goniotomy with an MVR blade in cadaver tissue. The incision is imprecise and extends at least 100 microns beyond the outer wall into the sclera. Panels B and C show sample tissue after goniotomy with a dual blade device. It is clear the incision extends a few dozen microns beyond the outer wall and that much of the outer wall is damaged. Panel D shows the trabecular meshwork following a procedure with the Trabectome. The outer wall is tattered and there is evidence of thermal denaturization of collagen in the proximal or anterior trabecular meshwork.

Chapter 3: Dispersion Compensation for OCT

Introduction

We have previously demonstrated the feasibility of using femtosecond lasers for the treatment of glaucoma by optimizing pulse energies and evaluating potential damages related to FLT surgery using human cadaver eyes. The next key question is whether OCT imaging can benefit FLT treatment. Fully answering this question is challenging because clinical verification is needed through further steps involving OCT image-guided FLT surgery and assessing the intraocular pressure effects on patients. In Chapters 3 and 4, our goals are to develop a high-resolution OCT system and to image the iridocorneal angle structure details closely associated with glaucoma development. In this chapter, our aim is to improve the imaging axial resolution through dispersion compensation, which is an indispensable step in OCT development. To achieve this, we introduced a novel short-time Fourier Transform (STFT) and an iterative method for processing a single A-line spectrum mirror data to extract the system's dispersion.

Theory

Dispersion in SD-OCT:

The interference fringes, after background subtraction, are given by Eq. 3.1 [150], where k is the angular wavenumber, I(k) is the spectral interferogram, ρ is the responsivity of the detector, S(k) is the power spectrum of the light source, R_R and R_{Sn} are reflectivities

in reference and sample arms, $2\Delta z_n \cdot n_g$ is the optical path difference at sample depth z_n between the two arms which is scaled by the group refractive index of the material n_g at depth z_n, $\Delta\Phi(k)$ is the wavenumber-dependent dispersion correction term.

$$I(k) = \frac{\rho}{2} Re\left\{S(k)\sum_{n=1}^{N}\sqrt{R_R R_{Sn}}e^{i\left[2\frac{w}{c}\Delta z_n \cdot n_g + \Delta\Phi(k)\right]}\right\} \quad (3.1)$$

The phase function $\Delta\Phi(k)$ can be expanded as a Taylor series around the central wavenumber k_0:

$$\Delta\Phi(k) = \Delta\Phi(k_0) + \left.\frac{\partial\Delta\Phi(k)}{\partial k}\right|_{k_0} \cdot (k-k_0) + \frac{1}{2}\cdot\left.\frac{\partial^2\Delta\Phi(k)}{\partial k^2}\right|_{k_0} \cdot (k-k_0)^2 + \cdots + \frac{1}{n!}$$

$$\cdot\left.\frac{\partial^n\Delta\Phi(k)}{\partial k^n}\right|_{k_0} \cdot (k-k_0)^n \quad (3.2)$$

Since a_1 is a positional shift term, typically it is sufficient to compensate the second and third-order dispersion compensations with the phase correction term rewritten in Eq. 3.3 [151], where a_2 and a_3 are the second and third-order dispersion compensation coefficients, k_0 is the central angular wavenumber. Once $\Delta\Phi(k)$ is obtained, the Fourier transform of the dispersive fringe multiplied with $e^{-i\Delta\Phi(k)}$ produces a depth profile with improved axial resolution.

$$\Delta\Phi(k) = -a_2 \cdot (k-k_0)^2 - a_3 \cdot (k-k_0)^3 \quad (3.3)$$

Time-frequency Analysis (TFA):

Time-frequency analyses (TFAs) are a group of techniques that represent both the time and frequency domains simultaneously, which is particularly useful for detecting non-stationary signals [152]. The most common form is the STFT. Briefly, STFT performs a size-

fixed, localized segmental windowed Fourier transform, repeatedly sliding through a signal over time, after which it takes the summation of the series of windowed Fourier transforms. In practice, STFT of a resampled spectral interferogram produces a two-dimensional graphic representation of the energy distribution in the wavenumber and depth directions. While it is simple, window size selection and overlap of windows are of extreme importance when STFT is applied to the spectral interferogram because there is a trade-off between spatial and spectral resolutions in those two directions. A narrower spectral window size results in good spectral resolution but poor spatial resolution, while a longer spectral window size will improve the spatial resolution in z with poor spectral resolution. Since we aimed to favor a better spatial resolution to ensure the accuracy in peak position determination in z-space, we chose a large spectral window length with 1024-pixel points. Details of evaluation in window size and overlaps chosen will be discussed later. Figure 3.1 illustrates how STFT works and can be potentially used for targeting the dispersion mismatch using a mirror measurement. The dispersion is exhibited by the sub-bandwidth reconstructed PSFs' shift and broadening, although the main cause of the latter comes from the reduced spectral bandwidth by windowing.

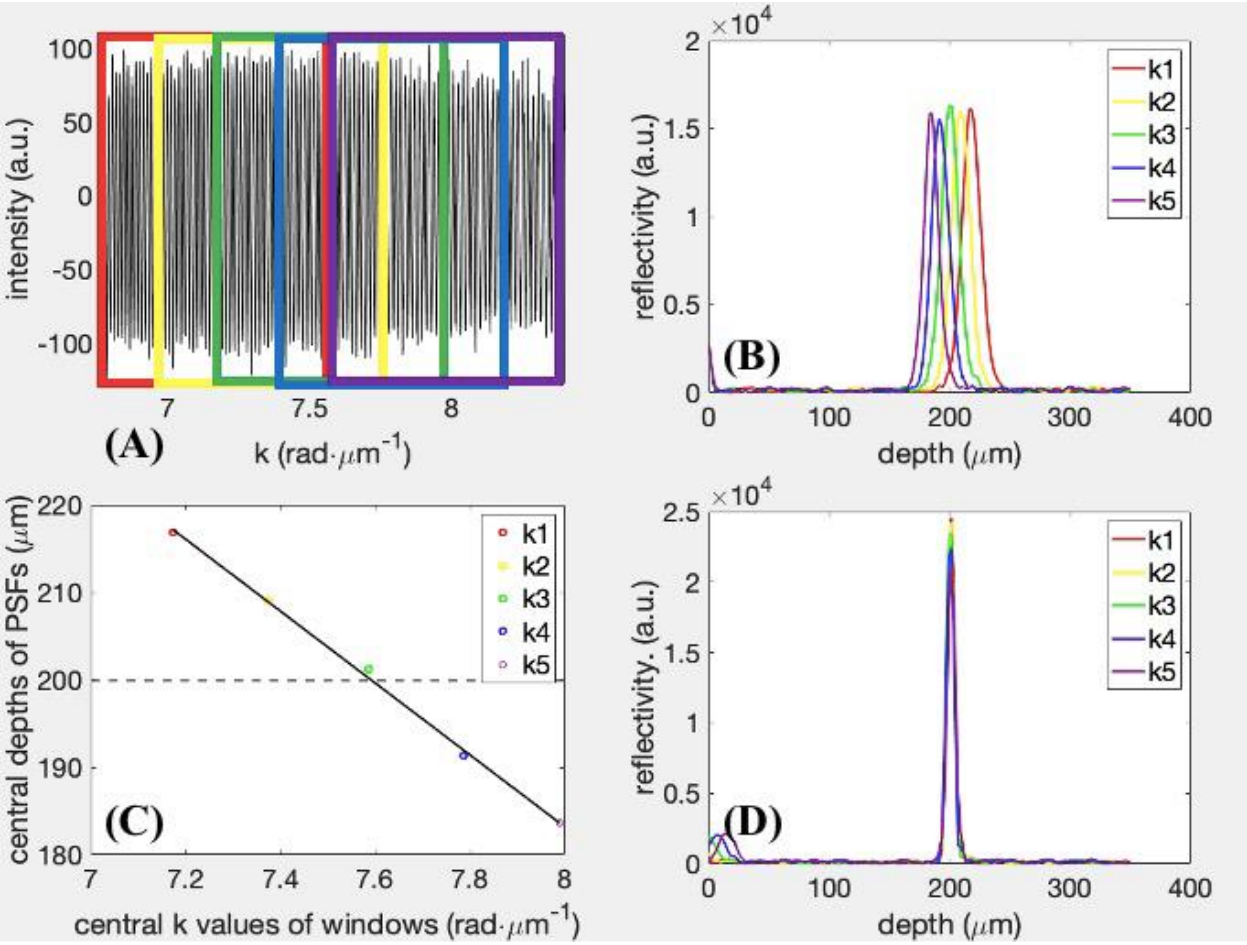

Figure 3.1: Illustration of how STFT works on a typical resampled spectral interferogram of a mirror positioned at the sample arm. For illustration, (A) a complete fringe was partially captured into 5 overlapping segments by a sliding window centered at k(i), where i=1, 2,...,5. (B) Each segmented fringe was then processed via conventional reconstructions into depth profiles, highlighted with different colors corresponding to the window color in (A). With unmatched dispersion in the system, the windowed bandwidth reconstructed PSFs are shifted and broadened accordingly. (C) The central depths of these sub-bandwidth reconstructed PSFs against different central k values of windows are plotted and linearly fitted, which show a direct display of the dispersion. (D) To correct the dispersion mismatch, a method is needed to align all of these shifted peaks to the correct depth position as well as to sharpen the PSFs, as will be described in detail below.

Automatic Dispersion Compensation Algorithm Using TFA:

To start the dispersion compensation term calculation, a resampled spectral interferogram, which has an equal-spacing distribution of the wavenumbers among P=2048 pixels, is input into an iterative loop that optimizes a user-defined objective function $Var(a_2)$ as defined in Eq. 3.4. First, STFT was performed on the spectral interferogram under optimization, which resulted in a 2-D depth-wavenumber plot. The detailed MATLAB

document for STFT usage can be found at https://www.mathworks.com/help/signal/ref/stft.html. The ridge was then calculated by finding the maximum depth value at each wavenumber being evaluated. The total number of wavenumbers being evaluated (or the total number of local sliding windows) K_{eval} in an STFT process is determined by Eq. 3.5, where M is the length of the sliding window and L is the overlap length between any two consecutive sliding windows, and the $\lfloor\ \rfloor$ symbols denote the floor function. According to Eq. 3.5, K_{eval} is proportional to the overlap length L but inversely proportional to the sliding window size M. Therefore, one can have more wavenumbers being evaluated by having much denser sliding windows or narrower windows, by consuming more computing time. On the other hand, narrow windows have broadened PSFs, which could lead to difficulty in ridge detections. The selection of window size and overlaps has an impact on the algorithm's output, and details will be discussed in Results - *Selecting The Overlap Length And Window Size for STFT Processing*. The k-dependent ridge variance, caused by dispersion, was then minimized at the dispersion compensation coefficients a_2, where $z_{a_2}^i$ is the calculated depth at ith wavenumber, and $\bar{z}_{a_2}$ is the average of depths across K_{eval} equally spaced wavenumbers.

$$Var(a_2) = \frac{\sum_i^{K_{eval}-1}(z_{a_2}^i - \bar{z}_{a_2})^2}{K_{eval}-1} \quad (3.4)$$

$$K_{eval} = \left\lfloor \frac{P-L}{M-L} \right\rfloor \quad (3.5)$$

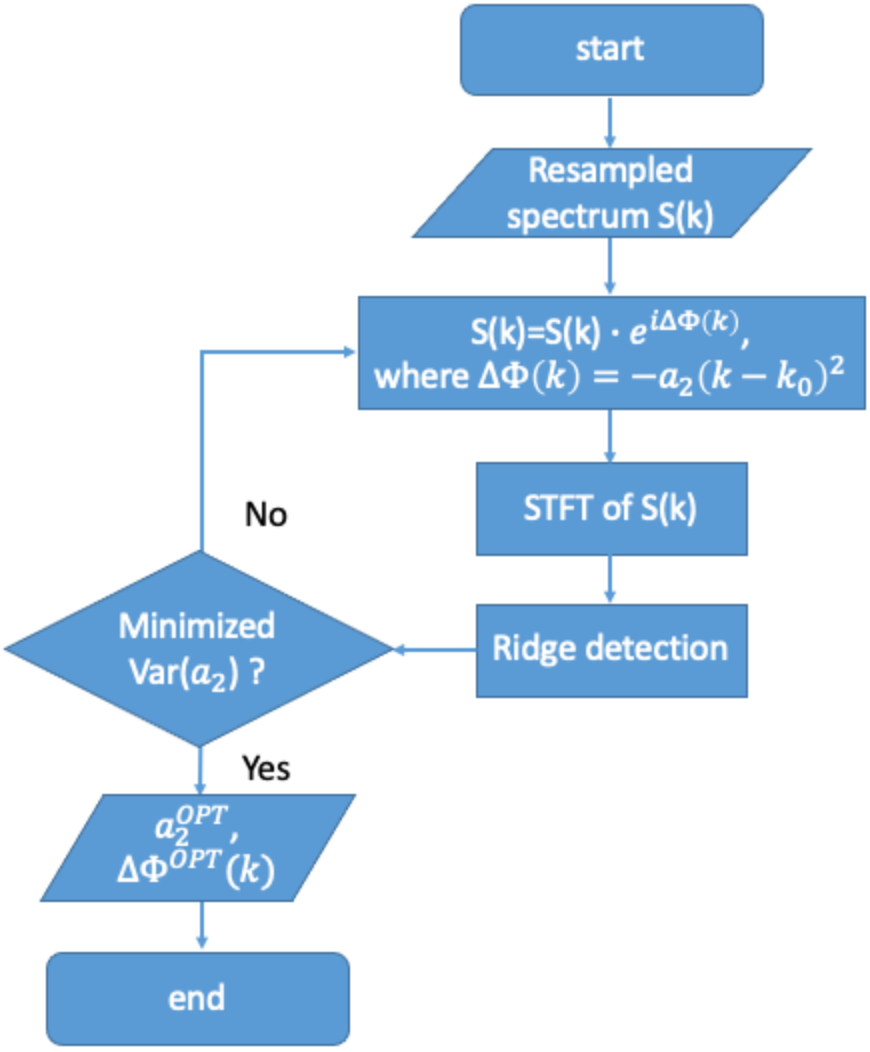

Figure 3.2: Flowchart of our proposed SD-OCT dispersion compensation algorithm. The objective function Var(a_2) denotes ridge variance, where a_2 is a variable of second-order dispersion compensation coefficient under optimization. STFT: short-time Fourier transform; OPT: optimized.

The automated system outputs the optimized dispersion compensation coefficients a_2^{OPT} and dispersion compensation term $\Delta\Phi^{OPT}(k)$, as illustrated in Fig. 3.2. $\Delta\Phi^{OPT}(k)$ is a P-pixel vector stored in local and is used for future dispersion compensation during routine OCT image reconstruction. Like the method described in Ref. [151], this procedure can be done for any higher-order dispersion compensations. However, since our system manifests unnoticeable third or higher-order dispersions, we calibrated the dispersion mismatch only

at the second order. Note that to obtain the desired dispersion compensation vector using this algorithm, only one A-line resampled spectral interferogram is needed.

Materials and Methods

OCT System:

A schematic diagram of the custom-built SD-OCT imaging system is shown in Fig. 3.3. The broadband laser light source (SuperLum Ltd., Ireland) has a bandwidth of $\Delta\lambda = 165\ nm$ at 3 dB spectrum width centered at 850 nm. The source light passing into a single-mode 50:50 fiber coupler (TW850R5A2; Thorlabs, Newton, NJ) is equally separated into two parts, directed to the reference arm and sample arm, respectively. A pair of galvanometric scanning mirrors (Cambridge Technology Inc., Bedford, MA) was implemented which enables simultaneously horizontal (X-axis) and vertical (Y-axis) scanning of the iridocorneal angle of the eye. To match the optical path lengths in the two arms, a motor-controlled mirror was used in the reference arm. A dispersion compensator (LSM54DC1; Thorlabs, Newton, NJ) was used in the reference arm to compensate for the objective lens which has an effective focal length of 54 mm (LSM54-850; Thorlabs, Newton, NJ). The two lights interfere with each other at the coupler and are then detected by a spectrometer (Cobra-S 800, Wasatch Photonics, NC), which comprises a diffraction grating and a high-speed 12-bit complementary metal-oxide-semiconductor (CMOS) line-scan camera.

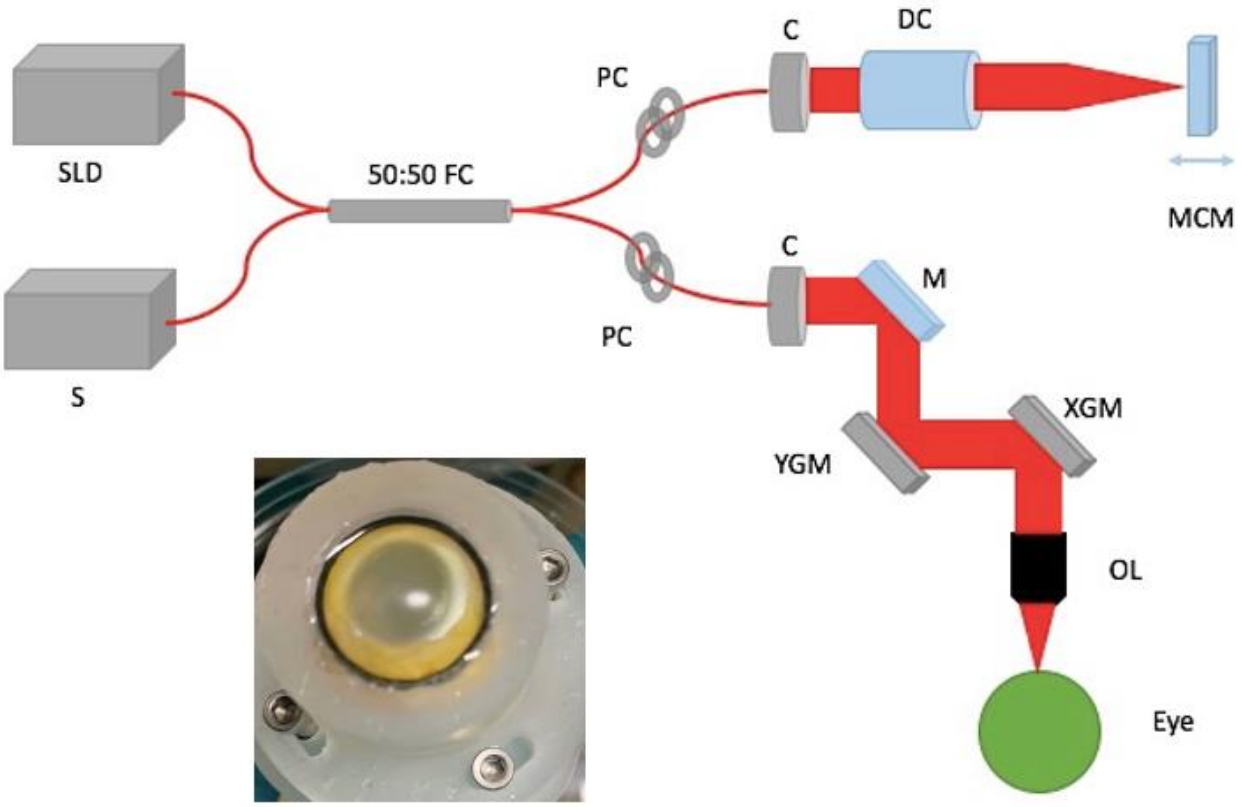

Figure 3.3: Schematic diagram of the SD-OCT system. An optical path length mismatch is corrected by using a movable mirror motor-controlled in the reference arm. The mirror or anterior segment of the cadaver eye placed on an eye holder is in the sample arm, as shown in the close-up for the cadaver eye setup. SLD: superluminescent diode; S: spectrometer; FC: fiber coupler; PC: polarization controller; C: collimator; DC: dispersion compensator; MCM: motor-controlled mirror; M: mirror; YGM: Y-axis galvanometer mirror; XGM: X-axis galvanometer mirror; OL: objective lens.

The line-scan camera has P=2048 pixels and runs at a 20 kHz rate. Processed images contain 1024 × 1000 pixels per frame, and display images at a rate of 10 frames per second. The measured average axial resolution across 2-mm depths and theoretical lateral resolution are 2.7 μm and 8.2 μm in air, respectively. The OCT imaging system has a sensitivity of ~110 dB and is capable of imaging the eye to a depth of approximately 1.5 mm with ~4.0 mW incident light power on the sample.

Sample Preparation:

The human cadaver eyes for OCT imaging were obtained from San Diego Eye Bank within 24-hour postmortem. The study was in compliance with the Declaration of Helsinki. Since we also use these eyes for experiments of femtosecond laser trabeculotomy where the laser is targeted on the TM region, unrelated structures are removed (living eyes do not encounter this issue because eyes are vibrant and clear) [65, 66]. Specifically, the eyes were carefully dissected to keep the TM intact, while removing other components, such as the posterior segment, iris, lens, ciliary body, and uveal tissues. The prepared eyes were then stored in the Optisol corneal storage medium (Bausch and Lomb, Rochester NY) and refrigerated at 4 °C. Before imaging, the enucleated eye was mounted on a customized eye holder as illustrated in Fig. 3.3, perfused with Dulbecco's modified Eagle's medium (DMEM) containing 5 μg/mL amphotericin, and 100 μg/mL streptomycin (MilliporeSigma, MO), and placed in an incubator (Sheldon Manufacturing, Inc., Cornelius OR) at 37 °C, 5% CO_2, and 90% humidity for 30 min. The eye was then placed on a movable mechanical stage with 5 degrees of freedom, i.e., X, Y, Z translations, rotation, and tilting under the OCT imaging system. The OCT beam was focused on the limbus to image the iridocorneal angle. The cornea surface was kept moist to prevent dehydration during imaging. Note that cadaver tissue swelling will make the relationship between ex vivo and in vivo dimensions uncertain.

Methods:

To test the feasibility of the proposed dispersion compensation algorithm, a 19.6 mm, N-BAK1 glass manufactured block (LSM04DC; Thorlabs, Newton, NJ) was deliberately added

into the OCT beam, which introduces dispersion mismatch between the two arms. A mirror was placed at the focus on the sample arm while the delay line was adjusted in the reference arm such that the PSF was located at 200 μm from zero-delay. Ten spectral interferograms were taken at this location and put into the algorithm independently to obtain the dispersion compensation vectors. We tested the effectiveness and robustness of the algorithm by shifting PSFs at different locations as well as applying the dispersion compensation term to human cadaver eye data. In addition, to verify of the algorithm works with more dispersion, we added two same glass blocks as did previously described, with the PSF located at 800 μm from zero-delay.

In performing STFT, a 1024-pixel-sized Hann window with 99% overlapping was applied to the 2048-pixel sized spectral interferogram totaling 94 sliding spectral windows in this work. The Simplex search method ("fminsearch" function with default stopping criteria in MATLAB R2021b, MathWorks, Inc., Natick, Massachusetts) was used to minimize the ridge variance. Our dispersion compensation algorithm as detailed in Theory - *Automatic Dispersion Compensation Algorithm Using TFA* takes only around 0.5 seconds in a MacBook Air 13-inch, 2017 (1.8 GHz Dual-Core Intel Core i5, 8 GB 1600 MHz DDR3).

Results

Selecting The Overlap Length and Window Size for STFT Processing:

Figure 3.4A and B show the effects of overlap ratio, which is defined by the ratio of overlap length to the window size, on the dispersion compensated axial resolution and the averaged compute time at an array of window sizes. Figure 3.4C demonstrates that a strong

linear relationship exists between the averaged compute time and the total number of windows. To evaluate the influence of window size on the dispersion compensated axial resolution and compute time, we first fix the overlap ratio to 0.9, and the results are displayed in Fig. 3.4D. More details can be found in Appendix 3.1 Table S3.1.1.

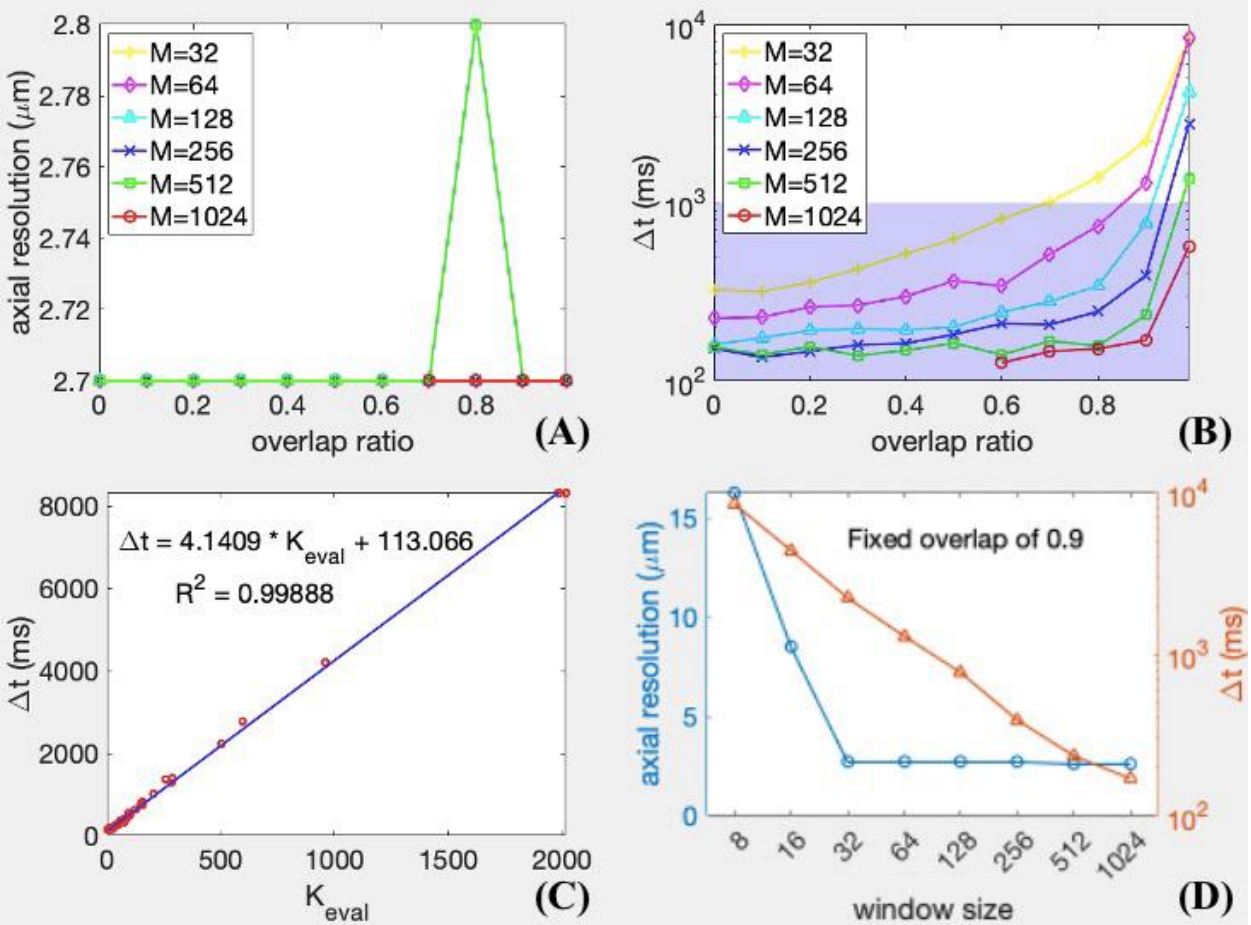

Figure 3.4: Parameter study using STFT. (A) Axial resolution and (B) averaged compute time Δt in milliseconds to generate a dispersion compensation vector against a range of the overlap ratios, i.e., 0, 0.1, 0.2, 0.3, 0.4, 0.5, 0.6, 0.7, 0.8, 0.9, and 0.99. Note that data are not available at some overlap ratios for window size M=1024 (in red). (C) A coefficient of determination of 0.99888 indicates that there is a strong correlation between the total number of windows Keval and Δt. (D) Obtained axial resolution (y-axis left) and Δt (y-axis right) versus a series of window sizes.

In Fig. 3.5, we show a few examples to represent the impact of the window size on the spectral and spatial distribution, a pair of competing factors in an STFT. The k-axis is the wavenumbers being evaluated, which consist of a series of the central k values of each sliding

window. For different combinations of window size and overlaps, the total number of the sliding windows and the interval in k will change, resulting in a difference on the k-axis. For example, a large window has a larger starting k value on the k-axis than a smaller window does, and a larger overlap has a finer k increment on the k-axis. Even so, either a large or small window will cover the spectrum from one end but might miss some information from the other end of the spectrum. As expected, significant loss of spectrum will only occur if large window sizes are used with small overlaps.

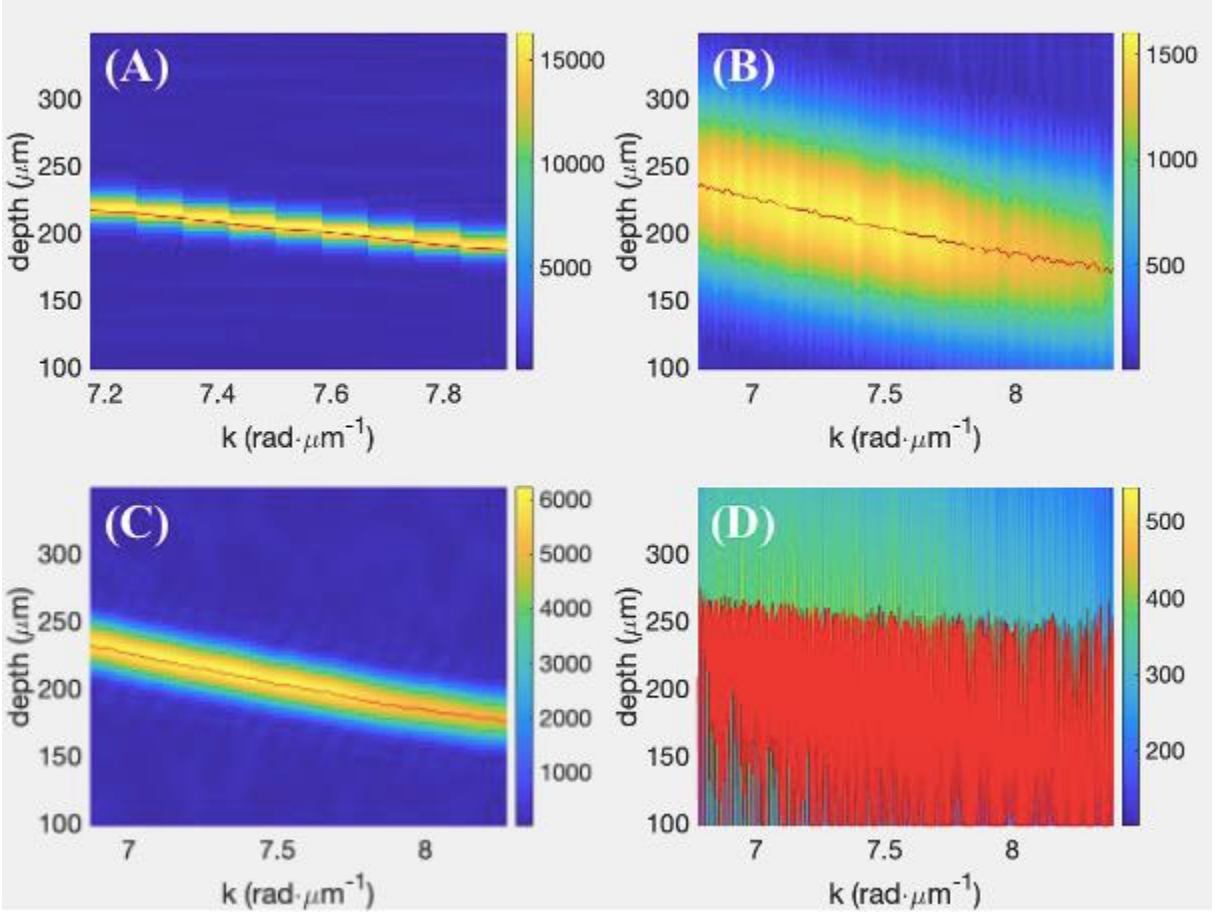

Figure 3. 5: Spectral and spatial distribution using STFT with various window sizes (A) M=1024, (B) M= 256, (C) M=64, and (D) M=16. Overlap ratios=0.9. Red is the detected ridge of the distribution. Failure of edge detection in D.

Dispersion Compensation Using Mirror Data:

We plotted the energy maps before and after dispersion compensation in Fig. 3.6A and B for comparison. Using the proposed method discussed in Theory - *Automatic Dispersion Compensation Algorithm Using TFA*, we obtained the dispersion compensation term in Fig. 3.6C. It showed a quadratic curve with a larger amount in the lower and higher frequency bands relative to the central working frequency, because we consider only a_2 optimization in our study. Higher-order dispersion can also be performed if the dispersion is considerable. To avoid false ridge detections from the strong direct current component, spectral interferograms of the mirror at the focus of the sample arm were collected while shifting the PSF at 200 μm. Fig. 3.6D shows the PSFs comparison before and after dispersion compensation.

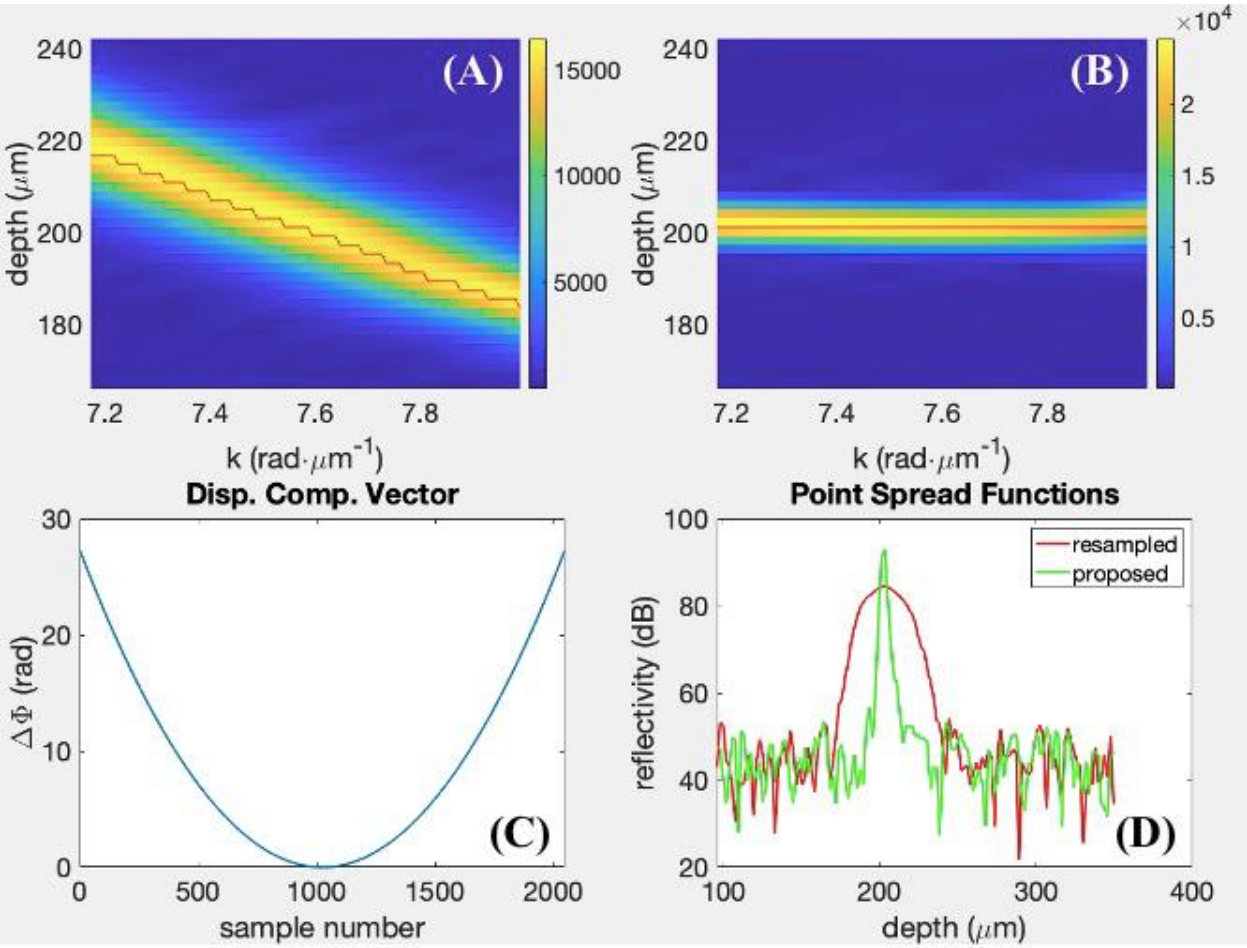

Figure 3.6: Spectral and spatial distributions (A) before and (B) after dispersion compensations. The red lines centered on the energy distributions indicate the detected ridges. (C) is the extracted dispersion using the proposed method, and (D) shows PSFs before and after dispersion compensations.

To test the robustness of the proposed method, we repeated 10 independent spectral interferograms on the algorithm as summarized in Table 3.1. The measured and theoretical a_2 values of the glass dispersion block were derived in Appendix 3.2.

Table 3.1. Statistics of the extracted a_2 values from 10 mirror fringes with induced dispersion block(s)

Num. disp. block	Extracted a_2 values ($\times 10^{-11} m^2$)	Mean ($\times 10^{-11} m^2$)	Standard deviation	Coefficient of variation
1	-4.098, -4.098, -4.098, -4.098, -4.098, -4.144, -4.133, -4.121, -4.133, -4.098	-4.118	0.0187	-0.0046
2	-8.568, -8.522, -8.522, -8.522, -8.522, -8.522, -8.475, -8.475, -8.475, -8.475	-8.5078	0.0315	-0.0037

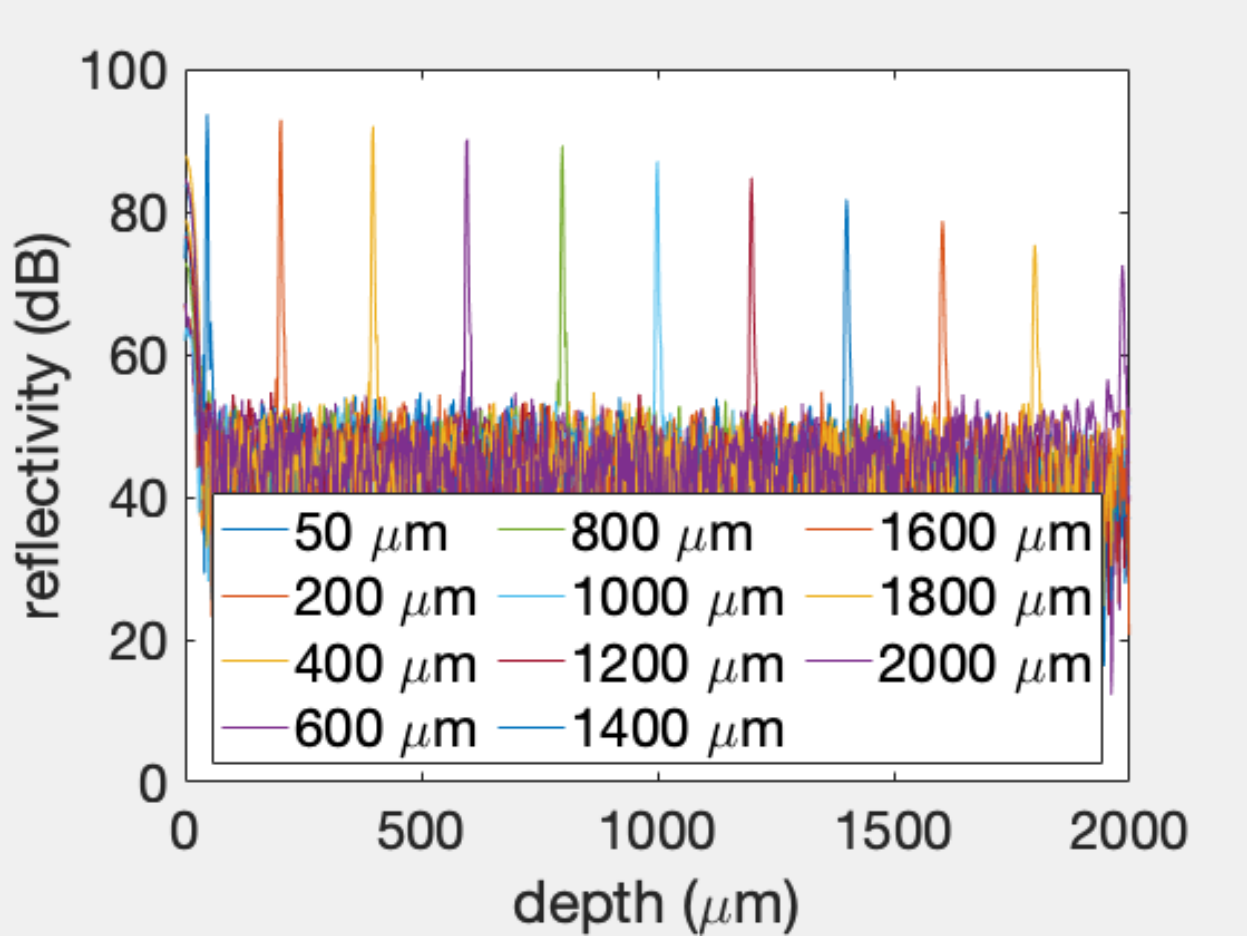

Figure 3.7: Sensitivity roll-off performance of the calibrated SD-OCT system by the proposed method, in which the reflectivity in dB is calculated by taking the 20·log of the amplitude of Fourier transform of the spectral interferograms.

The dispersion compensation vector was found to be depth-independent and, once obtained, can compensate for any other depths' measurements. Figure 3.7 summarizes the sensitivity roll-off performance of the imaging system over a range of 2 mm in air, corresponding to 1.5 mm in eye tissues.

Comparison to Polynomial Fitting Method Using Hilbert Transform:

The polynomial fitting method is done by performing a Fourier transform of the spectral interferogram, symmetrically gating the signal, inverse Fourier transformation,

Hilbert transformation to obtain the phase angle, unwrapping the phase, and finally fitting an n-order polynomial to smooth the curve [153]. Figure 3.8A and B show the corrected PSFs using the polynomial fitting method at a range of fitting orders and using our proposed method in two different amounts of dispersion introduced into the OCT system. When one dispersion glass block was introduced, the axial resolution using the polynomial fitting method can achieve as sharp as 2.4 μm. However, the resolution was raised to 3.0 μm or larger when 2 dispersion glass blocks were added. Larger sidelobes were observed using the polynomial fitting method when more dispersion existed. The proposed method achieved approximately 2.6-2.7 μm in both cases. The extracted dispersion curves between different methods are compared in one dispersion block (Fig. 3.8C) and two dispersion blocks (Fig. 3.8D). Our quadratic, convex dispersion compensation can "linearize" the raw, concave unwrapped phases. The dispersion curves extracted by the polynomial fitting method are also convex, thus capable of correcting some dispersion. In addition, the extracted dispersions using the polynomial fitting method are contingent on the fitting orders, especially when a large amount of dispersion is induced.

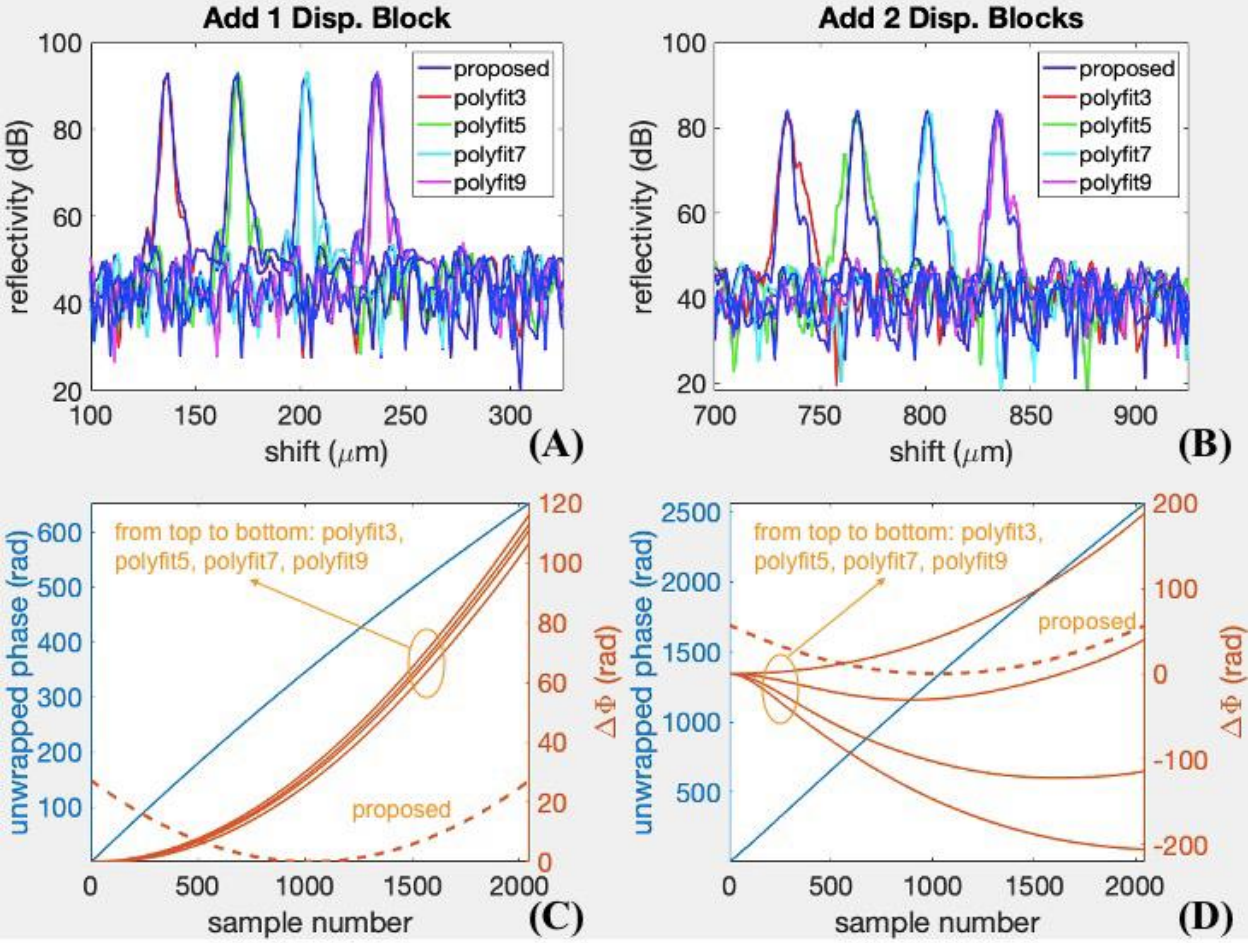

Figure 3.8: PSF comparisons between the proposed method and the polynomial fitting method with various fitting orders in an SD-OCT by introducing (A) one dispersion glass block, and (B) two dispersion glass blocks. Note that the "proposed" PSF is superimposed on each of the "polyfit" PSFs. All of them should be located at the same depth, but they are intentionally shifted to avoid crowd. (C, D) Measured dispersion curves of both techniques (solid orange: polynomial fitting methods; dash orange: proposed method) with the raw unwrapped phase (blue, left y-axis) from the Hilbert transform are plotted for the two cases of dispersion, respectively.

Imaging for Iridocorneal Angle in Human Cadaver Eyes:

The current gold standard for angle imaging associated with glaucoma is gonioscopy [154], which can view the TM surface through the cornea but it's extremely subjective and operator-dependent. For the potential glaucoma treatment application, we implemented the OCT imaging system specifically for the iridocorneal angle in human eyes. A 2mm×1.5mm area in human cadaver eyes was shown in Fig. 3.9. To remove the speckle noise, 10

sequential images at the same location were taken to obtain an averaged image. The dispersion compensated images were sharper and showed more clearly the anatomical details in the iridocorneal angle. For instance, SC, CCs, and adjacent vessels were clearly visualized on the dispersion compensated images while barely visible on uncorrected images. Note that the polynomial fitting method also represents quite similar results to our proposed method therefore not repeated here.

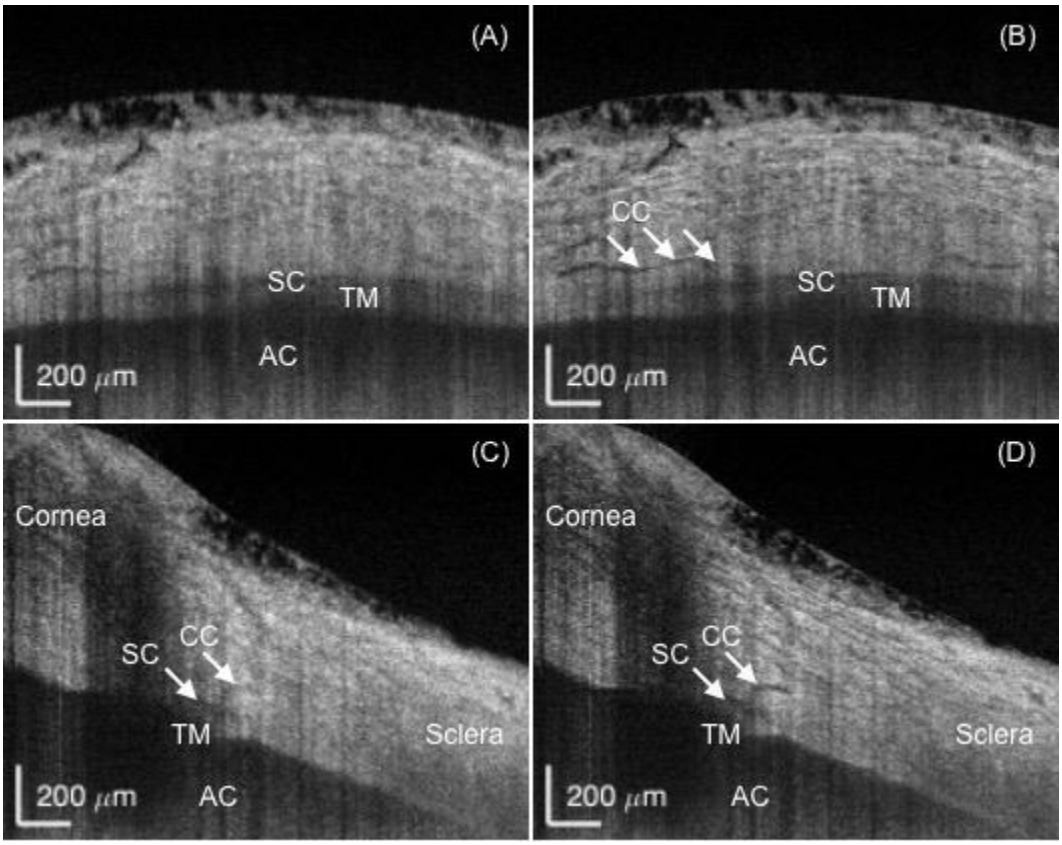

Figure 3.9: Typical averaged (A, B) horizontal and (C, D) vertical scanning OCT images of the iridocorneal angle of human cadaver eyes with a field of view $2mm \times 1.5mm$, compared between (A, C) without and (B, D) with the proposed dispersion compensation algorithm. The beam probe was arranged approximately perpendicular to the limbus to ensure the best visibility of TM, SC, and surrounding microstructures. SC, CCs, and adjacent vessels were found on the dispersion compensated images while some of them were not visible or blurred on the uncorrected images. Scale bar is 200 μm. AC: anterior chamber; TM: trabecular meshwork; SC: Schlemm's canal; CC: collector channel.

Discussion

Optical dispersion remains an unneglectable issue in the development of an OCT system, especially when using light sources with broad bandwidth, such as the 165 nm spectral bandwidth used in our study. In addition, the dispersion is difficult to detect in the spectral interferogram domain. To address these challenges, we developed a new TFA automated iterative framework that extracted the dispersion compensation by optimizing the energy distribution of a dispersive spectrum from a reflection of a mirror. The mirror data showed that dispersion induced discontinuity or disturbances and k-dependent fluctuation of ridges in the spatial-spectral domain. This variance was minimized via an iterative procedure together with STFT. An intuitive observation is that, if we align the central depths of PSFs to eliminate the k-dependence in the spatial-spectral domain, the FWHM of the resultant 1-D PSF can be greatly reduced after ridge variance minimization (Fig. 3.1, Fig. 3.6A and B).

Selecting appropriate parameters (overlaps and window size) in an STFT affects the results of dispersion compensation on both achieved axial resolution and compute time. Although the overlap ratio has little effect on the axial resolution, it does matter when a large window is used. This is because, for example, if an M=1024 window was used, some overlap was needed to ensure a sufficient number of windows Keval was used. Otherwise, it will lead to the failure of dispersion extraction, such as in the cases of overlap ratios ≤ 0.6 (Fig. 3.4A and B, Appendix 3.1 Table S3.3.1). Non-overlap can be considered if median or smaller sizes of windows (M=512, 256, 128, 64, 32) are used, considering less compute time is required (Fig. 3.4B, Appendix 3.1 Table S3.3.1). In addition, window size selection is closely related to

the axial resolution and compute time. The window size does not influence the axial resolution for most window sizes; but to some degree when the windows are too small (M=16 and 8), the axial resolution dramatically worsens (Fig. 3.4D). This is possibly due to the use of extremely narrow windows, which means higher spectral resolution in the k-axis, causing the spatial resolution to greatly degrade, leading to the failure of ridge detection (Fig. 3.5D). A smaller window also has a problem with a longer compute time (Fig. 3.4B, Appendix 3.1 Table S3.1.1). To summarize, when using an STFT for dispersion compensation in our algorithm, one could either select a larger window size (M=1024) with some overlaps (0.7 or higher in our case), or select a median or median small size window (M=512, 256, 128, 64, 32) with no or small overlaps. The shaded area in Fig. 3.4B incorporates a broad range of optional choices if 1 second of averaged compute time is considered to be acceptable.

Previous studies have attempted to use STFT and/or iterative optimization methods for correcting the dispersion mismatch between the two arms [155, 156]. By simply scanning a mirror at the sample arm in this work, we presented an alternative method to compensate for the dispersion in an SD-OCT. Unlike using cross-correlation to find the peak shifts [155], we used a simple maximum search method to detect the locations of ridges, followed by an iterative optimization procedure for ridge variation minimization. In addition, Ni et al.'s work [156] focused on the optimization of the sample centroid image's information entropy, as a further refinement of the technique demonstrated by Wojtkowski et al. [151] and Yasuno et al. [157] towards optimizing an image's contrast and entropy, respectively. A simple and widely used polynomial fitting method proposed by Cense et al. used Hilbert transform to extract the phase function $\Delta\Phi$. This method worked pretty well when small dispersion was introduced in our experiment (Fig. 3.8A). However, axial resolution degraded

as the dispersion mismatch grew (Fig. 3.8B). Our method showed consistent corrected PSFs in either situation (Fig. 3.8A and B, Table 3.1).

In addition, our algorithm is simple, automatic, and robust for repeated measurements. The dispersion compensation terms obtained from the 10 spectral interferograms of a mirror positioned in the sample arm have only a -0.46% (-0.37%) coefficient of variation (Table 1.1). Another advantage of our algorithm is that it provides a broad range of parameter selection for an STFT, as discussed before. Lastly, it is convenient to use STFT to directly and dynamically visualize how the spectral non-linearity and dispersion mismatch represents at each step through the entire OCT processing (Fig. S3.3.1 in Appendix 3.3).

The resolution and imaging capability of the angle details were improved with the proposed method using the STFT iterative technique. The dispersion compensation algorithm enabled high-fidelity visualization of CCs adjacent to the SC, which was lost on the uncompensated images. The imaging capability of these micro-structures is comparable to Kagemann et al.'s work [158]. Furthermore, our horizontal and vertical imaging can assist to access angle details more efficiently, which is crucial before and during glaucoma surgeries. For instance, in Fig. 3.9B, the horizontal scanning allows ophthalmologists to have a different view of the continuous structures i.e., TM/SC/CCs connected with each other rather than only the cross-sectional images in the vertical scanning in Fig. 3.9D. This will be beneficial for the treatment planning of the surgical volumes in our ongoing laser studies in human cadaver eyes [65, 66] because laser drilling through TM that is close to the opened SC/CCs might have a positive effect on intraocular pressure reduction. Given the importance of better image visualization and characterization of the ocular outflow structures in the

iridocorneal angle for glaucoma surgery, future studies include further image quality improvement of the TM/SC/CC areas, as well as studies of OCT image-guided femtosecond laser trabeculotomy in cadaver eyes for the treatment of glaucoma [65, 66].

Chapter 4: Iridocorneal Angle OCT Imaging

Introduction

In the last chapter, we improved the axial resolution of OCT imaging through dispersion compensation, utilizing an STFT and iterative method. Now, our focus is on fully imaging and characterizing the details of the iridocorneal angle by implementing 'cross line' scanning alongside a series of image processing techniques. 'Crossline' scanning enables simultaneous azimuthal and circumferential scanning of angle structures, including the trabecular meshwork, Schlemm's canal, and collector channels. These structures play crucial roles in regulating aqueous outflow in the eyes and are closely associated with glaucoma. Our image processing methods, including intensity projection, enface projection, 3D reconstruction and orthogonal viewing, segmentation and depth color-encoding, facilitate a more accessible way to view the angle details.

Materials and Methods

System Setup:

The SD-OCT system was described in our previous publication [1]. Briefly, our imaging system is working at 850 nm center wavelength with 165 nm bandwidth, which is combined by three superluminescent diodes (SLDs) (Fig. 4.1A). A pair of galvanometric scanning mirrors (Cambridge Technology Inc., Bedford, MA) was implemented which enables simultaneous radial and circumferential scanning of the iridocorneal angle of the eye

(Fig. 4.1B-E). An objective lens that has an effective focal length of 54 mm (LSM54-850; Thorlabs, Newton, NJ) was used to focus the OCT beam onto the limbus region. Spectral interferograms are detected by a spectrometer (Cobra-S 800, Wasatch Photonics, NC), which are then Fourier transformed into B-scan images.

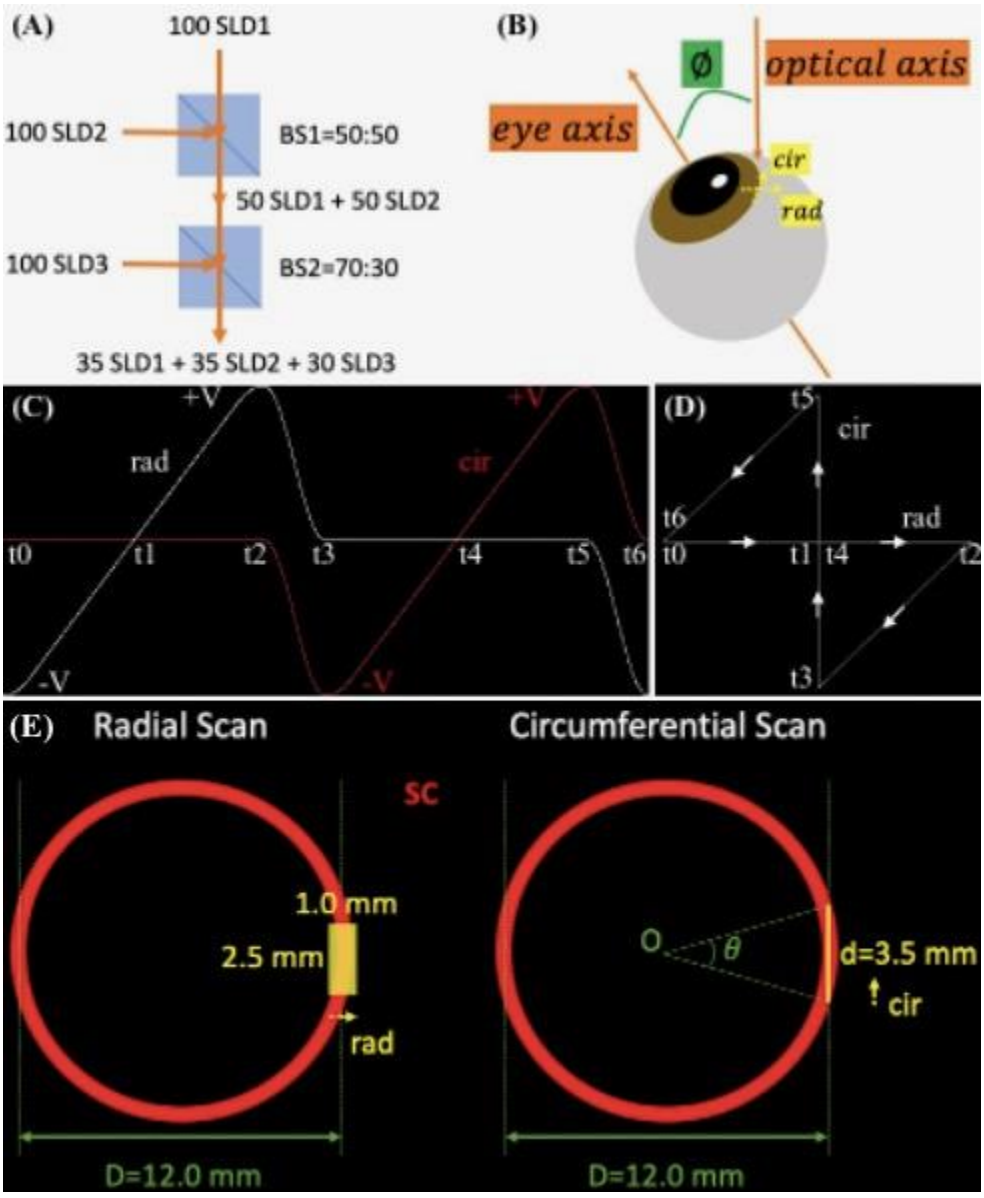

Figure 4.1: SD-OCT imaging and experimental setup. To obtain a higher axial resolution, (A) three SLDs were combined by two beam splitters, BS1 and BS2, to have a broader optical source spectrum. Assuming that the three SLDs each have 100 arbitrary units of spectral powers, after BS1 and BS2 with the respective transmission-to-reflection ratios of 50:50 and 70:30, the optical source output is generated by the combined spectrum which is consisted of 3 comparable spectra from each SLD. (B) The human cadaver eye is positioned on a translational stage (not shown) and is tilted at an off-eye axis angle for best imaging of the iridocorneal angle features. (C) The timing diagram of the crossline scanning for one period of radial and circumferential

scans. Strictly speaking, the 'simultaneous' radial and circumferential scans are in fact working alternately. The galvonometer voltage controlling the circumferential scan flattens at zero when it scans radially, vice versa. (D) shows the corresponding 2D trajectory of the OCT beam at different time points in (C). Note our crossline (radial and circumferential) scanning is part of the bowtie-shaped track, where the two hypotenuses' paths are used to shift between the two scans. In the projection view along the eye axis, a continuous 2.5 mm translation of the eye in shown B (normal to the paper towards readers) resulted in (E) a $1.0 \times 2.5\ mm^2$ radial scan and a 3.5-mm circumferential scan. The latter corresponds to a counter-clockwise, approximately $\theta = 2 \cdot \tan^{-1}(\frac{d}{D}) = 33^0$ of the full circumference of the angle structures, where D is the diameter of the ring-shaped SC estimated from reported averaged measurements of the spur-to-spur distance [159]. SLD: superluminescent diode; BS: beam splitter; rad: radial; cir: circumferential; SC: Schlemm's canal.

The line-scan camera has 2048 pixels and runs at a 20 kHz rate. Processed images contain 798×500 pixels per frame. The measured average axial resolution across 2-mm depths and theoretical lateral resolution are 2.7 μm and 8.2 μm in air, respectively. The physical lateral spacing is 2 μm. The OCT imaging system has a sensitivity of ~110 dB and is capable of imaging the eye to a depth of approximately 1.5 mm with ~4.0 mW incident light power on the sample. The power level remains below the maximum permissible exposure (MPE) limits for the retina, with the thermal MPE and photochemical MPE calculated to be 5.0 mW and 47.7 mW, respectively, for a scan time of 250 s [160]. Note that the OCT emission described in this paper is fully contained within the iridocorneal angle of the eye. No OCT light will be incident on the retina or the posterior segment of the eye.

Sample Preparation:

The human cadaver eyes for OCT imaging were obtained from San Diego Eye Bank within 24-h postmortem. The study was in compliance with the Declaration of Helsinki. The eyes were stored in the Optisol corneal storage medium (Bausch and Lomb, Rochester, NY) and refrigerated at 4 °C, which kept the cells alive for several days. One eyeball was used in this study, and it was at good status without the need for any perfusion requirements. Before imaging, the eye was placed in an incubator (Sheldon Manufacturing, Inc., Cornelius, OR) at

37 °C, 5% CO_2, and 90% humidity for 30 min. The eye was then placed on a customized eye holder on a movable mechanical stage with 5 degrees of freedom, i.e., X, Y, Z translations, rotation, and tilting under the OCT imaging system. The OCT beam was focused on the limbus to image the iridocorneal angle as illustrated in Fig. 4.1B. The cornea surface was kept moist to prevent dehydration during imaging. Note that the iris color is not known in this study, and the color shown in the figure is based on depth-encoding.

Data Acquisition and Image Preprocessing:

Mirror data were collected for systematic dispersion compensation as described previously using time-frequency analysis and iterative optimization [1]. Before scanning the cadaver eye, background data were obtained by blocking the sample arm. We then decided on the scan region by finely tuning the translation stage' vernier micrometers in both radial and circumferential directions to localize the TM/SC/CC region on both radial and circumferential images. In our experimental setup, we deliberately positioned the DC component, which represents the lower frequencies of the image, at the bottom of the image frames [161]. This arrangement was intended to optimize the visualization of angle details by enhancing their intensity. Three-dimensional tissue data were acquired at 10 μm intervals along a 2.5-mm distance circumferentially, which corresponded to a stack of radial images. A collection of circumferential data was generated simultaneously during this process.

These raw spectra data were read and processed in the MATLAB environment (MATLAB R2021b, MathWorks, Inc., Natick, MA) to generate B-can images. Specifically, the

tissue spectra were first subtracted from the background, then uniformized by dividing by the normalized background which is within the 0 to 1 range. A Hann window was applied before Fourier transformation was done to generate the images. To avoid unresolved details approaching the Nyquist limit area, an up-sampling technique was used via 2 × zero-padding in the image space. Inverse Fourier transform of the padded images thus resulted in 2 × denser spectra, which were then k-linearized before dispersion compensation. Lastly, Fourier transform and logarithm operation was implemented to generate a gray-scale intensity B-scan image.

We assumed the average tissue refractive index as 1.336 of air, cornea, sclera, and aqueous humor for air-to-tissue scaling along the depth direction. Each B-scan image was then converted to isometric pixels using the 'imresize' function in MATLAB so that 2 μm per pixel was achieved. A 3 × 3 median filter was applied, and the image was scaled to [0,1] before segmentation was done.

Segmentation:

Segmentations of the anterior surface were performed slice-by-slice for the serial radial images by a graph-based algorithm and iterative method. Since the interval between B-scan images were only 10 μm separate in y-axis, we assumed that the segmented boundaries in adjacent images were within a small range, for example 20 μm. Initial segmentation was obtained by hand on the first image, image was flattened along this boundary and the search region was determined to be above and below 20 μm of the boundary. Gradient was calculated before applying the graph search algorithm to the current

B-scan image. The segmented result was then fitted with a 9th ordering polynomial curve as the current segmentation result. The current segmented result was also used to determine the search region for the next B-scan image, and this process was repeated in a loop, as illustrated in Fig. 4.2A-C. The proposed semi-automatic iterative method allows for fast segmentation, which requires only initial manual segmentation on the first B-scan and it is completely automatic for the remaining images.

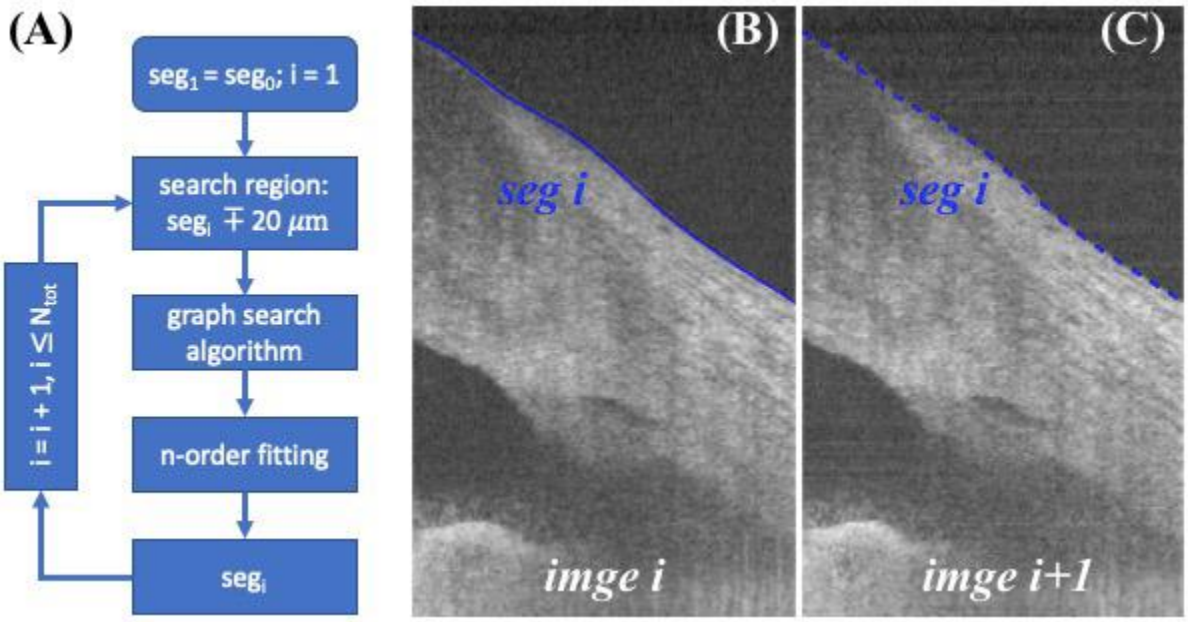

Figure 4.2: Segmentation framework. (A) Anterior surface image segmentation is initiated by manually segmenting the first image and iterating in a loop for the following B-scans in serial. The bottom block seg_i indicates the current image segmentation result and is used to determine the search region for the next B-scan's image segmentation. (B) An example shows a typical image i with its segmented boundary seg_i, and (C) image i+1 with previous segmented result seg_i overlayed, which is used as an estimate to determine the search region by shifting $\pm 20\ \mu m$ of seg_i for segmenting image i+1. For clarity segmentation result seg_{i+1} was not shown on (C) because it was close to seg_i.

Image depth encoding:

The color visualization was modeled in a Hue-Saturation-Value (HSV) color space. Specifically, the depth starting from the segmented layer was coded into the Hue channel, image intensity into the Value channel, and a constant, i.e., 1 into the Saturation channel. Note

S, V values were normalized to the range in [0,1]; the H value was tailored from 0 to 2/3 so that a rainbow effect was achieved (changing from red, yellow, green, to blue). The HSV was then converted to RGB space for visualization and final image generation. Note the rainbow effect representation is available in FluoRender software (Scientific Computing and Imaging Institute, Salt Lake City, UT, USA), but it is incapable of encoding the depth starting from specific locations such as the segmented layer in our case.

Image 3D reconstruction:

Three-dimensional reconstruction was obtained by stacking the color images in ImageJ and loading them into FluoRender software for 3D visualization and slice-by-slice viewing.

Results

Segmentation and depth encoding:

Segmentation was performed on each B-scan image's anterior surface of the eye before further processing. Figures 4.3A and B are typical OCT images before and after segmentation. The background region above the surface was masked out as shown in Figure 4.3C. Figure 4.3D illustrates the rainbow effect of a depth color-coded image, in which starting from the segmented layer to the deeper tissue depths are displayed as a gradation of color from red, yellow, green, to blue. For example, the red color indicates that the tissue is shallow, and yellow indicates that the tissue is at a deeper location from the tissue's

anterior surface. The TM/SC/CC region is mainly within the green layer, and the iris is in the blue layer.

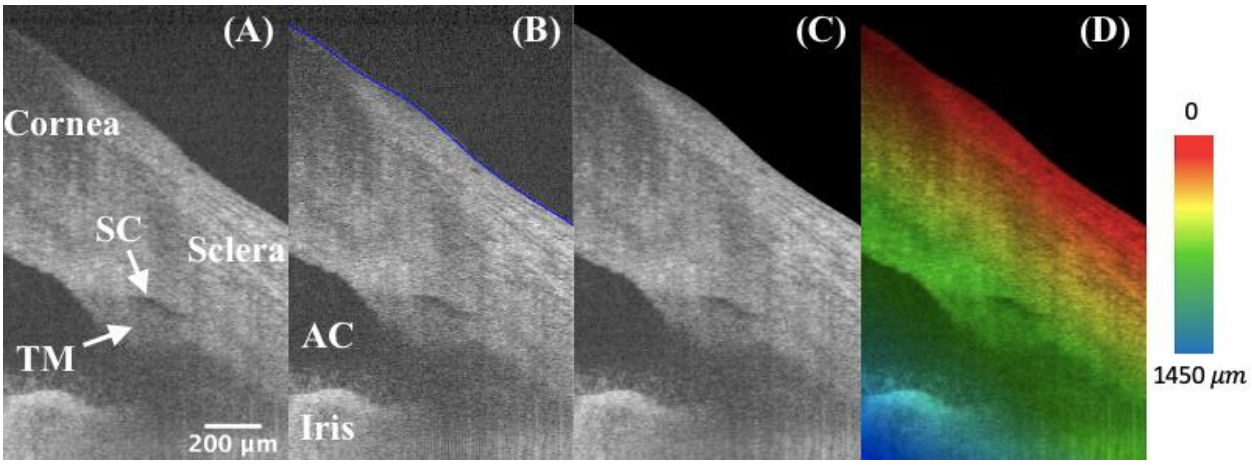

Figure 4.3: High-resolution iridocorneal angle OCT imaging, segmentation, and depth-encoding. (A) The example is a radial image, where the low-intensity prolate ellipse corresponds to the cross-section of a ring-shaped SC, which locates right above the TM. (B) The anterior surface was segmented and delineated in blue using a custom semi-automated algorithm. (C) The region outside of the surface boundary is blackened as zeros. (D) A depth-encoded image shows the rainbow effect starting from the segmented boundary into deeper tissues. TM: trabecular meshwork; SC: Schlemm's canal; AC: anterior chamber.

Three-dimensional reconstruction and orthogonal viewing:

The imaging capability of the proposed SD-OCT system for the iridocorneal angle in the limbus region was tested in a human cadaver eye study, as shown in Figs. 4.4 and 4.5. Figure 4.4 represents a 3D reconstruction of a stack of radial images, with the anterior surfaces segmented. An unintentionally damaged tissue was also found on the surface (Fig. 4.4), causing the shadow underneath along the depth direction (Fig. 4.5A). To reveal details in the TM/SC/CC region, orthogonal images can be obtained from the image volume by y-slicing (Fig. 4.5A), x-slicing (Fig. 4.5B), and z-slicing (Fig. 4.5C). Importantly, careful tracing of the continuous slices allows for revealing the details of the TM/SC structural changes and morphology of nearby CCs stemming from the SC going circumferentially along with the SC.

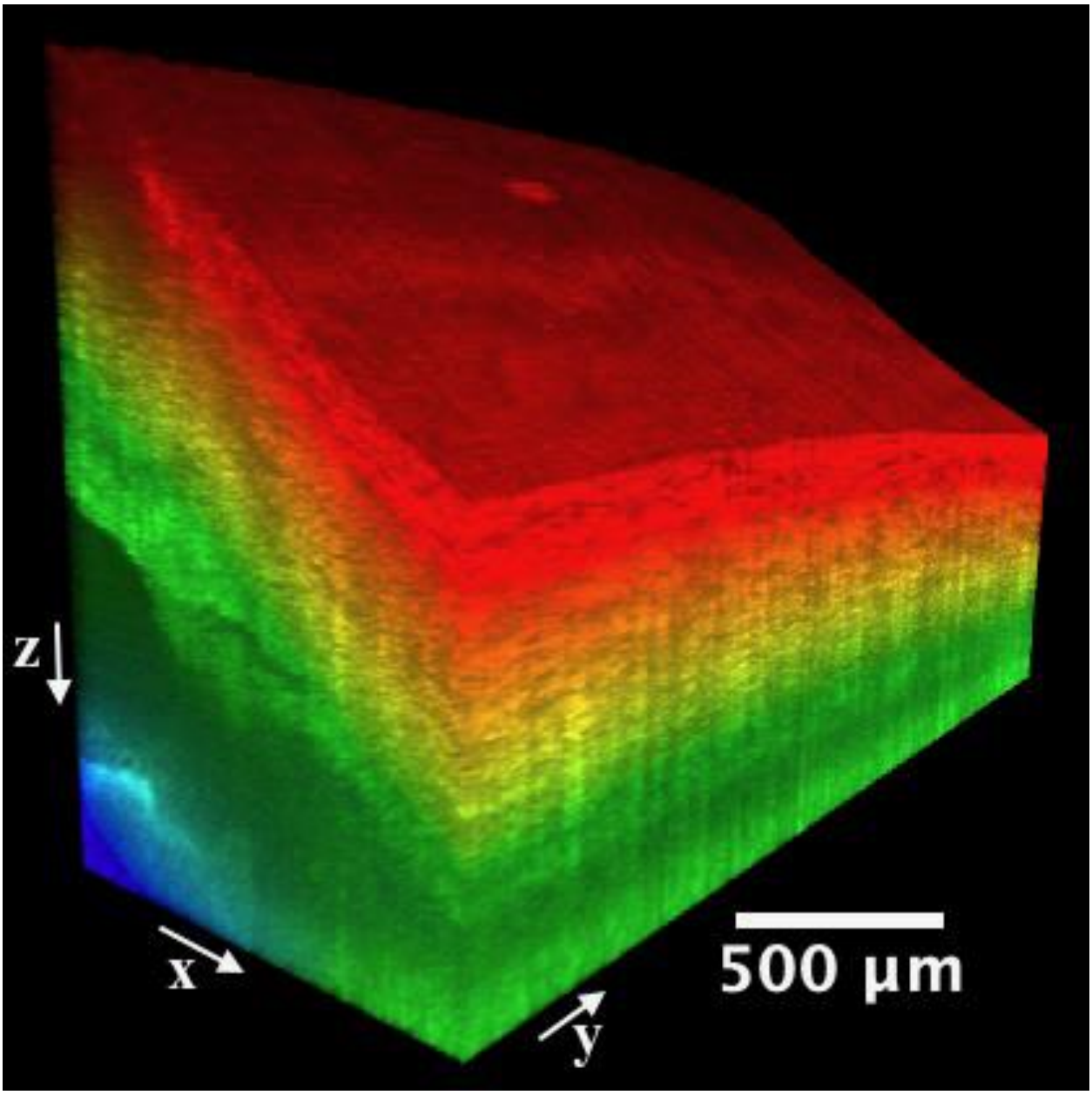

Figure 4.4: A $1.0 \times 2.5\ mm^2$ area at the iridocorneal angle of a human cadaver eye was scanned, resulting in a $1.0 \times 2.5 \times 1.6\ mm^3$ three-dimensional OCT cube. Included also the x, y, and z directions are defined and the origin is the vertex of the image cube on the top left (not shown). The colormap is coded along the imaging depth direction from the segmented layer on the surface. Same eye used in Fig. 4.3.

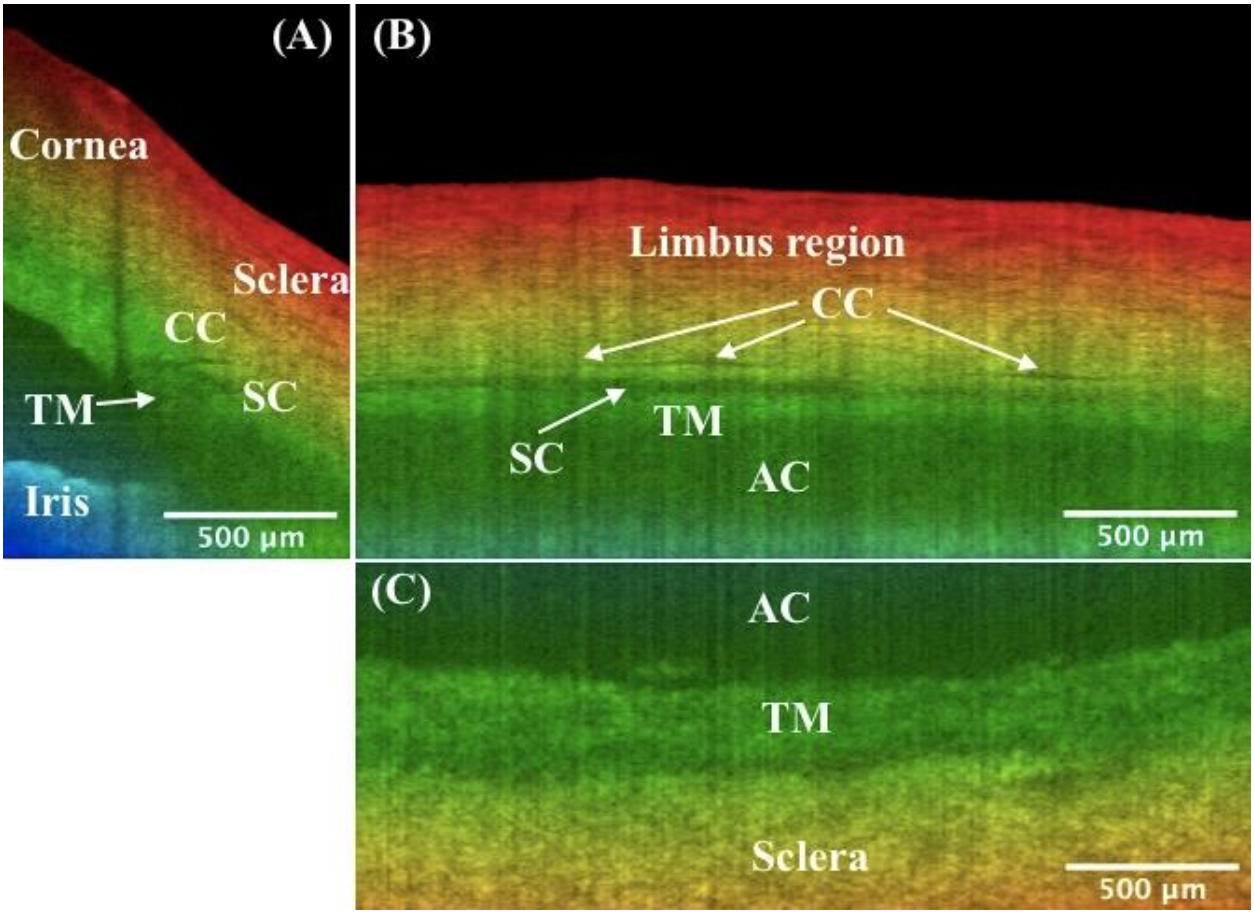

Figure 4.5: Orthogonal viewing by x-, y-, and z-slicing. (A) An xz-plane image reveals the SC's cross-sectional area change and branching of CC stemming from the SC, as compared to Fig. 2.3D. Note shadow effect is evident which is cast by the damaged tissue on the tissue surface. (B) An x-slicing results in an yz-plane image, where the SC is clearly visualized as a low-intensity band right above the TM. Note CC is running approximately parallel above the SC. (C) A z-slicing through the center of SC from the top view allows for visualization of the juxtacanalicular tissue and inner wall of SC, which are considered the main source of resistance of the human ocular outflow. Also straightforward is that the TM is located at a relatively deeper depth than the nearby sclera. TM: trabecular meshwork; SC: Schlemm's canal; CC: collector channel; AC: anterior chamber. More details such as the cross-sectional area changes of SC, distribution and branching of CCs, the morphology of TM/SC/CC region, and nearby vessels can be seen in **video1_radialStack**, and **video2_3DSlice**. Same eye used in Fig. 4.3.

Intensity projections:

A series of projections using ImageJ software (National Institutes of Health, Bethesda, Maryland, USA) were performed to obtain more supplementary information. Figure 4.6 A-F shows maximum intensity projection, minimum intensity projection, average intensity projection, median intensity projection, sum intensity projection, and standard deviation

intensity projection, respectively, along the y-axis. The shadowing regions and the TM have much lower values on the minimum intensity projection, and the anterior and posterior surfaces of the corneoscleral tissue, and the surrounding regions of the SC show large variances on the standard deviation intensity projection.

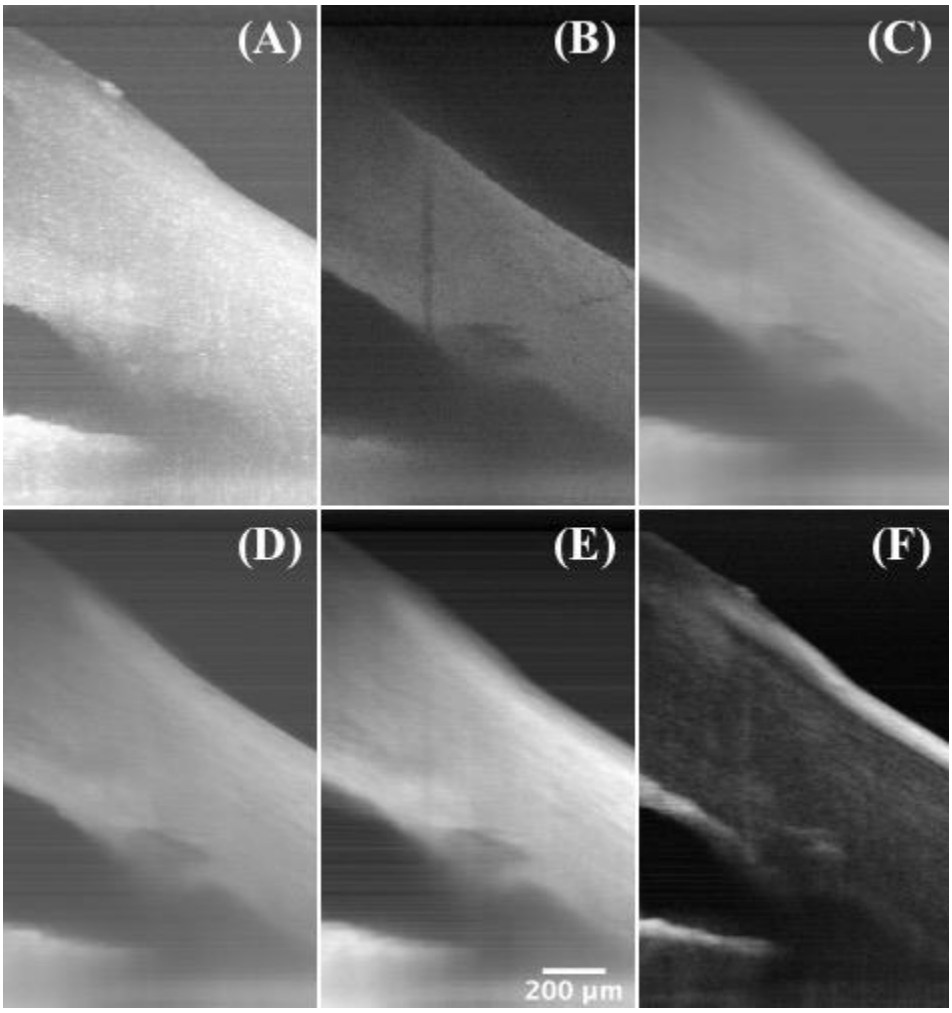

Figure 4.6: Intensity projections. (A) Maximum intensity projection, (B) minimum intensity projection, (C) average intensity projection, (D) median intensity projection, (E) sum intensity projection, and (F) standard deviation intensity projection along the y-axis of a 2.5-mm segment of radial scanning at the iridocorneal angle of a human cadaver eye, showing the TM/SC region and the damaged tissue on the surface. Same eye used in Fig. 4.3.

Enface imaging:

After segmenting the anterior surface for the entire scan volume, images were flattened from the segmented boundaries so that the surface was in the first rows in the new image cube. Figure 4.7A shows one representative flattened image. By minimum enface projection along a depth range within the flattened imaging cube (Fig. 4.7B), an enface image was obtained, where the SC region was clearly visualized as a dark trough in Fig. 4.7C.

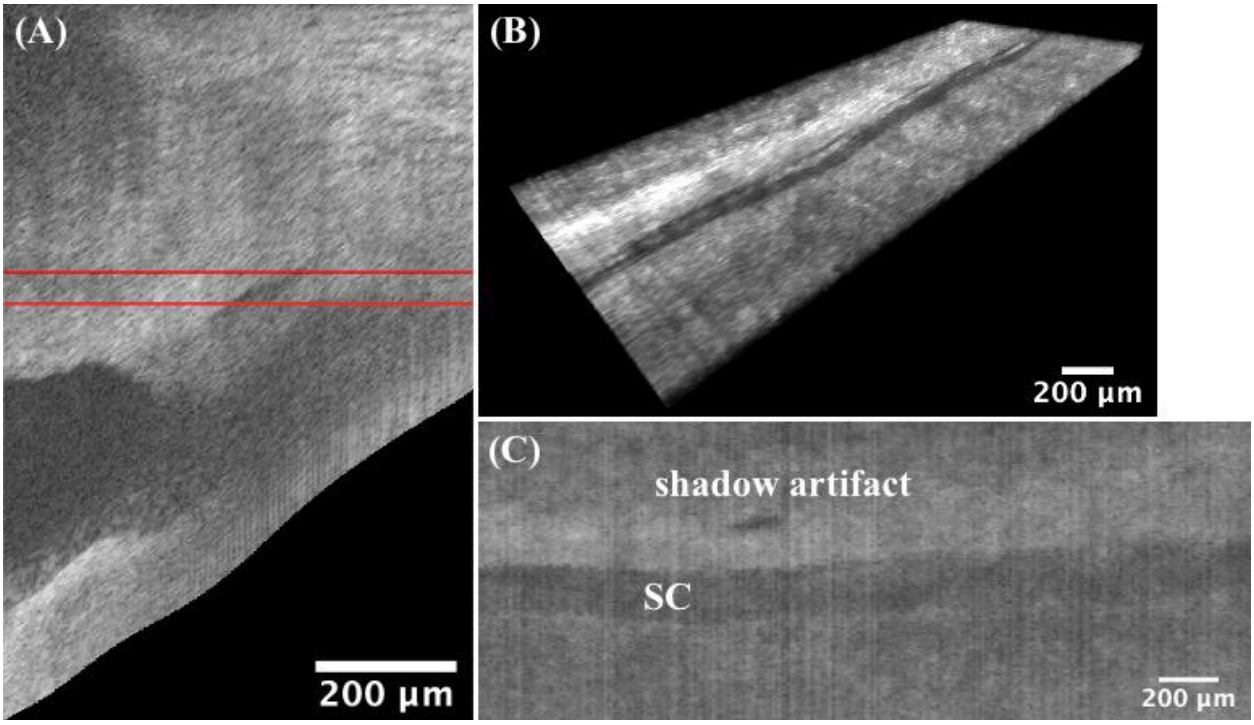

Figure 4.7: Enface Imaging. The image flattening technique is applied to each B-scan image along the anterior boundary for the entire scan volume, (A) shows only one representative flattened image of the whole flattened volume. (B) The thickness of the cropped flattened image cube is confined by the red lines (rows 286 and 320 in the flattened volume). (C) An SC region is shown on the minimum enface projection, which is performed along the depth direction on the image cube in B. The patent lumen of the SC is due to the relatively low backscattering in the fluid within the canal. Note the dark shadow artifact is caused by the damaged tissue on the surface. TM: trabecular meshwork; SC: Schlemm's canal. Same eye used in Fig. 4.3.

Circumferential scanning:

Besides previous radially scanned images, circumferential images of the TM/SC/CC were simultaneously obtained by our custom-design crossline scanning at the limbus region

(Fig. 4.9B-E). Figure 4.8A shows a circumferential image, and Fig. 4.8B is a concatenated circumferentially scanned image, providing a 'panoramic' view of TM/SC/CC region.

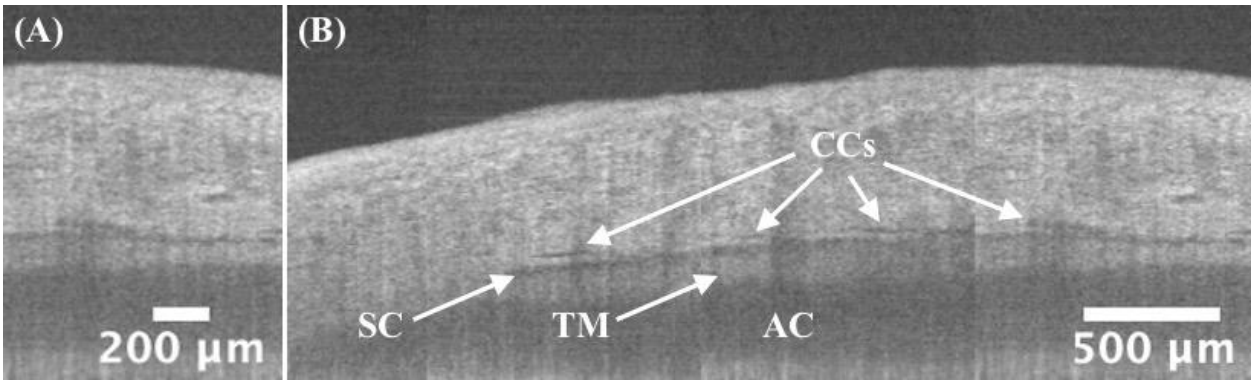

Figure 4.8: Circumferential scanning. (A) A typical circumferential image with details of TM/SC/CC shown. Some SC/CC narrow or discontinue but can be appearing larger at nearby radial locations (perpendicular to the paper direction), and this can be verified by 3D reconstruction of previous radial stacks. (B) A 'panoramic' view of TM/SC/CC regions, which is concatenated by non-overlapping, circumferential scans, demonstrating a 3.5-mm (i.e., 2.5-mm translation plus 1-mm image width itself) circumferential coverage of the iridocorneal angle. Continuous circumferential representation gives ophthalmologists direct access to the pattern change of the TM/SC/CC details, which is potentially applicable in preoperative planning for glaucoma surgeries. More dense and overlapping scanned images can be found in **video3_cir**. TM: trabecular meshwork; SC: Schlemm's canal; CC: collector channel. Same eye used in Fig. 4.3.

Discussion

The vast majority of the ocular angle OCT imaging systems developed so far were designed for the whole anterior chamber (AC). These systems have a good characterization of the AC but have limited capability in resolving ICA details. An OCT system particularly for TM/SC/CC region is therefore imperative considering those important structures in the ocular outflow are associated with glaucoma development. In this study, we demonstrated the feasibility of an SD-OCT system custom-built for the ICA imaging. In addition, image processing algorithms were implemented to better visualize the angle details.

We used human cadaver eyes for the current OCT imaging verification, which was consistent with our previous glaucoma treatment studies in human donor eyes by the FLT

surgical system [65, 66]. Although mice are more readily available, their eye sizes are much smaller and the angle structures are different from human eyes [162]. Primates have the SC but they are extremely costly and involve more complex experimental protocols. Human cadaver eyes provide researchers the best access to studying the ICA details. The donor eyes from San Diego Eye Bank were within 24 h of death, allowing for preservation of cellular structure. In this study, the tissue structures of the eyes were kept intact, as opposed to our previous FLT surgery experiments. For best imaging of the TM/SC/CC details, a tilted angle between the OCT beams and the eye axis is required. In a clinical setting this can be accomplished by directing patients to focus on an external target on the side so that the OCT beams can impinge on the limbus region perpendicularly.

Since the depth encoding starts from the ocular surface, segmentation is needed before further operations. The graph search algorithm was previously reported and it was widely used in clinics [163]. Fully automated segmentation is possible, but it is not robust for OCT images under different experimental scenarios. For example, the cornea side on the top left of the image has relatively low intensity and tends to be segmented erroneously by directly applying the graph search algorithm. A simple semi-automated segmentation framework can ensure the segmentation works more robustly and accurately within a restricted search region.

Depth color encoding allows for depth differentiation between TM/SC/CC and nearby structures. This would be beneficial to eye surgeons, for example, to distinguish the nearby structures, especially on the xy-plane images via z-slicing. Indeed, the JCT in a deeper depth (Fig. 4.5C, green) can be easily distinguished from the nearby sclera in a shallower depth (Fig. 4.5C, yellow). Note that the color gradient used in this work is only depth-encoded and

it has nothing to do with segmentation and color assignment for different eye structures. While for the structures we are interested in this study, the sclera typically has a shallower location from the ocular surface than the deep-seated TM/SC/CC structures.

Three-dimensional reconstruction of radial image stacks and slice-by-slice orthogonal viewing allows for visualizing the TM/SC/CC region in more detail. Our previous study has used this imaging system to evaluate femtosecond laser trabeculotomy (FLT) channels in human cadaver anterior segments [65, 66]. However, the sample tissues were imaged directly on a corneoscleral anterior segment artificially mounted such that the TM was directly facing the axis of the OCT beam. In this study, OCT light was irradiating the limbus region of an intact human cadaver eye to study the imaging capability of our prototype OCT system [1]. In addition, our previous study indicated that the TM geometry was not available when doing the FLT surgery so the outer wall of the SC might be unintentionally disturbed sometimes. Therefore, this work was to test the feasibility of imaging and quantifying the TM/SC/CC region in 3D. We have successfully detected the TM/SC/CC structures and distribution, showing a promise for presurgical planning for the FLT surgery. By using this imaging system, future work will utilize the 3D OCT to image guide the FLT glaucoma surgery and to evaluate the FLT channel creations and treatment efficacy in more detail.

Intensity projections and en face imaging are common techniques used in medical imaging which generate useful information. These views of images might provide supplementary information in location estimates of the target regions in an FLT or other glaucoma surgeries.

In addition, the simultaneously implemented circumferential images allow for visualization sweeping over the TM/SC/CC region circumferentially to get a panoramic view. Although 3D reconstruction of the radial image stacks can usually provide more detailed structures spatially, these serial 2D circumferential images can provide TM and SC, and the relative distributions of the CCs from the SC in real-time (video3_cir). This might help ophthalmologists get a quick idea of what the TM/SC/CC region looks like before a dense 3D volume scan is taken.

Several limitations should be addressed for cadaver eye or other animals' ocular OCT iridocorneal imaging studies. Our current implementation of a volume scan was collected by radial image stacks by manually adjusting the translation for prototype verification. Future work can be integrating a fast 3D scan protocol. Second, the circumferential scanning length is limited due to the curved ring-shaped structures of the TM/SC circulating the cornea. To test the 3D imaging capability, we showed a 2.5-mm scanning length circumferentially. The latest published techniques for 360° imaging of the SC employed the combination of multiple volumetric scanning [162, 164, 165], which might cause discontinuity between volume scans. A larger field of view could be a solution, but the resolution is limited, and the direction of OCT beams is not optimal for the angle imaging. A potential solution to obtain the 360° angle structures could be the 3D reconstruction of a large number of radial scans in the TM/SC/CC regions. This will include further hardware modification for the imaging system and interpolation algorithm implementation for the angular spacing between adjacent radial B-scans. Lastly, for potential future clinical translation, the eye movement issue during the complete 360° ICA acquisition might be solved by the faster scanning technique.

In summary, our prototype was demonstrated to be able to visualize the ICA details. Both circumferential and radial images can provide researchers with the spatial representation of the TM/SC/CCs. A variety of image post processing have been implemented for better visualization of the angle details.

Chapter 5: Modeling Meibum Secretion: Alternatives for Obstructive Meibomian Gland Dysfunction (MGD)

Introduction

The first part of my dissertation is related to the use of femtosecond lasers for the treatment of glaucoma and the development of OCT imaging for FLT surgery. The second part of the thesis, covered in the remaining chapters, shifts the focus to the potential applications of lasers for treating meibomian gland dysfunction. Before exploring potential techniques for addressing this condition, we aim to discover novel alternative mechanisms underlying obstructive meibomian gland dysfunction through finite element modeling.

Materials and Methods

Defining The Geometry of The Meibomian Gland Terminal Duct:

Meibum outflow through the gland's orifice occurs via a passive secretory mechanism driven by mechanical forces exerted by the orbicularis muscles on the central duct of the meibomian gland that pushes meibum through the terminal excretory duct and orifice of the gland [166]. The terminal duct was modeled in COMSOL, as a cylinder characterized by a radius R and a length L (Fig. 5.1). Based on a recent report by Cui et al. [167], who measured the diameter and length of the excretory duct using optical coherence tomography and histology, the average maximal inner diameter of the terminal duct measured approximately 100 μm with a length between 890 and 1370 μm. We therefore selected a radius of R = 50

μm and a length of L = 1000 μm as the baseline conditions for modeling the impact of eyelid pressure, and meibum quality on the meibum flow rates, as detailed in Section "*Pressure, Geometry, And Temperature Dependent Studies*".

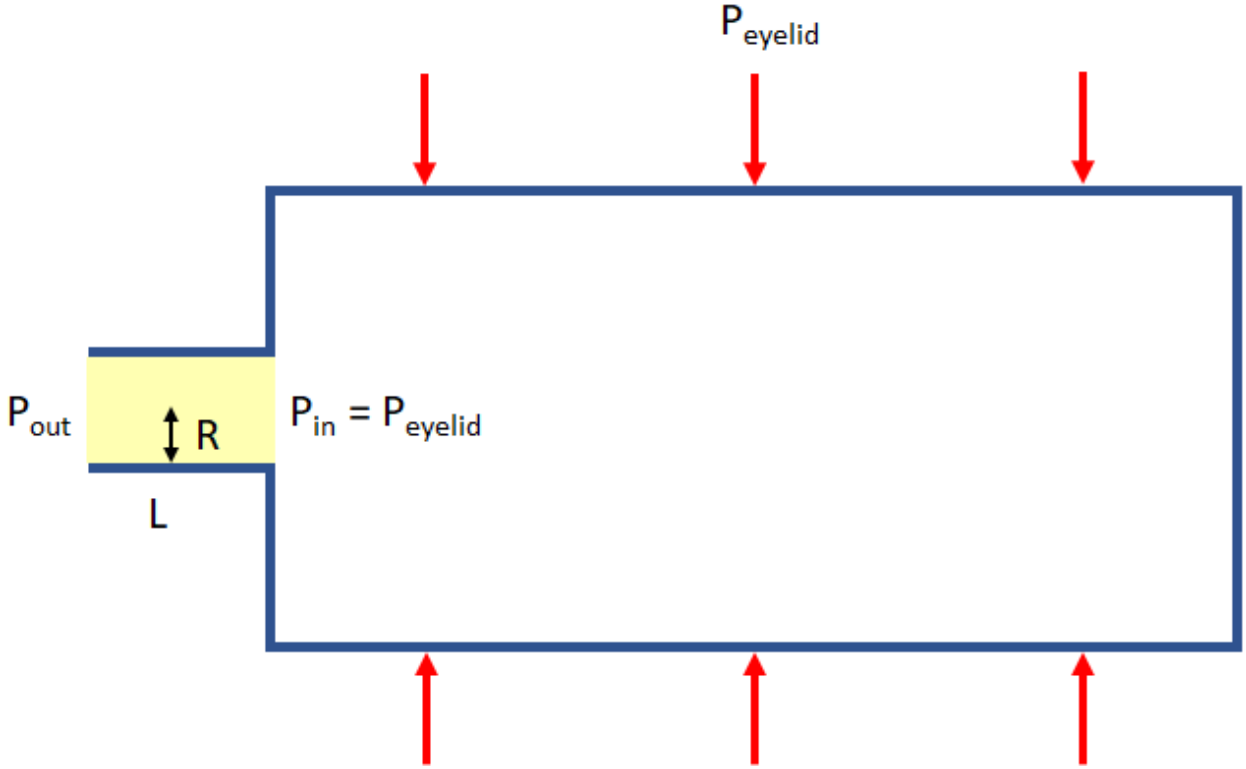

Figure 5.1: Meibomian gland's terminal duct modeling in COMSOL. Meibum secretion is modeled by assuming that the orbicularis muscle overlying the meibomian glands, but not the terminal excretory duct and orifice, exerts an eyelid pressure (P_{eyelid}) on the meibomian gland duct that is translate to the inlet pressure (P_{in}) of the terminal excretory duct represented as a simplified cylindrical model of radius (R) and a length (L). The pressure at the gland orifice is assumed to be the atmospheric pressure (P_{out}). The pressure difference between the two drives the meibum through the terminal duct (depicted as the yellow region). Dimension not scaled.

Defining The Pressures for Driving the Meibum Flow:

To model meibum secretion, we presumed that the external force exerted by the orbicularis muscle on the eye (P_{eyelid}) led to a compensatory and equal increase in the internal pressure of the central duct that could then be applied as the inlet pressure (P_{in}) exerted on meibum at the entrance to terminal duct as shown in Fig. 5.1. Meibum secretion was then presumed to be driven by the pressure drop between the inlet pressure (P_{in}) at the

start of the terminal duct and the outside or atmospheric pressure (P_{out}) at the orifice. The eyelid pressure (P_{eyelid}) was assumed to be equal to the pressure exerted by the eyelid on the eye surface or the change in intraocular pressure (IOP) during an eyelid blink. Typical reported values are presented in Table 5.1.

Table 5.1: Representative values of eyelid pressures utilized in this study.

Pressure measured	References	pressure change in mmHg	corresponding kPa	eyelid manoeuvres	Method
Changes in IOP	Coleman etc, 1969 [183]	90	12	eyelid squeezing	strain gauge
		10	1.3	turning eyes to side	
		10	1.3	blinking	
	Korb etc, 2008 [184]	35	4.7	eyelid squeezing	custom diagnostic instrument
	van den Bosch etc, 2022 [185]	59.1±9.6	7.9±1.3	eyelid rubbing	implanted telemetric IOP sensors in open-angle glaucoma patients
		42.2±5.8	5.6±0.8	eyelid squeezing	
		3.8±0.6	0.5±0.1	eyelid closure	
		11.6±2.4	1.5±0.3	voluntory blink	
		0	0	involuntory blink	
Corneal surface measure	Miller etc, 1967 [186]	10.3±2.3	1.4±0.3	deliberate blink	scleral lens balloon sensor
		7.6±3.5	1.0±0.5	sound blink	
		7.5±2.3	1.0±0.3	touch blink	
		2.8±2.2	0.4±0.3	light blink	
		3.2±1.2	0.4±0.2	static eyelid closure	
	Sakai etc, 2012 [187]	16.95±6.08	2.3±0.8	static eye closed, upper lid	blepharon-tensiometer using tactile pressure sensor
		16.11±7.27	2.1±1.0	static eye closed, lower lid	
	Shaw etc, 2010 [188]	8.0±3.4	1.1±0.5	statid eyelid pressure	piezoresistive pressure sensors at upper lids in young adult subjects
	Wang etc, 2022 [189]	3.9±1.2	0.5±0.2	eyelid closed	custom built membrane pressure sensor

Deriving Viscosity Properties from Human Meibum Rheological Data:

The rheological data of human meibum, specifically shear viscosity versus shear rate reported by Rosenfeld et al. [168], were extracted using the GRABIT software [169] in MATLAB 2021b (Mathworks, Inc., Natick, MA). To calibrate the x- and y-axes within the software interface, a power index, denoted as n, was entered to establish the logarithmic scale for data points corresponding to 10^n values. The extracted data points were subsequently converted to a linear scale using the equation linear_data = 10log data. These linearized data points were then fitted to a Bingham-Papanastasiou (BP) model, using the formulae:

$$\eta_a = \eta_p + \frac{\tau_y}{\dot{\gamma}}\left(1 - e^{-m_p \dot{\gamma}}\right) \quad (5.1)$$

where τ_y represents the minimum yield stress, η_p denotes plastic viscosity, m_p is a scale factor, and η_a is the apparent viscosity defined as the shear stress $\boldsymbol{\tau}$ applied to a fluid divided by the shear rate $\dot{\gamma}$ [170]. Further details regarding these parameters, along with a brief introduction of the BP model, can be found in Appendix 5.1.

Setting Other Model Parameters:

The density of meibum changes little with temperature and is assumed to be 0.9 g/cm^3 [171]. The governing equations in COMSOL are the Navier-Stokes equations, considering no-slip boundary conditions. The element size chosen for the mesh was set to 'Normal' in the COMSOL software, resulting in a mesh consisting of approximately 250,000 elements. The flow is assumed to be laminar [172], and in this study, it is modeled as a single-phase, incompressible fluid.

Pressure, Geometry, And Temperature Dependent Studies:

The inlet pressure influences meibum flow, and therefore, a series of eyelid pressures as discussed in Section "*Defining The Pressures For Driving The Meibum Flow*" and presented in Table 5.1 were used to study the pressure-dependent meibum flow behaviors. To evaluate the impact of geometric factors on meibum expression, a range of radiuses (R = 12.5, 25, 37.5, 50 μm) was investigated while keeping the length fixed at L = 1000 μm. While we did not model changes in excretory duct length, it should be noted that the meibum flow rate inversely correlates with length of the duct, as supported by the analytical derivation

presented in Appendix 5.2. Lastly, parametric sweep studies were conducted for viscosities at four different normal meibum melting temperatures (Table 5.2), with the model's geometry assumed to be fixed at R = 50 μm and L = 1000 μm.

Quantifying The Meibum Secretion:

The volumetric flow rate, Q, was used as a measure of the volume of fluid passing through a specific area per unit of time. It was calculated using the equation:

$$Q = S_c \cdot \bar{u} \quad (5.2)$$

where Sc represents the cross-sectional area of the meibum flow through the terminal duct and orifice ($S_c = \pi R^2$), and $\bar{u}$ denotes the average velocity obtained from COMSOL simulations. Flow rates were computed and compared under different pressure conditions, geometries, and viscosities over the range of meibum melting temperatures.

Results

Meibum Viscosity Parameters for a Non-Newtonian Model:

The resulting fitted rheology data were presented in logarithmic scale as depicted in Fig. 5.2. In general, it was observed that the data at lower temperatures exhibited a superior fit to the BP model compared to the data at higher temperatures. The fitting parameters obtained from the analysis, namely η_p, τ_y, and m_p, are presented in Table 5.2. With the increase in temperature from 25 to 40 °C, meibum undergoes melting, resulting in a significant decrease in both the minimum yield stress and plastic viscosity. Specifically, solid

meibum at 25 °C exhibits higher minimum yield stress of 95.53 N/m^2, and a larger plastic viscosity of 74.95 Pa·s, while more fluid meibum at a melting temperature of 40 °C exhibits dramatically lower minimum yield stress of 2.06 N/m^2 and plastic viscosity of 1.01 Pa·s. The material parameter m_p could not be accurately fitted using the data at temperatures of 35 and 40 °C. However, at 25 °C, the value of m_p was relatively large, indicating a more rigid behavior compared to that at 30 °C.

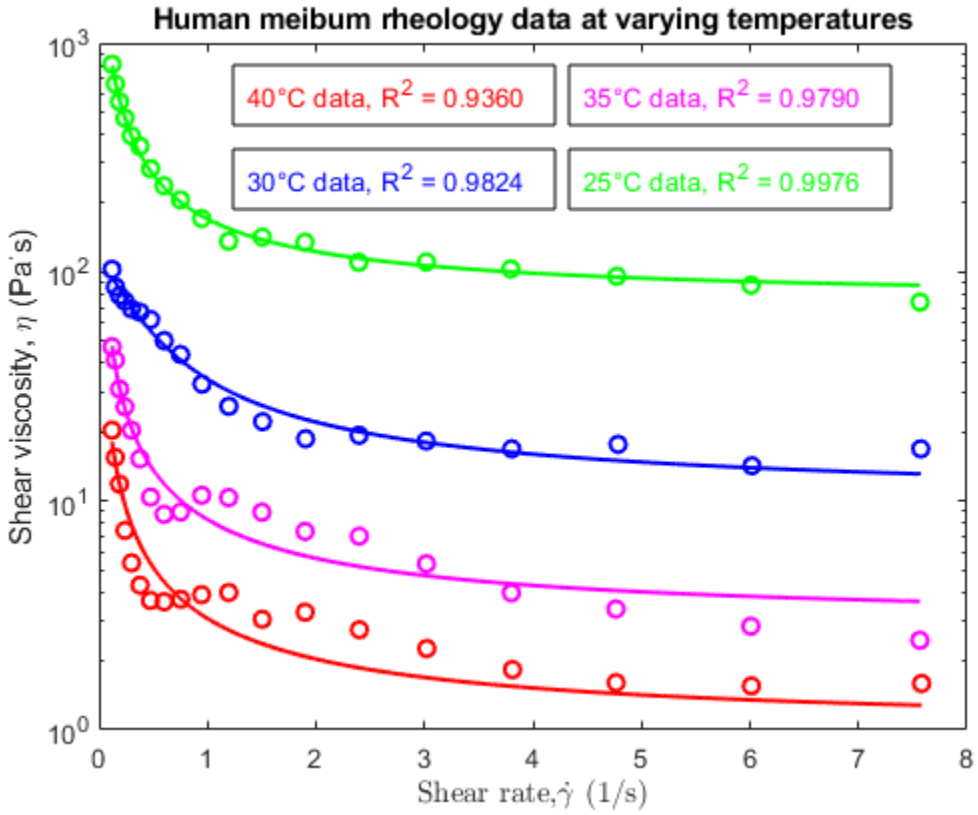

Figure 5.2: The viscosity of human meibum was extracted from existing literature and fitted as a function of shear rate at different temperatures. The coefficient of determination R^2 (not duct radius) was used to evaluate the goodness of the fitting, with a value of 1 indicating an ideal fit between the model and the respective data.

Table 5.2: Extracted parameters for characterizing the Bingham-Papanastasiou non-Newtonian fluidic meibum.

temperature T (°C)	minimum yield stress τ_y (N/m^2)	plastic viscosity η_p (Pa·s)	scale factor m_p (s)
25	95.53	74.95	19.81
30	24.40	9.90	4.55
35	5.36	2.94	62.70†
40	2.06	1.01	190.00†

†The values of the m_p parameter obtained at 35 °C and 40 °C fell within the 95% confidence bounds of (-1962, 2086) and (-Inf, Inf), respectively.

Pressure Dependency:

When the terminal duct radius was held at 50 μm, there was a strong correlation between meibum flow rate and eyelid pressure that increased with increasing temperature as shown in Fig. 5.3. The degree of linearity correlated with the meibum temperature and quality, with more fluid meibum (C and D) showing a slightly higher linear correlation compared to more viscous meibum (A and B). This difference was due to the fact that meibum at lower temperature with higher minimal yield stress and plastic viscosity show practically no meibum flow at the eyelid pressures below 2 kPa.

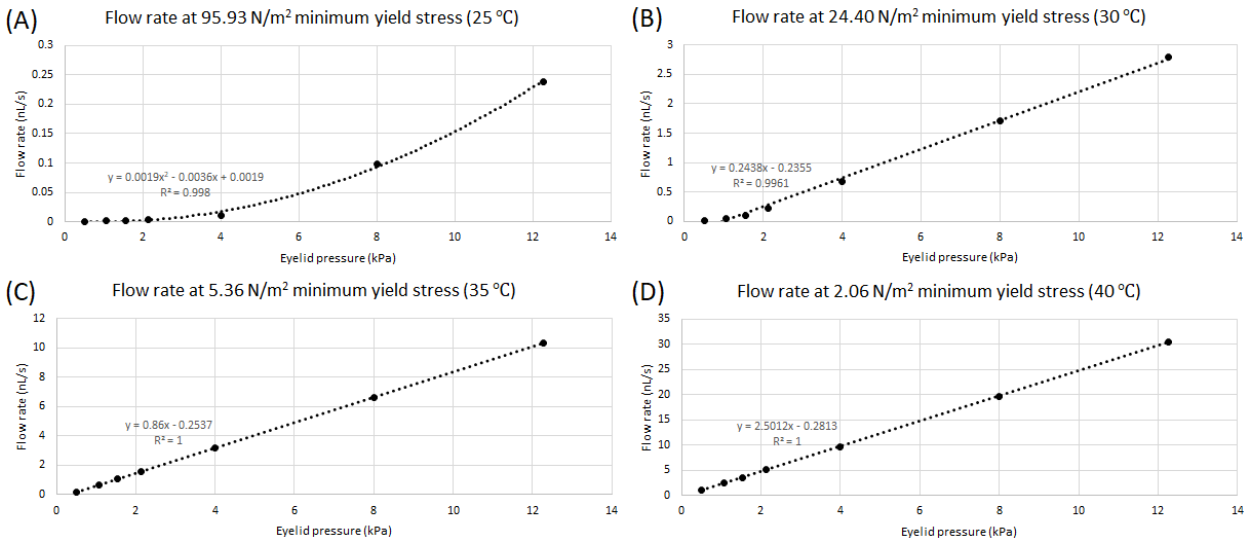

Figure 5.3: Impact of eyelid pressure on meibum flow rate from a meibomian gland orifice at different minimum yield stress or plastic viscosity of meibum obtained at different temperatures along the meibum melting curve, (A) 25 ℃, (B) 30 ℃, (C) 35 ℃, and (D) 40 ℃. A strong linear correlation exists between the meibum flow rate and the eyelid pressure except in case A. It should be noted that there is no meibum flow at low eyelid pressures (<2 kPa) for high minimum yield stress and plastic viscosity (A and B). Modeling geometry is fixed: R = 50 μm, L = 1000 μm.

Previous reports of meibum delivery following eyelid blinking as reported by Chew, et al. [171] and Nagymihalyi et al. [173] using a meibometer to measure the casual level of lipid on the eyelid margin, suggest that an average blink delivers from 0.17 to 0.53 mg of meibum per gland to the eyelid margin. While these levels seem to vary widely between individuals, the estimated average meibum flow rate might vary from 0.55 to 1.7nL/s during a normal blink. Based on modeling and assuming a normal eyelid temperature of 35 °C, this level of meibum flow would be achieved by eyelid pressures varying from 1.1 to 2.1 kPa (Fig. 5.5).

A time-dependent velocity map video illustrating meibum flow in the terminal duct with a radius of 50 μm that would be induced during eyelid blinking was also generated as shown in the supplementary materials (Video S5.1). For the video, a typical blink duration of 1/3 seconds (ΔT) and a blink interval (T) of 5 seconds [174], with inlet pressure changed as $P_{in} = \begin{cases} P_r & 0 \le t < T - \Delta T \\ P_b & T - \Delta T \le t < T' \end{cases}$ where eyelid resting pressure P_r (0.4 kPa) and eyelid blink pressure Pb (2.1 kPa) at a temperature of 35 °C.

Viscosity Effects:

Viscosity data of meibum obtained at different melting temperatures (refer to Table 5.2) were used to examine the influence on meibum expression within a BP model. As the

meibum transitioned from fluid to solid, there was an exponential decrease in meibum flow, caused by the increasing minimum yield stress and plastic viscosity (Fig. 5.4). To visualize both effects of viscosity and eyelid pressure, Fig. 5.5 presents a compilation of cross-sectional distributions of the velocities and flow rates of meibum secretion from a meibomian gland orifice at different viscosities and eyelid pressures.

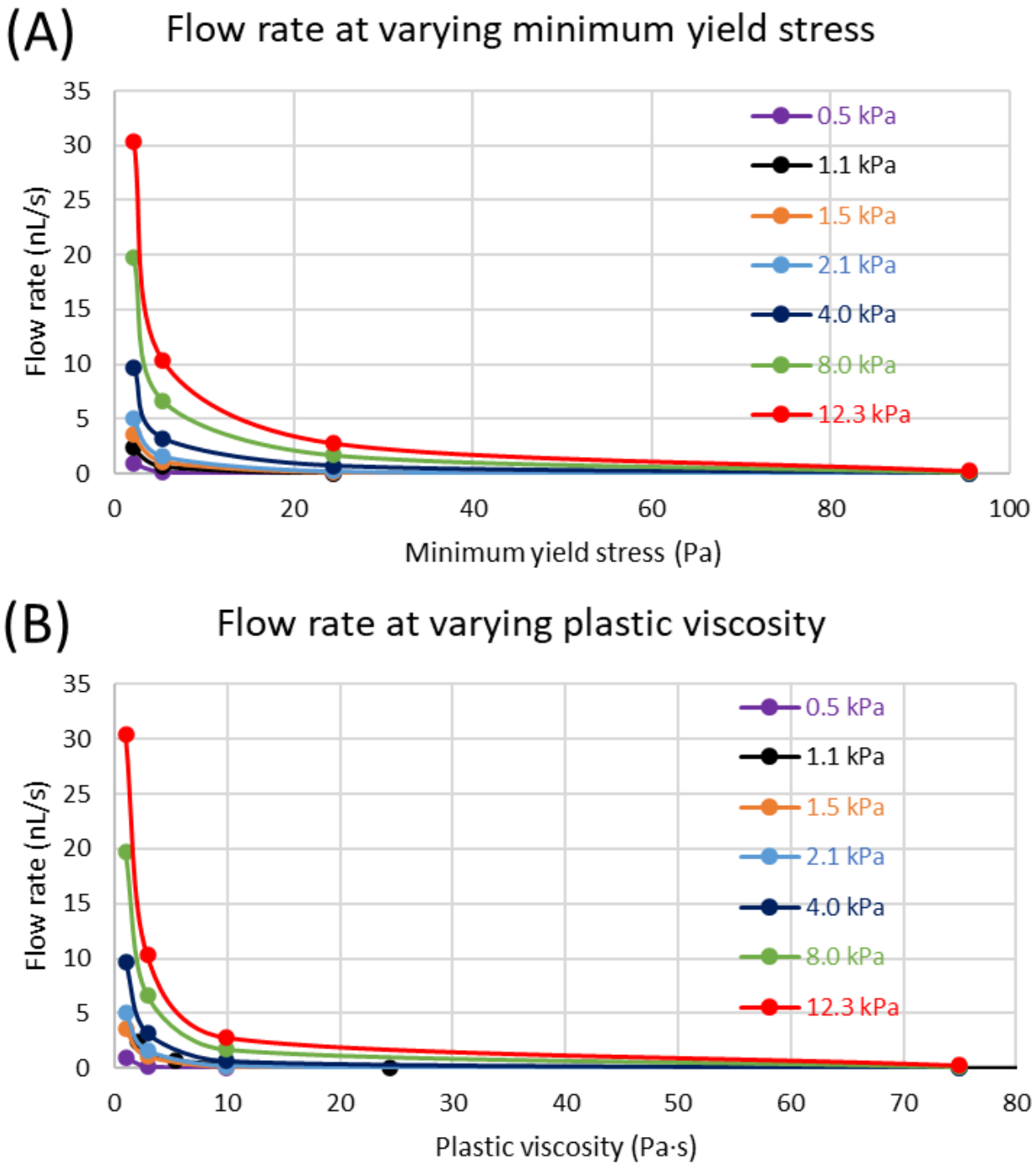

Figure 5.4: Effects of changes in meibum viscosities on meibum flow rate from a meibomian gland orifice. Note that there is an exponential decrease in meibum flow rates with (A) higher minimum yield stress and (B) plastic viscosity. Different curves indicate modeling under different eyelid pressures. R = 50 μm, L = 1000 μm.

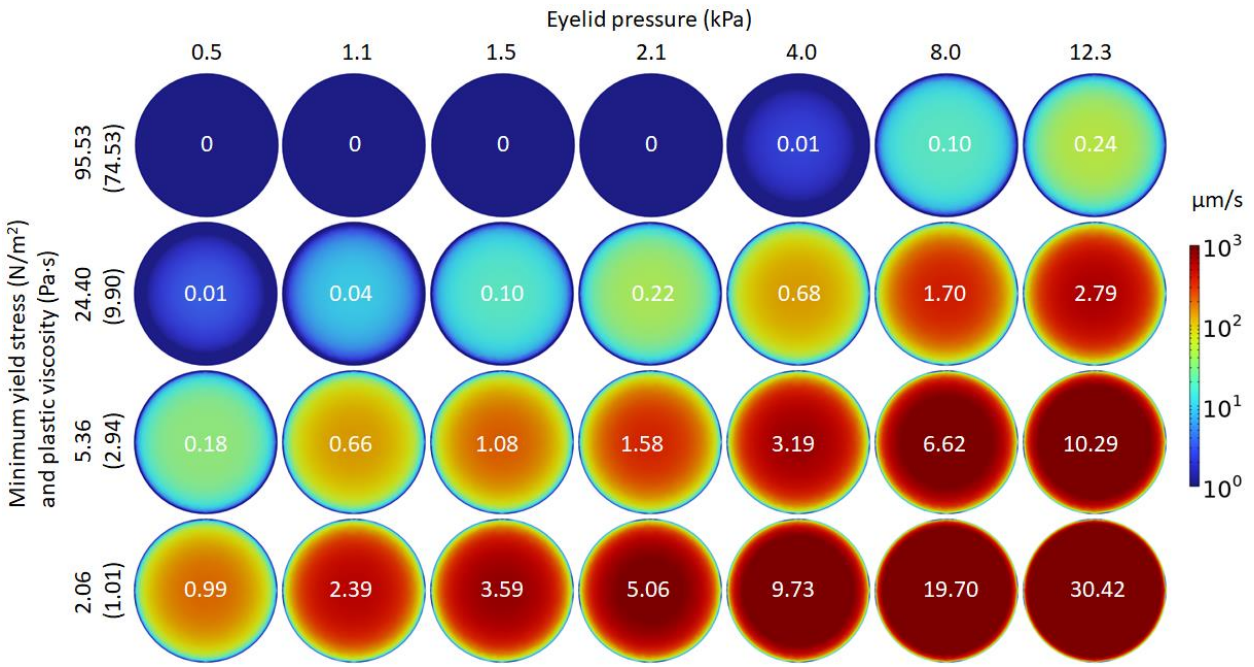

Figure 5.5: Cross-sectional distribution of the velocity maps (μm/s) and flow rates (nL/s) of meibum secretion from a meibomian gland orifice at different meibum viscosities and eyelid pressures, as summarized in the current study. The velocity is color mapped in a log scale between 1 and 1000 μm/s. No-slip boundary conditions result in zero velocities at the edges of the ducts. Corresponding flow rates are shown in the center of each map. The 7 typical eyelid pressures under current study are selected or approximated from Table 5.1, and their mmHg values are converted into kPa values. R = 50 μm and L = 1000 μm.

Geometric Effects:

As shown in Fig. 5.6, there was a significant correlation between meibum flow rate and the fourth power of the duct's radius R^4 at both low (A) and high (B) eyelid blink pressures. A similar relationship was observed in Eq. S14 of Appendix 5.2.

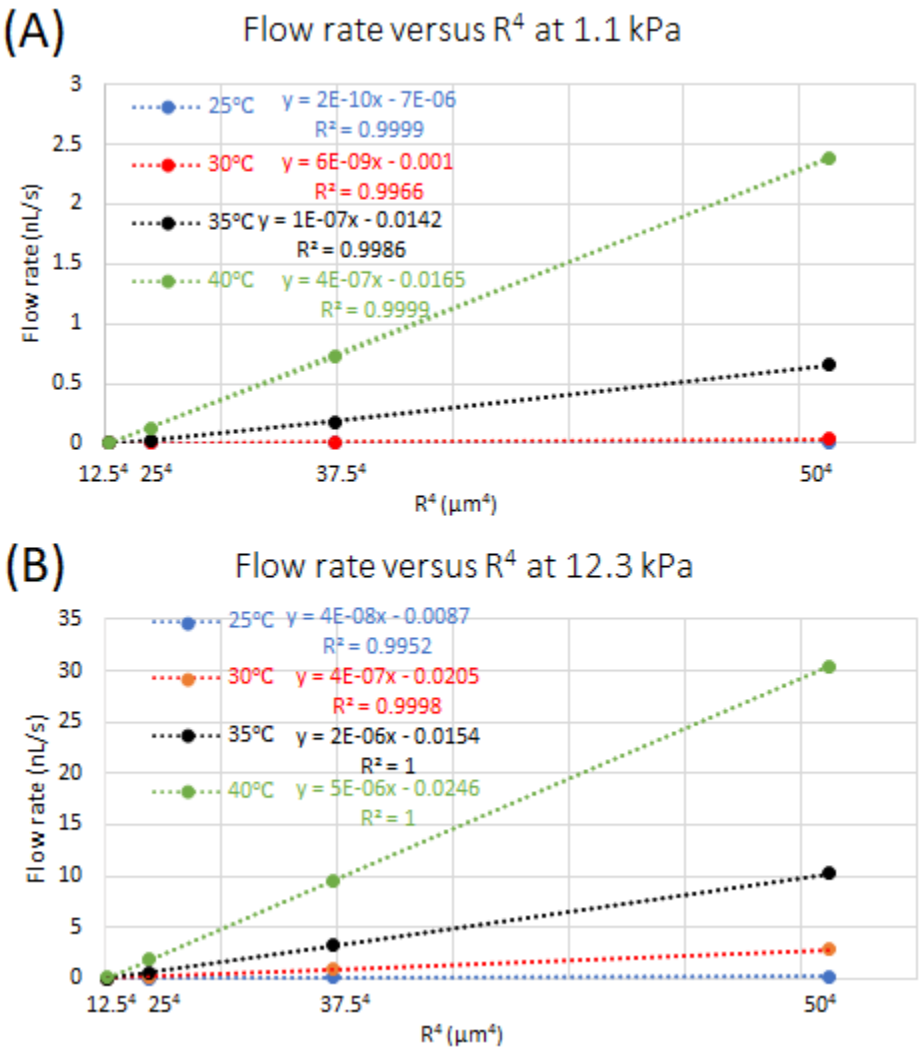

Figure 5.6: Influence of terminal duct size on meibum flow rate from a meibomian gland orifice. The fittings suggest that the meibum flow rate exhibits a linear correlation with the fourth power of the duct radius, both at low eyelid pressure (A), where Pb = 1.1 kPa, and at high eyelid pressure (B), where Pb = 12.3 kPa. This is consistent with Poiseuille's Law. At a temperature of 35 °C in scenario (A), with a radius of 50 µm and an eyelid pressure of 1.1 kPa, a comparable meibum flow rate of 0.6 nL/s is observed when compared to scenario (B), which involves a radius of 25 µm and an eyelid pressure of 12.3 kPa. Note that different colors indicate different temperatures. L = 1000 µm.

Discussion

In this paper we have developed a finite element model for measuring the flow of meibum from the terminal duct of the meibomian gland and analyzed the combined effects of eyelid pressure and duct radius on meibum delivery to the eyelid margin. For this analysis

we have modeled meibum as a non-Newtonian fluid based on rheological data of human meibum as reported by Rosenfeld et al. [168]. Minimum yield stress and plastic viscosity values were estimated based on data from meibum taken at different temperature values covering the melting range of meibum from 25 °C to 40 °C. Based on finite element modeling, meibum flow rates exponentially decreased with increasing minimum yield stress and plastic viscosity. Modeling also revealed that meibum flow rates at the same minimum yield stress and plastic viscosity was linearly related to eyelid pressure and the fourth power of the duct radius. Together, these findings suggest novel alternatives to the classical understanding of obstructive MGD and potentially new mechanisms for meibomian gland atrophy involving changes in meibum melting point, eyelid pressure and ductal radius as discussed below.

Effects of Altered Meibum Melting Point:

As measured by Butovich et al. [175], meibum obtained from normal subjects has a wide melting range from 10 °C to 40 °C, with three transition points at 12 °C, 21 °C and 32 °C. On the other hand, meibum from dry eye subjects have a slightly higher range with transition points of 22 °C and 33 °C as measured by Butovich et al. and up to 35 °C as measured by McCulley and Shine [176]. These changes in meibum melting point are also consistent with the decreased presence of wax esters that have been identified in patients with dry eye disease [177, 178], and the known lower melting point of wax esters [179, 180]. Furthermore, meibum from dry eye patients also contains variable amounts of proteins which may also affect the meibum melting temperature [175, 181, 182].

As noted in our study, shifts in the melting temperature of meibum has exponential effects on both the minimum yield stress and plastic viscosity that increase more than three to four-fold with a temperature shift of only 5 °C (35 °C to 30 °C), resulting in a change from 5 to 24 N/m^2 and 3 to 10 Pa·s, respectively. These effects of temperature on meibum flow rate predict to large extent the findings of Nagymihalyi et al. [173], which identified a marked decrease in the deposition of meibum after 10 blinks following a 7 °C cooling of the surface of the eyelids. While rheology of meibum from MGD patients with altered meibum quality have not been measured, the measured shift in melting temperature of meibum noted for MGD patients would predict similar increase in the minimum yield stress and plastic viscosity and an exponential decrease in meibum flow that could be reduced by as much as 90% depending on the eyelid pressure.

Effects of Eyelid Pressure on Meibum Flow Rates:

A range of eyelid pressures on the eye have been reported using a wide range of techniques from measuring the intraocular pressure during blinking [183-185], to more static measurements using scleral or contact lenses with pressure sensors [186-189] as detailed in Table 5.1. For the most part, static eyelid pressures with eyelids either open or closed produce very low pressures on the eye that are generally below 10 mmHg (1.3 kPa), while eyelid blinking produces higher values. Reports measuring changes in intraocular pressure during eyelid blinking show much higher changes in IOP that can achieve levels from 40 mmHg to 90 mmHg during squeezing of the eyelids [183, 185]. As noted earlier however, translating changes in IOP to the pressure exerted on the eye by the eyelid is

difficult. Likewise, measurement of eyelid pressure during blinking using contact lens pressure sensors is complicated by the fact that the sensor needs to be inserted between the eyelid and the eye, thus changing the normal application of force. Furthermore, the force applied to the eye by the eyelid is localized to the lid wiper or distal region of eyelid near to eyelid margin, which may not be adequately measured by some sensors [188]. Finally, the relationship between the pressure the eyelid exerts on the eye and the pressure exerted on the meibomian gland duct is not known. All these concerns make it difficult to extrapolate eyelid pressure data to pressure changes in the duct of the meibomian gland, other than to say that blink pressure is most likely higher than resting pressure with eyes open or closed.

Nevertheless, modeling demonstrates a linear increase in meibum flow rate with higher eyelid pressures. This observation is consistent with clinical findings and aligns with intuitive expectations. Interestingly, eyelid pressure on the eye has been shown to decrease with age, averaging 23.2 mmHg in individuals that are over twenty, decreasing to 13.6 mmHg for individuals over sixty, or a reduction of 2-3 mm Hg for every 10 years [190]. This decrease in eyelid pressure would translate into a 40% decrease in meibum flow rate for individuals over sixty and a 70% reduction for individuals over 90 years of age. While the volume of meibum delivered to the eyelid margin with each blink likely exceeds the volume necessary to replenish lipid onto the eyelid surface by some 40 fold [171], this age-related decrease in eyelid pressure combined with changes in melting temperature and other structural changes in the duct may help explain the significant relationship between age and MGD. Certainly, more in-depth modeling of this mechanism is needed in the future.

The Effect of Ductal Morphology on Meibum Flow Rates:

When other parameters are held constant, we observe a linear relationship between the flow rate and the fourth power of the duct radius. Both the pressure and geometric studies indicated that the flow of meibum followed Poiseuille's law [172], which is typically derived for a Newtonian fluid. However, we speculate that the non-Newtonian behaviors did not overwhelmingly dominate the entire flow pattern (please refer to Appendix 5.2 for further information). Interestingly, at temperatures of 35 °C, comparable meibum flow rates were found between (A) a radius of 50 μm and an eyelid pressure of 1.1 kPa, and (B) a radius of 25 μm and an eyelid pressure of 12.3 kPa (Fig. 5.6).

While hyperkeratinization and plugging of the meibomian gland duct is cited as the most common cause of obstructive MGD, a recent detailed immunohistochemical study of the human meibomian gland by Reneker et al., found evidence of ductal epithelial hyperproliferation but not hyperkeratinization [191]. It is interesting to note that our modeling data also predicts significant effects of ductal epithelial thickening on meibum flow rates. While little is known regarding the thickness of the ductal epithelium that lines the excretory duct, histology images presented by Cui et al. report an outer ductal diameter of 172 μm with an inner diameter of 100 μm, giving a ductal epithelial thickness of approximately 35 μm [167]. Since the excretory duct is embedded in a dense collagenous tarsal plate, it might be assumed that the outer diameter of the excretory duct is fixed, and any hyperproliferation leading to ductal epithelial thickening would lead to a reduction in the inner diameter of the duct. Based on our modeling, an increase in epithelial thickness from 35 to 40 μm, or a 5 μm increase, would lead to a 35% decrease in meibum flow rate in

a 100 μm diameter duct, and a 62%-86% decrease in flow rate in a 50 μm diameter duct depending on the eyelid force.

Limitations

A major limitation of this study is the lack of available data for meibum rheology from both normal and MGD subjects. For normal meibum, rheology data is only available for only 4 discrete melting temperatures from 25 °C to 40 °C [168], while no data is available from meibum expressed from MGD patients. While we have assumed that changes in meibum melting temperature from MGD patients would translate into changes in meibum flow rates indicative of the increased minimum yield stress and plastic viscosity observed at lower temperature in normal meibum, this may not accurately predict the changes that occur. Additionally, it is crucial to gather more clinical rheology data encompassing the clinical range of altered meibum quality from viscous to toothpaste-like in future studies.

A second limitation of this study is that little is known regarding the actual mechanisms of meibum secretion, and the effect of forces that are exerted on the inside of the duct to push meibum out of the gland. While there are many reports concerning the force the eyelid exerts on the eye, whether these forces are directly related to the compressive forces exerted on the gland are not known. Furthermore, how these forces translate into the pressure exerted on the excretory portion of the duct is not known and whether these forces can produce other effects on the gland remains to be studied. In this report we have only modeled the terminal, 1 mm distal end of the duct, and how this pressure affects the more central duct remains unclear. It is likely that as meibum flow is decreased, internal ductal pressure may have effects on the lateral wall of the common duct causing increased mechanical strain. While 'acinar disuse atrophy' is an often-cited mechanism for obstructive

MGD [192], a more plausible alternative is that reduced meibum flow regardless of cause leads to increased mechanical strain and stretching of the ductal and acinar cells that cause downstream effects on cell differentiation. To more clearly understand these potential effects, a more complex modeling of the entire meibomian gland is needed, which requires better understanding of the tissue compliance of the ductal epithelium and surrounding extracellular matrix.

Chapter 6: Selective Photothermal Ablation for MGD

Introduction

After proposing alternative mechanisms for obstructive meibomian gland dysfunction (MGD), we then introduced a technique called selective photothermal ablation (SPA) for its treatment. As the term 'selective' suggests, SPA can heat or ablate the desired meibum within the meibomian glands selectively or preferentially while preserving the overlying conjunctival epithelial tissues. In this chapter, we presented preliminary ex-vivo results in mice.

Materials and Methods

Selective Photothermal Ablation (SPA) Laser System:

The surgical laser system (Cutera Inc.) operates at 1726 nm and offers tunable current (power) capacity, variable pulse duration, and laser duty cycles. Laser pulses are delivered through a custom-designed handpiece that passes through a glass slide before penetrating the carefully flattened tissue, which is sandwiched between that glass slide and a block immersed in iced water. This setup serves as a contact cooling system, essential for preventing hyperthermal tissue damage (Fig. 6.1).

The average power of the laser at each ampere of current was measured in air using a power meter (Newport model 1918-C, Irvine, CA) for laser calibration.

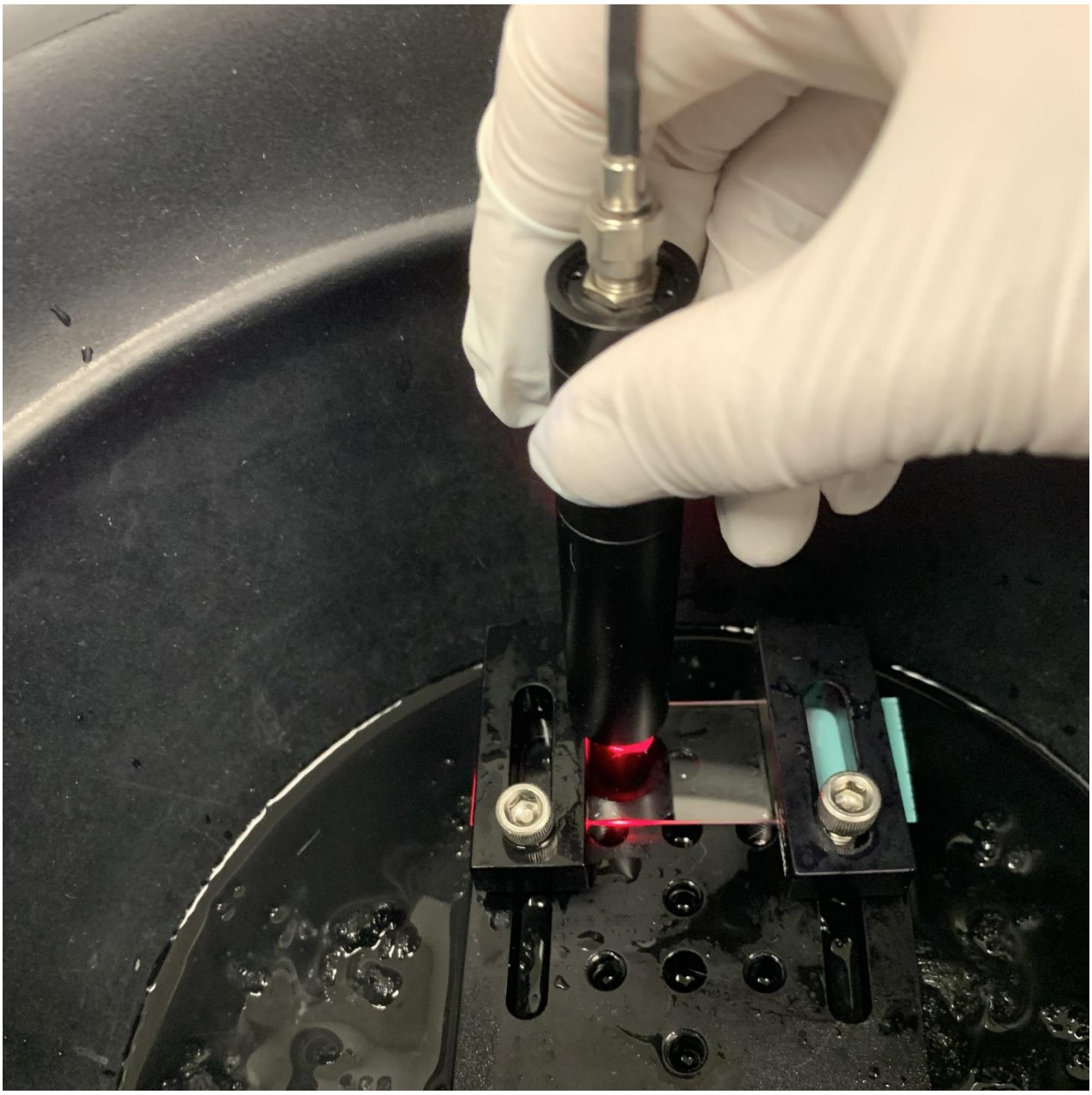

Figure 6.1: Experimental setup. The tissue was carefully flattened and sandwiched between a glass slide and a block immersed in iced water, forming a simplified contact cooling system. The skin side of the eyelid was positioned downwards, while the conjunctiva side faced upwards, allowing the laser beam from the handpiece to pass through the glass slide before penetrating the meibomian glands, which are embedded beneath the conjunctiva. Red light was used to guide the 1726 nm surgical laser.

Mice Eyelids Preparation for SPA Treatment:

Five male mice were sacrificed by cervical neck dislocation after Ketaimin anesthesia. The upper eyelid of each mouse was peeled off each time by surgical scissors under a dissecting microscope. The tissue sample is immediately immersed into a peri dish containing cell culture DMEM medium at 4°C. The experimental procedures adhered to the principles outlined in the Declaration of Helsinki.

The eyelid tissue is oriented so that the conjunctiva of the eyelid faces upwards, exposed to the laser beam through a glass slide. The tissue was precooled for 1 minute before the treatment. A coaxial visible red light is used to guide the 1726 nm surgical laser toward the desired meibomian glands located beneath the conjunctiva, making them visible to the naked eye. Based on the theory of selective photothermolysis [43], the duration of the beam was set to 120 ms. The laser beam diameter is 500 μm. Each eyelid received one laser zap at the center of the tissue. A meibography image was taken before and after the SPA laser treatment. The tissue was fixed in 2% PFA right after the meibography imaging for 24 hours.

Tissue Damage Assessment by Histology and Immunohistochemistry Imaging:

The fixed samples were subsequently placed in an embedding medium (Tissue-Tek O.C.T. Compound, Sakura Finetek USA, Inc., Torrance, CA) and frozen in liquid nitrogen for subsequent cryosection. The tissue slices were stained using either H&E or immunohistochemistry (DAPI, Phalloidin and LipidTox) to obtain the histological results for

the laser damage evaluation. Images were taken either using a standard light microscope (OLYMPUS BX60) or a fluorescence microscope (Leica CTR 6500).

Results

Laser calibration:

Figure 6.2 shows the average power of the laser measured in air as a function of current in amperes, demonstrating high linearity when the current exceeds 8 amperes.

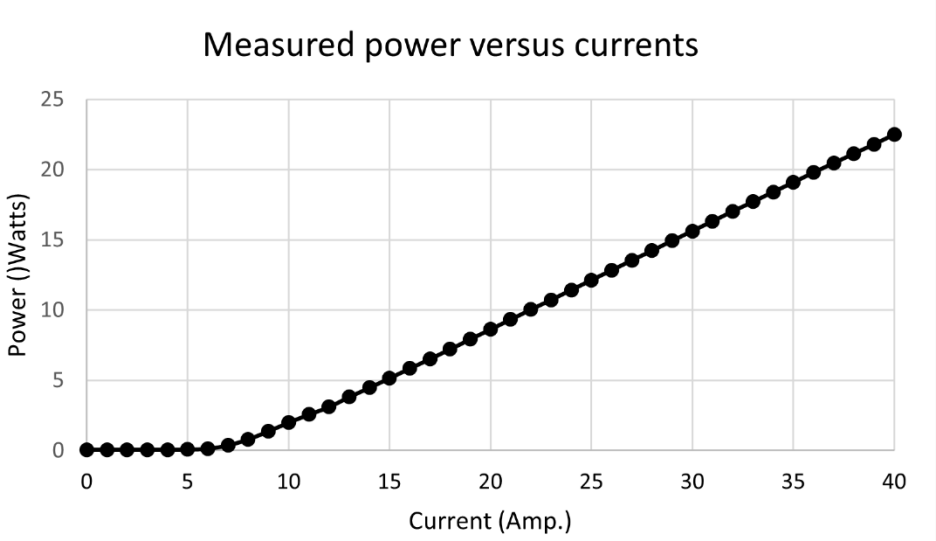

Figure 6.2: Laser Calibration. The SPA laser system can be finely tuned for current control. A power meter was used to measure the corresponding average power of the beam radiation at current intervals of 1 ampere, ranging from 0 to 40 amperes.

Tissue Damage Assessment After SPA Treatment:

Representative meibography images of eyelid tissue were captured before and after SPA treatment, as depicted in Fig. 6.3. During the SPA treatment, the meibomian glands in the treated area were selectively targeted and removed, while the overlying conjunctiva remained intact. The laser parameters used for SPA treatment included a 500 μm beam diameter, 14 amperes (corresponding to 5 Watts), and a 120 ms pulse duration.

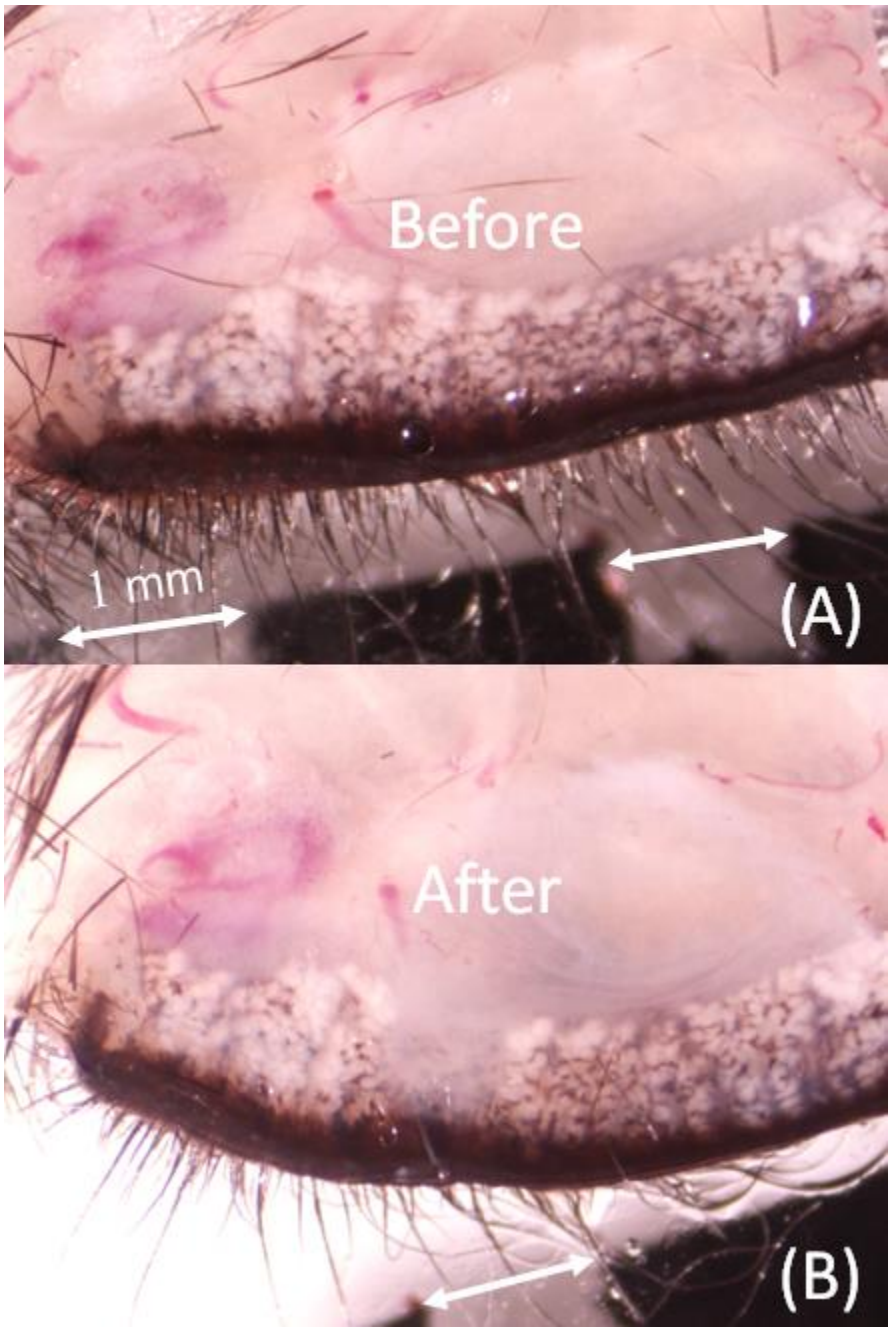

Figure 6.3: Meibography images of eyelid tissue taken (A) before and (B) after SPA treatment, illustrating the selective removal of meibomian glands in the treated area while leaving the overlying conjunctiva tissue intact. Laser parameters for SPA treatment include a 500 μm beam diameter, 5 Watts, and a 120 ms pulse duration.

Figures 6.4 and 6.5 display meibomian gland shrinkage in the H&E image and meibum melting in the fluorescent image, respectively. Both images show no signs of damage to the overlying conjunctiva tissue.

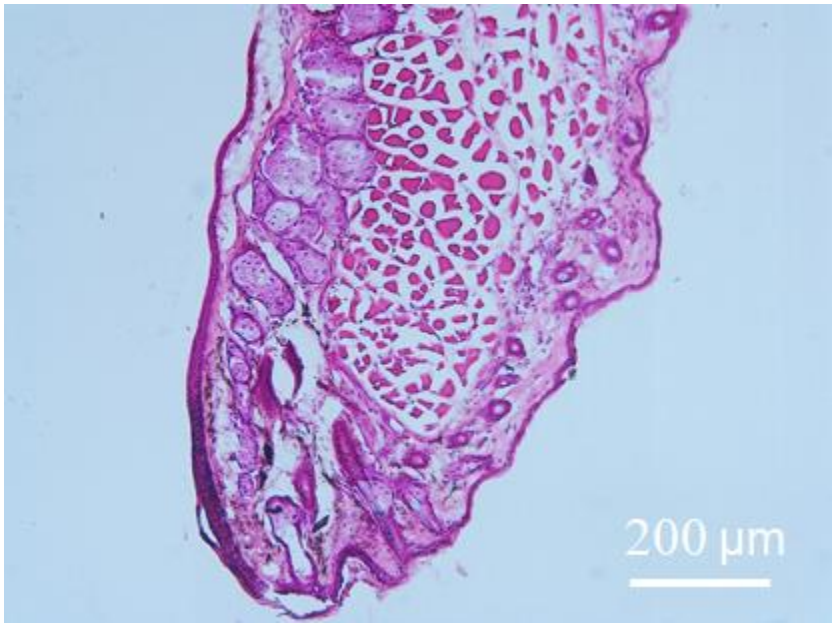

Figure 6.4: H&E histological image indicating the shrinkage of meibomian glands after SPA treatment. The same laser parameters and eyelid sample used as in Fig. 6.3.

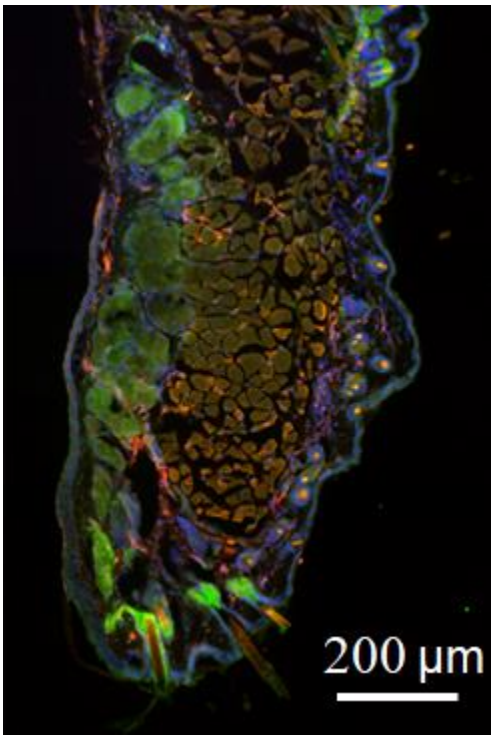

Figure 5: Fluorescent image showing meibum melting after SPA treatment. Blue: DAPI stains the nuclei. Green: LipidTox stains the lipid. Red: Phalloidin stains the muscle. The same laser parameters and eyelid sample were used as in Figs. 6.3 & 6.4.

Discussion

In this study, we propose a novel SPA treatment for MGD-related dry eye syndromes, conducting an ex vivo feasibility study using a narrow laser centered at 1726 nm. Our results indicate that SPA can selectively target meibomian glands and melt meibum while leaving the overlying tissues intact. SPA holds promise as a technique for MGD treatment.

Current laser treatments with wide bandwidths can potentially cause thermal damage to surrounding tissues, as they may induce equivalent or comparable wavelength-integral bulk effects of thermodynamics or photobiomodulation across a broader radiation spectrum. Therefore, designing a narrow bandwidth laser centered at the wavelength of the local absorption peak of the target is desirable to ensure preferential or selective absorption

by the target rather than adjacent tissues. Scopelliti et al [193] reports a narrow local absorption peak of sebum lipid, higher than that of water, at 1726 nm, making it a preferential absorption site for heat in sebum. The recent success of the 1726 nm laser for acne treatment suggests its potential use for DED due to MGD. Our SPA treatment, as demonstrated in this study, exhibits selective treatment in meibography images. The treatment selectivity of SPA is further confirmed in H&E and fluorescent imaging, revealing meibomian gland shrinkage and meibum melting beneath the untouched overlying conjunctiva tissue.

Cooling is essential before, during, and after SPA treatment because, despite selective heating of the meibum, the laser can still generate significant thermal effects on other tissues. Cooling helps to mitigate hyperthermal effects and safety concerns in healthy tissues, bringing them within a safe and acceptable range.

Chapter 7: Conclusions and Future Work

Conclusions

Pulse Energy Optimization for FLT:

In conclusion, this study successfully demonstrated the capability of our FLT system, utilizing a pulse energy of 15 μJ, to effectively photodisrupt the TM tissues. This led to the creation of a full-thickness outflow channel, establishing a vital connection between the anterior chamber and SC. The confirmation of this outcome was achieved through comprehensive analysis of high-resolution OCT images. These findings emphasize the effectiveness of utilizing OCT as a valuable tool for evaluating the efficacy of FLT surgery in the treatment of glaucoma.

Thermal Collateral Damage During FLT – an Ex-vivo Study:

This study shows that tissue heating during FLT is well beneath the threshold for thermal denaturization of collagen and proteins in general. Various imaging modalities (histology, SHG) prove there is no thermal collateral damage to the tissue surrounding the FLT channel.

OCT Dispersion Compensation:

In conclusion, we presented a new numerical dispersion compensation algorithm for an SD-OCT, for imaging the iridocorneal angle of human cadaver eyes. The dispersion

compensation term can be calculated with an automatic iterative procedure that minimizes the k-dependent ridge variance via optimization of energy redistribution of a mirror's spectral interferogram in the spatial-spectral domain using STFT. Lastly, we demonstrate the feasibility of the proposed method for dispersion compensation in an SD-OCT by evaluating both the mirror and angle imaging of human cadaver eyes.

Iridocorneal Angle OCT Imaging:

In this study, we presented a custom-built, high-resolution SD-OCT system to scan the corneoscleral limbus and implemented different image processing for better visualization of the TM/SC/CC areas in human cadaver eyes. Simultaneously radial and circumferential scanning were implemented in the current system. A semiautomatic segmentation of the anterior corneal surface was carried out using a graph search algorithm and iterative method. Based on this segmentation, we further encoded the depth with 'rainbow effect' colors, which can be readily perceived by human eyes. In addition, intensity projections, and en face imaging were performed as supplemental information to the individual B-scan image and 3D reconstruction. To our best knowledge, this is the first time that the aforementioned novel or improved image processing and a 'crossline' scan have been implemented to achieve a better visualization and comprehensive understanding of the angle details. Future full integration of these imaging capabilities into an FLT system would potentially assist the accurate determination of the surgical targets and benefit other glaucoma treatments as well.

Modeling Meibum Secretion – Alternatives for Obstructive Meibomian Gland Dysfunction (MGD):

In summary, this study has successfully developed and applied a finite element analysis to simulate the flow of non-Newtonian meibum within the terminal duct of the meibomian gland. Through systematic investigations, the impact of eyelid pressure, meibum minimum yield stress and plastic viscosity, and distal duct geometry on meibum flow rate has been thoroughly explored. The results reveal a significant exponential decrease in meibum flow with increasing minimum yield stress and plastic viscosity that develop over the range of normal meibum melting temperatures from 25 ^{o}C to 40 ^{o}C. This finding predicts that clinical changes in meibum quality noted in MGD patients can be explained by an increase in the meibum melting temperature causing the appearance of increased meibum viscosity, reduced meibum flow and the requirement for increased application of force to express altered meibum. Our analysis also found that there was a linear relationship between the fourth power of the distal duct radius and the meibum flow rate, indicating that small changes in the thickness of the ductal epithelium may produce significant changes in the flow rate of meibum. Finally, there was a linear relationship between eyelid pressure and meibum flow. Together, changes in these three factors can lead to marked restriction of meibum flow onto the eyelid margin, and, in part, provide an alternative cause for obstructive MGD.

Selective Photothermal Ablation for MGD:

In summary, SPA represents a novel treatment for MGD-related dry eye using a narrowband 1726 nm laser. Further in-vivo investigations are necessary.

Future Work

OCT Image Guided FLT:

We identified the collector channels along Schlemm's canal and the trabecular meshwork using a high-resolution spectral domain OCT imaging system. However, it remains unknown whether performing FLT surgery near the collector channels in the trabecular meshwork results in a greater reduction in intraocular pressure (IOP). Additionally, targeting and cutting through the full depth of the trabecular meshwork while preserving the endothelium of the outer wall of Schlemm's canal can help avoid unnecessary tissue damage. OCT image guided FLT surgery, involving OCT imaging before and during the procedure, has the potential to enhance surgical accuracy and improve IOP reduction.

In Vivo SPA for Obstructive MGD Treatment:

Selective photothermal ablation (SPA) represents a promising approach for the treatment of MGD. Further investigation through in vivo studies is warranted to validate these findings.

References

[1] Luo S, Holland G, Mikula E, Bradford S, Khazaeinezhad R, Jester JV, et al. Dispersion compensation for spectral domain optical coherence tomography by time-frequency analysis and iterative optimization. Optics Continuum. 2022;1:1117-36.

[2] Tham YC, Li X, Wong TY, Quigley HA, Aung T, Cheng CY. Global Prevalence of Glaucoma and Projections of Glaucoma Burden through 2040 A Systematic Review and Meta-Analysis. Ophthalmology. 2014;121:2081-90.

[3] Johnson M. What controls aqueous humour outflow resistance?. Exp Eye Res. 2006;82:545–57.

[4] Goel M, Picciani RG, Lee RK, Bhattacharya SK. Aqueous humor dynamics: a review. Open Ophthalmol J. 2010;4:52-9.

[5] Carreon T, van der Merwe E, Fellman RL, Johnstone M, Bhattacharya SK. Aqueous outflow - A continuum from trabecular meshwork to episcleral veins. Prog Retin Eye Res. 2017;57:108-33.

[6] Tamm ER. The trabecular meshwork outflow pathways: structural and functional aspects. Exp Eye Res. 2009;88:648-55.

[7] Hann CR, Vercnocke AJ, Bentley MD, Jorgensen SM, Fautsch MP. Anatomic changes in Schlemm's canal and collector channels in normal and primary open-angle glaucoma eyes using low and high perfusion pressures. Invest Ophthalmol Vis Sci. 2014;55:5834-41.

[8] Allingham RR. Shields textbook of glaucoma. 7 ed. Philadelphia: Wolters Kluwer; 2021.

[9] Conlon R, Saheb H, Ahmed, II. Glaucoma treatment trends: a review. Can J Ophthalmol. 2017;52:114-24.

[10] Nordstrom BL, Friedman DS, Mozaffari E, Quigley HA, Walker AM. Persistence and adherence with topical glaucoma therapy. Am J Ophthalmol. 2005;140:598-606.

[11] Patel SC, Spaeth GL. Compliance in patients prescribed eyedrops for glaucoma. Ophthalmic Surg. 1995;26:233-6.

[12] Inoue K. Managing adverse effects of glaucoma medications. Clin Ophthalmol. 2014;8:903-13.

[13] Beckers HJ, Schouten JS, Webers CA, van der Valk R, Hendrikse F. Side effects of commonly used glaucoma medications: comparison of tolerability, chance of discontinuation, and patient satisfaction. Graefes Arch Clin Exp Ophthalmol. 2008;246:1485-90.

[14] Nordmann JP, Auzanneau N, Ricard S, Berdeaux G. Vision related quality of life and topical glaucoma treatment side effects. Health Qual Life Outcomes. 2003;1:75.

[15] Waldock A, Snape J, Graham CM. Effects of glaucoma medications on the cardiorespiratory and intraocular pressure status of newly diagnosed glaucoma patients. Br J Ophthalmol. 2000;84:710-3.

[16] Wickham MG, Worthen DM. Argon laser trabeculotomy:long-term follow-up. Ophthalmology. 1979;86:495-503.

[17] Wise JB, Witter SL. Argon laser therapy for open-angle glaucoma. A pilot study. Arch Ophthalmol. 1979;97:319-22.

[18] Melamed S, Pei J, Epstein DL. Short-term effect of argon laser trabeculoplasty in monkeys. Arch Ophthalmol. 1985;103:1546-52.

[19] van der Zypen E, Fankhauser F. Ultrastructural changes of the trabecular meshwork of the monkey (Macaca speciosa) following irradiation with argon laser light. Graefes Arch Clin Exp Ophthalmol. 1984;221:249-61.

[20] Melamed S, Epstein DL. Alterations of aqueous humour outflow following argon laser trabeculoplasty in monkeys. Br J Ophthalmol. 1987;71:776-81.

[21] Stein JD, Challa P. Mechanisms of action and efficacy of argon laser trabeculoplasty and selective laser trabeculoplasty. Curr Opin Ophthalmol. 2007;18:140-5.

[22] Rodrigues MM, Spaeth GL, Donohoo P. Electron microscopy of argon laser therapy in phakic open-angle glaucoma. Ophthalmology. 1982;89:198-210.

[23] Fink AI. Argon-Laser Trabeculoplasty. Arch Ophthalmol-Chic. 1984;102:1746-.
[24] Dueker DK, Norberg M, Johnson DH, Tschumper RC, Feeney-Burns L. Stimulation of cell division by argon and Nd:YAG laser trabeculoplasty in cynomolgus monkeys. Invest Ophthalmol Vis Sci. 1990;31:115-24.
[25] Kimpel MW, Johnson DH. Factors influencing in vivo trabecular cell replication as determined by 3H-thymidine labelling; an autoradiographic study in cats. Curr Eye Res. 1992;11:297–306.
[26] Bylsma SS, Samples JR, Acott TS, Pirouzkar B, Van Buskirk EM. DNA replication in the cat trabecular meshwork after laser trabeculoplasty in vivo. J Glaucoma. 1994;3:36-43.
[27] Acott TS, Samples JR, Bradley JM, Bacon DR, Bylsma SS, Van Buskirk EM. Trabecular repopulation by anterior trabecular meshwork cells after laser trabeculoplasty. Am J Ophthalmol. 1989;107:1-6.
[28] Alexander RA, Grierson I. Morphological effects of argon laser trabeculoplasty upon the glaucomatous human meshwork. Eye. 1989;3:719–26.
[29] Koller T, Sturmer J, Reme C, Gloor B. Membrane formation in the chamber angle after failure of argon laser trabeculoplasty: analysis of risk factors. Br J Ophthalmol. 2000;84:48-53.
[30] Wilensky JT, Weinreb RN. Early and late failures of argon laser trabeculoplasty. Arch Ophthalmol. 1983;101:895-7.
[31] Richter CU, Shingleton BJ, Bellows AR, Hutchinson BT, Jacobson LP. Retreatment with argon laser trabeculoplasty. Ophthalmology. 1987;94:1085-9.
[32] The Glaucoma Laser Trial (GLT). 2. Results of argon laser trabeculoplasty versus topical medicines. The Glaucoma Laser Trial Research Group. Ophthalmology. 1990;97:1403-13.
[33] Harkins T. The glaucoma laser trial. Clin Eye Vis Care. 1996;8:51–4.
[34] Feldman RM, Katz LJ, Spaeth GL, Crapotta JA, Fahmy IA, Ali MA. Long-term efficacy of repeat argon laser trabeculoplasty. Ophthalmology. 1991;98:1061-5.
[35] Mermoud A, Pittet N, Herbort CP. Inflammation patterns after laser trabeculoplasty measured with the laser flare meter. Arch Ophthalmol. 1992;110:368-70.
[36] Rouhiainen HJ, Terasvirta ME, Tuovinen EJ. Peripheral anterior synechiae formation after trabeculoplasty. Arch Ophthalmol. 1988;106:189-91.
[37] Traverso CE, Greenidge KC, Spaeth GL. Formation of peripheral anterior synechiae following argon laser trabeculoplasty. A prospective study to determine relationship to position of laser burns. Arch Ophthalmol. 1984;102:861-3.
[38] Schwartz AL, Love DC, Schwartz MA. Long-term follow-up of argon laser trabeculoplasty for uncontrolled open-angle glaucoma. Arch Ophthalmol. 1985;103:1482-4.
[39] Grinich NP, Van Buskirk EM, Samples JR. Three-year efficacy of argon laser trabeculoplasty. Ophthalmology. 1987;94:858-61.
[40] The Glaucoma Laser Trial (GLT) and glaucoma laser trial follow-up study: 7. Results. Glaucoma Laser Trial Research Group. Am J Ophthalmol. 1995;120:718-31.
[41] Latina MA, Park C. Selective targeting of trabecular meshwork cells: in vitro studies of pulsed and CW laser interactions. Exp Eye Res. 1995;60:359-71.
[42] Latina MA, Sibayan SA, Shin DH, Noecker RJ, Marcellino G. Q-switched 532-nm Nd:YAG laser trabeculoplasty (selective laser trabeculoplasty): a multicenter, pilot, clinical study. Ophthalmology. 1998;105:2082-8; discussion 9-90.
[43] Anderson RR, Parrish JA. Selective photothermolysis: precise microsurgery by selective absorption of pulsed radiation. Science. 1983;220:524-7.
[44] Kramer TR, Noecker RJ. Comparison of the morphologic changes after selective laser trabeculoplasty and argon laser trabeculoplasty in human eye bank eyes. Ophthalmology. 2001;108:773-9.
[45] Alvarado JA, Alvarado RG, Yeh RF, Franse-Carman L, Marcellino GR, Brownstein MJ. A new insight into the cellular regulation of aqueous outflow: how trabecular meshwork endothelial cells drive a mechanism that regulates the permeability of Schlemm's canal endothelial cells. Br J Ophthalmol. 2005;89:1500–5.

[46] Alvarado JA, Yeh RF, Franse-Carman L, Marcellino G, Brownstein MJ. Interactions between endothelia of the trabecular meshwork and of Schlemm's canal: a new insight into the regulation of aqueous outflow in the eye. Trans Am Ophthalmol Soc. 2005;103:148–63.
[47] Alvarado JA, Katz LJ, Trivedi S, Shifera AS. Monocyte modulation of aqueous outflow and recruitment to the trabecular meshwork following selective laser trabeculoplasty. Arch Ophthalmol. 2010;128:731-7.
[48] Lee JY, Kagan DB, Roumeliotis G, Liu H, Hutnik CM. Secretion of matrix metalloproteinase-3 by co-cultured pigmented and non-pigmented human trabecular meshwork cells following selective laser trabeculoplasty. Clin Exp Ophthalmol. 2016;44:33-42.
[49] Khouri AS, Lin J, Berezina TL, Maltzman B, Fechtner RD. Repeat selective laser trabeculoplasty can be effective in eyes with initial modest response. Middle East Afr J Op. 2014;21:205-9.
[50] Tang M, Fu Y, Fu MS, Fan Y, Zou HD, Sun XD, et al. The efficacy of low-energy selective laser trabeculoplasty. Ophthalmic Surg Lasers Imaging. 2011;42:59-63.
[51] Polat J, Grantham L, Mitchell K, Realini T. Repeatability of selective laser trabeculoplasty. Br J Ophthalmol. 2016;100:1437-41.
[52] Francis BA, Loewen N, Hong B, Dustin L, Kaplowitz K, Kinast R, et al. Repeatability of selective laser trabeculoplasty for open-angle glaucoma. BMC Ophthalmol. 2016;16:128.
[53] Avery N, Ang GS, Nicholas S, Wells A. Repeatability of primary selective laser trabeculoplasty in patients with primary open-angle glaucoma. Int Ophthalmol. 2013;33:501-6.
[54] Cvenkel B, Hvala A, Drnovsek-Olup B, Gale N. Acute ultrastructural changes of the trabecular meshwork after selective laser trabeculoplasty and low power argon laser trabeculoplasty. Laser Surg Med. 2003;33:204-8.
[55] Juzych MS, Chopra V, Banitt MR, Hughes BA, Kim C, Goulas MT, et al. Comparison of long-term outcomes of selective laser trabeculoplasty versus argon laser trabeculoplasty in open-angle glaucoma. Ophthalmology. 2004;111:1853-9.
[56] Song J, Lee PP, Epstein DL, Stinnett SS, Herndon LW, Jr., Asrani SG, et al. High failure rate associated with 180 degrees selective laser trabeculoplasty. J Glaucoma. 2005;14:400-8.
[57] Leahy KE, White AJ. Selective laser trabeculoplasty: current perspectives. Clin Ophthalmol. 2015;9:833-41.
[58] Song J. Complications of selective laser trabeculoplasty: a review. Clin Ophthalmol. 2016;10:137-43.
[59] Gedde SJ, Schiffman JC, Feuer WJ, Herndon LW, Brandt JD, Budenz DL. Treatment outcomes in the tube versus trabeculectomy study after one year of follow-up. Am J Ophthalmol. 2007;143:9-22.
[60] Gedde SJ, Schiffman JC, Feuer WJ, Herndon LW, Brandt JD, Budenz DL, et al. Treatment outcomes in the Tube Versus Trabeculectomy (TVT) study after five years of follow-up. Am J Ophthalmol. 2012;153:789-803 e2.
[61] Christakis PG, Zhang D, Budenz DL, Barton K, Tsai JC, Ahmed IIK, et al. Five-Year Pooled Data Analysis of the Ahmed Baerveldt Comparison Study and the Ahmed Versus Baerveldt Study. Am J Ophthalmol. 2017;176:118-26.
[62] Shaarawy T, Goldberg I, Fechtner R. EX-PRESS glaucoma filtration device: Review of clinical experience and comparison with trabeculectomy. Surv Ophthalmol. 2015;60:327-45.
[63] Investigators A. The Advanced Glaucoma Intervention Study (AGIS): 11. Risk factors for failure of trabeculectomy and argon laser trabeculoplasty. Am J Ophthalmol. 2002;134:481-98.
[64] Lee RMH, Bouremel Y, Eames I, Brocchini S, Khaw PT. Translating Minimally Invasive Glaucoma Surgery Devices. Clin Transl Sci. 2020;13:14-25.
[65] Mikula E, Holland G, Bradford S, Khazaeinezhad R, Srass H, Suarez C, et al. Intraocular Pressure Reduction by Femtosecond Laser Created Trabecular Channels in Perfused Human Anterior Segments. Transl Vis Sci Technol. 2021;10:22.

[66] Mikula ER, Raksi F, Ahmed, II, Sharma M, Holland G, Khazaeinezhad R, et al. Femtosecond Laser Trabeculotomy in Perfused Human Cadaver Anterior Segments: A Novel, Noninvasive Approach to Glaucoma Treatment. Transl Vis Sci Technol. 2022;11:28.
[67] Luo S, Mikula ER, Bradford S, Joshi R, Zhang F, Farrah E, et al. Evaluating the Effect of Pulse Energy on Femtosecond Laser Trabeculotomy (FLT) Drainage Channels in Human Cadaver Eyes. Invest Ophthalmol Vis Sci. 2023;64:4896.
[68] Mikula ER, Djotyan G, Luo S, Jester JV, Juhasz T. Femtosecond Laser Image Guided High-precision Trabeculotomy (FLigHT): a thermal collateral damage study. Invest Ophthalmol Vis Sci. 2023;64:4907.
[69] Juhasz T, Kastis GA, Suarez C, Bor Z, Bron WE. Time-resolved observations of shock waves and cavitation bubbles generated by femtosecond laser pulses in corneal tissue and water. Laser Surg Med. 1996;19:23-31.
[70] Juhasz T, Kurtz R, Raksi F, Suarez C, Horvath C, Spooner G. The Femtosecond Blade: Applications in Corneal Surgery. Optics and Photonics News. 2002;13:24-9.
[71] Juhasz T, Frieder H, Kurtz RM, Horvath C, Bille JF, Mourou G. Corneal refractive surgery with femtosecond lasers. Ieee J Sel Top Quant. 1999;5:902-10.
[72] Ratkay-Traub I, Juhasz T, Horvath C, Suarez C, Kiss K, Ferincz I, et al. Ultra-short pulse (femtosecond) laser surgery: initial use in LASIK flap creation. Ophthalmol Clin North Am. 2001;14:347-55, viii-ix.
[73] Palanker DV, Blumenkranz MS, Andersen D, Wiltberger M, Marcellino G, Gooding P, et al. Femtosecond laser-assisted cataract surgery with integrated optical coherence tomography. Sci Transl Med. 2010;2:58ra85.
[74] Nagy ZZ, McAlinden C. Femtosecond laser cataract surgery. Eye Vis (Lond). 2015;2:11.
[75] Nichols KK, Foulks GN, Bron AJ, Glasgow BJ, Dogru M, Tsubota K, et al. The international workshop on meibomian gland dysfunction: executive summary. Invest Ophthalmol Vis Sci. 2011;52:1922-9.
[76] Tomlinson A, Bron AJ, Korb DR, Amano S, Paugh JR, Pearce EI, et al. The international workshop on meibomian gland dysfunction: report of the diagnosis subcommittee. Invest Ophthalmol Vis Sci. 2011;52:2006-49.
[77] Farrand KF, Fridman M, Stillman IÖ, Schaumberg DA. Prevalence of Diagnosed Dry Eye Disease in the United States Among Adults Aged 18 Years and Older. Am J Ophthalmol. 2017;182:90-8.
[78] Yu J, Asche CV, Fairchild CJ. The economic burden of dry eye disease in the United States: a decision tree analysis. Cornea. 2011;30:379-87.
[79] Kojima T, Dogru M, Kawashima M, Nakamura S, Tsubota K. Advances in the diagnosis and treatment of dry eye. Prog Retin Eye Res. 2020;78.
[80] Geerling G, Tauber J, Baudouin C, Goto E, Matsumoto Y, O'Brien T, et al. The international workshop on meibomian gland dysfunction: report of the subcommittee on management and treatment of meibomian gland dysfunction. Invest Ophthalmol Vis Sci. 2011;52:2050-64.
[81] Thode AR, Latkany RA. Current and Emerging Therapeutic Strategies for the Treatment of Meibomian Gland Dysfunction (MGD). Drugs. 2015;75:1177-85.
[82] Villani E, Garoli E, Canton V, Pichi F, Nucci P, Ratiglia R. Evaluation of a novel eyelid-warming device in meibomian gland dysfunction unresponsive to traditional warm compress treatment: an in vivo confocal study. Int Ophthalmol. 2015;35:319-23.
[83] Doan S, Chiambaretta F, Baudouin C, group Es. Evaluation of an eyelid warming device (Blephasteam) for the management of ocular surface diseases in France: the ESPOIR study. J Fr Ophtalmol. 2014;37:763-72.
[84] Purslow C. Evaluation of the ocular tolerance of a novel eyelid-warming device used for meibomian gland dysfunction. Cont Lens Anterior Eye. 2013;36:226-31.
[85] Greiner JV. A single LipiFlow(R) Thermal Pulsation System treatment improves meibomian gland function and reduces dry eye symptoms for 9 months. Curr Eye Res. 2012;37:272-8.

[86] Friedland BR, Fleming CP, Blackie CA, Korb DR. A novel thermodynamic treatment for meibomian gland dysfunction. Curr Eye Res. 2011;36:79-87.
[87] Korb DR, Blackie CA. Restoration of meibomian gland functionality with novel thermodynamic treatment device-a case report. Cornea. 2010;29:930-3.
[88] Goto E, Monden Y, Takano Y, Mori A, Shimmura S, Shimazaki J, et al. Treatment of non-inflamed obstructive meibomian gland dysfunction by an infrared warm compression device. Br J Ophthalmol. 2002;86:1403-7.
[89] Kaido M, Ibrahim OM, Kawashima M, Ishida R, Sato EA, Tsubota K. Eyelid cleansing with ointment for obstructive meibomian gland dysfunction. Jpn J Ophthalmol. 2017;61:124-30.
[90] Tanabe H, Kawashima M, Kaido M, Ishida R, Kawakita T, Tsubota K. Safety and efficacy of wiping lid margins with lid hygiene shampoo using the "eye brush", a novel lid hygiene item, in healthy subjects: a pilot study. Bmc Ophthalmol. 2019;19.
[91] Okura M, Kawashima M, Katagiri M, Shirasawa T, Tsubota K. New Eye Cleansing Product Improves Makeup-Related Ocular Problems. J Ophthalmol. 2015;2015.
[92] Aketa N, Shinzawa M, Kawashima M, Dogru M, Okamoto S, Tsubota K, et al. Efficacy of Plate Expression of Meibum on Tear Function and Ocular Surface Findings in Meibomian Gland Disease. Eye Contact Lens. 2019;45:19-22.
[93] Nakayama N, Kawashima M, Kaido M, Arita R, Tsubota K. Analysis of Meibum Before and After Intraductal Meibomian Gland Probing in Eyes With Obstructive Meibomian Gland Dysfunction. Cornea. 2015;34:1206-8.
[94] Giannaccare G, Pellegrini M, Sebastiani S, Bernabei F, Roda M, Taroni L, et al. Efficacy of Omega-3 Fatty Acid Supplementation for Treatment of Dry Eye Disease: A Meta-Analysis of Randomized Clinical Trials. Cornea. 2019;38:565-73.
[95] Goto E, Dogru M, Fukagawa K, Uchino M, Matsumoto Y, Saiki M, et al. Successful tear lipid layer treatment for refractory dry eye in office workers by low-dose lipid application on the full-length eyelid margin. Am J Ophthalmol. 2006;142:264-70.
[96] Management and therapy of dry eye disease: report of the Management and Therapy Subcommittee of the International Dry Eye WorkShop (2007). Ocul Surf. 2007;5:163-78.
[97] Vergs C, Salgado-Borges J, de Ribot FM, Ribas V. Current developments of intensive pulsed light treatment for dry eye disease and meibomian gland dysfunction. Expert Rev Ophthalmo. 2021;16:401-9.
[98] Barbosa Ribeiro B, Marta A, Ponces Ramalhao J, Marques JH, Barbosa I. Pulsed Light Therapy in the Management of Dry Eye Disease: Current Perspectives. Clin Ophthalmol. 2022;16:3883-93.
[99] Giannaccare G, Taroni L, Senni C, Scorcia V. Intense Pulsed Light Therapy In The Treatment Of Meibomian Gland Dysfunction: Current Perspectives. Clin Optom (Auckl). 2019;11:113-26.
[100] Zhang-Nunes S, Guo S, Lee D, Chang J, Nguyen A. Safety and Efficacy of an Augmented Intense Pulse Light Protocol for Dry Eye Syndrome and Blepharitis. Photobiomodul Photomed Laser Surg. 2021;39:178-84.
[101] Xu L, Wu Y, Song Y, Zhang Q, Qin G, Yang L, et al. Comparison Between Heated Eye Mask and Intense Pulsed Light Treatment for Contact Lens-Related Dry Eye. Photobiomodul Photomed Laser Surg. 2022;40:189-97.
[102] Yang L, Pazo EE, Zhang Q, Wu Y, Song Y, Qin G, et al. Treatment of contact lens related dry eye with intense pulsed light. Cont Lens Anterior Eye. 2022;45:101449.
[103] Yang L, Pazo EE, Qin G, Zhang Q, Wu Y, Song Y, et al. Effect of Intense Pulsed Light on Anterior Corneal Aberrations and Quality of Vision in Patients with Evaporative Dry Eye. Photobiomodul Photomed Laser Surg. 2021;39:185-95.
[104] Toyos R, Desai NR, Toyos M, Dell SJ. Intense pulsed light improves signs and symptoms of dry eye disease due to meibomian gland dysfunction: A randomized controlled study. Plos One. 2022;17.

[105] Jiang X, Yuan H, Zhang M, Lv H, Chou Y, Yang J, et al. The Efficacy and Safety of New-Generation Intense Pulsed Light in the Treatment of Meibomian Gland Dysfunction-Related Dry Eye: A Multicenter, Randomized, Patients-Blind, Parallel-Control, Non-Inferiority Clinical Trial. Ophthalmol Ther. 2022;11:1895-912.
[106] Arita R, Fukuoka S, Mizoguchi T, Morishige N. Multicenter Study of Intense Pulsed Light for Patients with Refractory Aqueous-Deficient Dry Eye Accompanied by Mild Meibomian Gland Dysfunction. J Clin Med. 2020;9.
[107] Pazo EE, Huang H, Fan Q, Zhang C, Yue Y, Yang L, et al. Intense Pulse Light for Treating Post-LASIK Refractory Dry Eye. Photobiomodul Photomed Laser Surg. 2021;39:155-63.
[108] Vergés C, Salgado-Borges J, de Ribot FM. Prospective evaluation of a new intense pulsed light, thermaeye plus, in the treatment of dry eye disease due to meibomian gland dysfunction. J Optom. 2021;14:103-13.
[109] Toyos R, Toyos M, Willcox J, Mulliniks H, Hoover J. Evaluation of the Safety and Efficacy of Intense Pulsed Light Treatment with Meibomian Gland Expression of the Upper Eyelids for Dry Eye Disease. Photobiomodul Photomed Laser Surg. 2019;37:527-31.
[110] Suwal A, Hao JL, Zhou DD, Liu XF, Suwal R, Lu CW. Use of Intense Pulsed Light to Mitigate Meibomian Gland Dysfunction for Dry Eye Disease. Int J Med Sci. 2020;17:1385-92.
[111] Mejia LF, Gil JC, Jaramillo M. Intense pulsed light therapy: A promising complementary treatment for dry eye disease. Arch Soc Esp Oftalmol (Engl Ed). 2019;94:331-6.
[112] Guilloto Caballero S, Garcia Madrona JL, Colmenero Reina E. Effect of pulsed laser light in patients with dry eye syndrome. Arch Soc Esp Oftalmol. 2017;92:509-15.
[113] Vigo L, Giannaccare G, Sebastiani S, Pellegrini M, Carones F. Intense Pulsed Light for the Treatment of Dry Eye Owing to Meibomian Gland Dysfunction. J Vis Exp. 2019.
[114] Rong B, Tang Y, Liu R, Tu P, Qiao J, Song W, et al. Long-Term Effects of Intense Pulsed Light Combined with Meibomian Gland Expression in the Treatment of Meibomian Gland Dysfunction. Photomed Laser Surg. 2018;36:562-7.
[115] Yin Y, Liu N, Gong L, Song N. Changes in the Meibomian Gland After Exposure to Intense Pulsed Light in Meibomian Gland Dysfunction (MGD) Patients. Curr Eye Res. 2018;43:308-13.
[116] Dell SJ, Gaster RN, Barbarino SC, Cunningham DN. Prospective evaluation of intense pulsed light and meibomian gland expression efficacy on relieving signs and symptoms of dry eye disease due to meibomian gland dysfunction. Clin Ophthalmol. 2017;11:817-27.
[117] Arita R, Fukuoka S, Morishige N. Therapeutic efficacy of intense pulsed light in patients with refractory meibomian gland dysfunction. Ocul Surf. 2019;17:104-10.
[118] Craig JP, Chen YH, Turnbull PR. Prospective trial of intense pulsed light for the treatment of meibomian gland dysfunction. Invest Ophthalmol Vis Sci. 2015;56:1965-70.
[119] Toyos R, McGill W, Briscoe D. Intense Pulsed Light Treatment for Dry Eye Disease Due to Meibomian Gland Dysfunction; A 3-Year Retrospective Study. Photomed Laser Surg. 2015;33:41-6.
[120] Fineide F, Magno MS, Khan AZ, Chen X, Vehof J, Utheim TP. Intense pulsed light treatment in meibomian gland dysfunction: Past, present, and future. Acta Ophthalmol. 2023.
[121] Tashbayev B, Yazdani M, Arita R, Fineide F, Utheim TP. Intense pulsed light treatment in meibomian gland dysfunction: A concise review. Ocul Surf. 2020;18:583-94.
[122] Park Y, Kim H, Kim S, Cho KJ. Effect of low-level light therapy in patients with dry eye: a prospective, randomized, observer-masked trial. Sci Rep. 2022;12:3575.
[123] Giannaccare G, Vaccaro S, Pellegrini M, Borselli M, Carnovale Scalzo G, Taloni A, et al. Serial Sessions of a Novel Low-Level Light Therapy Device for Home Treatment of Dry Eye Disease. Ophthalmol Ther. 2023;12:459-68.
[124] Markoulli M, Chandramohan N, Papas EB. Photobiomodulation (low-level light therapy) and dry eye disease. Clin Exp Optom. 2021;104:561-6.

[125] Antwi A, Nti AN, Ritchey ER. Thermal effect on eyelid and tear film after low-level light therapy and warm compress. Clin Exp Optom. 2023:1-7.
[126] Ballesteros-Sanchez A, Gargallo-Martinez B, Sanchez-Gonzalez MC, Sanchez-Gonzalez JM. Intense Pulse Light Combined With Low-Level Light Therapy in Dry Eye Disease: A Systematic Review. Eye Contact Lens. 2023;49:8-13.
[127] Stonecipher K, Abell TG, Chotiner B, Chotiner E, Potvin R. Combined low level light therapy and intense pulsed light therapy for the treatment of meibomian gland dysfunction. Clin Ophthalmol. 2019;13:993-9.
[128] Naudin T, Thorel D, Tetart F, Muraine M, Gueudry J. Combined Intense Pulsed Light and low-level light therapy in the treatment of Meibomian gland dysfunction. J Fr Ophtalmol. 2021;44:1021-8.
[129] El Shami M, Maroun A, Hoyek S, Antoun J. Optimized combined low level light therapy and intense pulsed light therapy for the treatment of dry eye syndrome caused by Meibomian glands dysfunction. J Fr Ophtalmol. 2022;45:1126-36.
[130] Perez-Silguero MA, Perez-Silguero D, Rivero-Santana A, Bernal-Blasco MI, Encinas-Pisa P. Combined Intense Pulsed Light and Low-Level Light Therapy for the Treatment of Dry Eye: A Retrospective Before-After Study with One-Year Follow-Up. Clin Ophthalmol. 2021;15:2133-40.
[131] Di Marino M, Conigliaro P, Aiello F, Valeri C, Giannini C, Mancino R, et al. Combined Low-Level Light Therapy and Intense Pulsed Light Therapy for the Treatment of Dry Eye in Patients with Sjogren's Syndrome. J Ophthalmol. 2021;2021:2023246.
[132] Meduri A, Oliverio GW, Tedesco G, Aragona P. Combined intense pulsed light and low-level light therapy for the treatment of refractory Meibomian gland dysfunction. Eur J Ophthalmol. 2022:11206721221127206.
[133] Marques JH, Marta A, Baptista PM, Almeida D, Jose D, Sousa PJM, et al. Low-Level Light Therapy in Association with Intense Pulsed Light for Meibomian Gland Dysfunction. Clin Ophthalmol. 2022;16:4003-10.
[134] Giannaccare G, Pellegrini M, Carnovale Scalzo G, Borselli M, Ceravolo D, Scorcia V. Low-Level Light Therapy Versus Intense Pulsed Light for the Treatment of Meibomian Gland Dysfunction: Preliminary Results From a Prospective Randomized Comparative Study. Cornea. 2023;42:141-4.
[135] He Y, Qu Y, Zhu J, Zhang Y, Saidi A, Ma T, et al. Confocal Shear Wave Acoustic Radiation Force Optical Coherence Elastography for Imaging and Quantification of the In Vivo Posterior Eye. IEEE J Sel Top Quantum Electron. 2019;25.
[136] Toyran S, Liu Y, Singha S, Shan S, Cho MR, Gordon RJ, et al. Femtosecond laser photodisruption of human trabecular meshwork: an in vitro study. Exp Eye Res. 2005;81:298-305.
[137] Liu Y, Nakamura H, Witt TE, Edward DP, Gordon RJ. Femtosecond laser photodisruption of porcine anterior chamber angle: an ex vivo study. Ophthalmic Surg Lasers Imaging. 2008;39:485-90.
[138] Nakamura H, Liu Y, Witt TE, Gordon RJ, Edward DP. Femtosecond laser photodisruption of primate trabecular meshwork: an ex vivo study. Invest Ophthalmol Vis Sci. 2009;50:1198-204.
[139] Luo S, Holland G, Khazaeinezhad R, Bradford S, Joshi R, Juhasz T. Iridocorneal angle imaging of a human donor eye by spectral-domain optical coherence tomography. Sci Rep. 2023;13:13861.
[140] Nagy ZZ, Kranitz K, Ahmed IIK, De Francesco T, Mikula E, Juhasz T. First-in-Human Safety Study of Femtosecond Laser Image-Guided Trabeculotomy for Glaucoma Treatment: 24-month Outcomes. Ophthalmol Sci. 2023;3:100313.
[141] Mikula ER, Raksi F, Ahmed II, Sharma M, Holland G, Khazaeinezhad R, et al. Femtosecond Laser Trabeculotomy in Perfused Human Cadaver Anterior Segments: A Novel, Noninvasive Approach to Glaucoma Treatment. Translational Vision Science & Technology. 2022;11:28-.
[142] Mikula E, Holland G, Srass H, Suarez C, Jester JV, Juhasz T. Intraocular Pressure Reduction by Femtosecond Laser Created Trabecular Channels in Perfused Human Anterior Segments. Transl Vis Sci Technol. 2021;10:22.

[143] Liao CS, Zhuo ZY, Yu JY, Tzeng YY, Chu SW, Yu SF, et al. Decrimping: The first stage of collagen thermal denaturation unraveled by in situ second-harmonic-generation imaging. Appl Phys Lett. 2011;98.
[144] Sun Y, Chen W-L, Lin S-J, Jee S-H, Chen Y-F, Lin L-C, et al. Investigating Mechanisms of Collagen Thermal Denaturation by High Resolution Second-Harmonic Generation Imaging. Biophysical Journal. 2006;91:2620-5.
[145] Bozec L, Odlyha M. Thermal denaturation studies of collagen by microthermal analysis and atomic force microscopy. Biophys J. 2011;101:228-36.
[146] Derman ID, Senel EC, Ferhanoglu O, Cilesiz I, Kazanci M. Effect of Heat Level and Expose Time on Denaturation of Collagen Tissues. Cell Mol Bioeng. 2021;14:113-9.
[147] Sun Y, Chen WL, Lin SJ, Jee SH, Chen YF, Lin LC, et al. Investigating mechanisms of collagen thermal denaturation by high resolution second-harmonic generation imaging. Biophys J. 2006;91:2620-5.
[148] Ammar DA, Seibold LK, Kahook MY. Preclinical Investigation of Goniotomy Using Four Different Techniques. Clin Ophthalmol. 2020;14:3519-25.
[149] Seibold LK, Soohoo JR, Ammar DA, Kahook MY. Preclinical investigation of ab interno trabeculectomy using a novel dual-blade device. Am J Ophthalmol. 2013;155:524-9 e2.
[150] Joseph A. Izatt MAC, and Al-Hafeez Dhalla. Theory of Optical Coherence Tomography. In: Drexler W, Fujimoto JG, editors. Optical Coherence Tomography: Technology and Applications. 2 ed: Springer; 2015.
[151] Wojtkowski M, Srinivasan V, Ko T, Fujimoto J, Kowalczyk A, Duker J. Ultrahigh-resolution, high-speed, Fourier domain optical coherence tomography and methods for dispersion compensation. Opt Express. 2004;12:2404-22.
[152] Cohen L. Time-Frequency Analysis. 1 ed: Prentice Hall; 1995.
[153] Cense B, Nassif N, Chen T, Pierce M, Yun SH, Park B, et al. Ultrahigh-resolution high-speed retinal imaging using spectral-domain optical coherence tomography. Opt Express. 2004;12:2435-47.
[154] Scheie HG. Width and pigmentation of the angle of the anterior chamber; a system of grading by gonioscopy. AMA Arch Ophthalmol. 1957;58:510-2.
[155] Hillmann D, Bonin T, Luhrs C, Franke G, Hagen-Eggert M, Koch P, et al. Common approach for compensation of axial motion artifacts in swept-source OCT and dispersion in Fourier-domain OCT. Opt Express. 2012;20:6761-76.
[156] Ni GM, Liu L, Liu JX, Zhang J, Wang XZ, Du XH, et al. Detection and compensation of dispersion mismatch for frequency-domain optical coherence tomography based on A-scan's spectrogram. Optics Express. 2020;28:19229-41.
[157] Yasuno Y, Hong Y, Makita S, Yamanari M, Akiba M, Miura M, et al. In vivo high-contrast imaging of deep posterior eye by 1-microm swept source optical coherence tomography and scattering optical coherence angiography. Opt Express. 2007;15:6121-39.
[158] Kagemann L, Wollstein G, Ishikawa H, Bilonick RA, Brennen PM, Folio LS, et al. Identification and assessment of Schlemm's canal by spectral-domain optical coherence tomography. Invest Ophthalmol Vis Sci. 2010;51:4054-9.
[159] Montes-Mico R, Tana-Rivero P, Aguilar-Corcoles S, Ruiz-Santos M, Rodriguez-Carrillo MD, Ruiz-Mesa R. Angle-to-angle and spur-to-spur distance analysis with high-resolution optical coherence tomography. Eye Vis (Lond). 2020;7:42.
[160] Delori FC, Webb RH, Sliney DH, American National Standards I. Maximum permissible exposures for ocular safety (ANSI 2000), with emphasis on ophthalmic devices. J Opt Soc Am A Opt Image Sci Vis. 2007;24:1250-65.
[161] Spaide RF, Koizumi H, Pozzoni MC. Enhanced depth imaging spectral-domain optical coherence tomography. Am J Ophthalmol. 2008;146:496-500.
[162] Zhang X, Beckmann L, Miller DA, Shao G, Cai Z, Sun C, et al. In Vivo Imaging of Schlemm's Canal and Limbal Vascular Network in Mouse Using Visible-Light OCT. Invest Ophthalmol Vis Sci. 2020;61:23.

[163] Chiu SJ, Li XT, Nicholas P, Toth CA, Izatt JA, Farsiu S. Automatic segmentation of seven retinal layers in SDOCT images congruent with expert manual segmentation. Opt Express. 2010;18:19413-28.
[164] Huang AS, Belghith A, Dastiridou A, Chopra V, Zangwill LM, Weinreb RN. Automated circumferential construction of first-order aqueous humor outflow pathways using spectral-domain optical coherence tomography. J Biomed Opt. 2017;22:66010.
[165] Yao X, Tan B, Ho Y, Liu X, Wong D, Chua J, et al. Full circumferential morphological analysis of Schlemm's canal in human eyes using megahertz swept source OCT. Biomed Opt Express. 2021;12:3865-77.
[166] Linton RG, Curnow DH, Riley WJ. The Meibomian Glands: An Investigation into the Secretion and Some Aspects of the Physiology. Br J Ophthalmol. 1961;45:718-23.
[167] Cui X, Wu Q, Zhai Z, Yang Y, Wei A, Xu J, et al. Comparison of the Meibomian Gland Openings by Optical Coherence Tomography in Obstructive Meibomian Gland Dysfunction and Normal Patients. J Clin Med. 2020;9.
[168] Rosenfeld L, Cerretani C, Leiske DL, Toney MF, Radke CJ, Fuller GG. Structural and rheological properties of meibomian lipid. Invest Ophthalmol Vis Sci. 2013;54:2720-32.
[169] Doke J. GRABIT. MATLAB Central File Exchange; 2023.
[170] Papanastasiou TC. Flows of Materials with Yield. J Rheol. 1987;31:385-404.
[171] Chew CK, Jansweijer C, Tiffany JM, Dikstein S, Bron AJ. An instrument for quantifying meibomian lipid on the lid margin: the Meibometer. Curr Eye Res. 1993;12:247-54.
[172] Mitchell JW. Fox and McDonald's Introduction to fluid mechanics. 10th ed. Hoboken, NJ: Wiley; 2020.
[173] Nagymihalyi A, Dikstein S, Tiffany JM. The influence of eyelid temperature on the delivery of meibomian oil. Exp Eye Res. 2004;78:367-70.
[174] Fatt I, Weissman BA. Physiology of the eye: an introduction to the vegetative functions. 2nd ed. Boston: Butterworth-Heinemann; 1992.
[175] Butovich IA, Lu H, McMahon A, Ketelson H, Senchyna M, Meadows D, et al. Biophysical and morphological evaluation of human normal and dry eye meibum using hot stage polarized light microscopy. Invest Ophthalmol Vis Sci. 2014;55:87-101.
[176] McCulley JP, Shine WE. Meibomian secretions in chronic blepharitis. Adv Exp Med Biol. 1998;438:319-26.
[177] Shrestha RK, Borchman D, Foulks GN, Yappert MC, Milliner SE. Analysis of the composition of lipid in human meibum from normal infants, children, adolescents, adults, and adults with meibomian gland dysfunction using (1)H-NMR spectroscopy. Invest Ophthalmol Vis Sci. 2011;52:7350-8.
[178] Sullivan BD, Evans JE, Dana MR, Sullivan DA. Influence of aging on the polar and neutral lipid profiles in human meibomian gland secretions. Arch Ophthalmol. 2006;124:1286-92.
[179] Iyengar BT, Schlenk H. Melting points of synthetic wax esters. Lipids. 1969;4:28-30.
[180] Mahadevan V, Lundberg W. Preparation of cholesterol esters of long-chain fatty acids and characterization of cholesteryl arachidonate. Journal of Lipid Research. 1962;3:106-10.
[181] Ong BL, Hodson SA, Wigham T, Miller F, Larke JR. Evidence for keratin proteins in normal and abnormal human meibomian fluids. Curr Eye Res. 1991;10:1113-9.
[182] Palaniappan CK, Schutt BS, Brauer L, Schicht M, Millar TJ. Effects of keratin and lung surfactant proteins on the surface activity of meibomian lipids. Invest Ophthalmol Vis Sci. 2013;54:2571-81.
[183] Coleman DJ, Trokel S. Direct-recorded intraocular pressure variations in a human subject. Arch Ophthalmol. 1969;82:637-40.
[184] Korb DR, Blackie CA. Meibomian gland diagnostic expressibility: correlation with dry eye symptoms and gland location. Cornea. 2008;27:1142-7.

[185] van den Bosch J, Pennisi V, Mansouri K, Weinreb RN, Thieme H, Hoffmann MB, et al. Effect of eyelid muscle action and rubbing on telemetrically obtained intraocular pressure in patients with glaucoma with an IOP sensor implant. Br J Ophthalmol. 2022.
[186] Miller D. Pressure of the lid on the eye. Arch Ophthalmol. 1967;78:328-30.
[187] Sakai E, Shiraishi A, Yamaguchi M, Ohta K, Ohashi Y. Blepharo-tensiometer: new eyelid pressure measurement system using tactile pressure sensor. Eye Contact Lens. 2012;38:326-30.
[188] Shaw AJ, Collins MJ, Davis BA, Carney LG. Eyelid pressure and contact with the ocular surface. Invest Ophthalmol Vis Sci. 2010;51:1911-7.
[189] Wang J, Bao J, Song W, Li S, Hao Y, Tian L, et al. Assessment of Eyelid Pressure Using a Novel Pressure Measurement Device in Patients With Moderate-to-Severe Dry Eye Disease. Front Med (Lausanne). 2022;9:833576.
[190] Yamaguchi M, Shiraishi A. Relationship Between Eyelid Pressure and Ocular Surface Disorders in Patients With Healthy and Dry Eyes. Invest Ophth Vis Sci. 2018;59.
[191] Reneker LW, Irlmeier RT, Shui YB, Liu Y, Huang AJW. Histopathology and selective biomarker expression in human meibomian glands. Br J Ophthalmol. 2020;104:999-1004.
[192] Foulks GN, Bron AJ. Meibomian gland dysfunction: a clinical scheme for description, diagnosis, classification, and grading. Ocul Surf. 2003;1:107-26.
[193] Scopelliti MG, Kothare A, Karavitis M. A novel 1726-nm laser system for safe and effective treatment of acne vulgaris. Lasers Med Sci. 2022;37:3639-47.
[194] Tichy JA. Hydrodynamic Lubrication Theory for the Bingham Plastic-Flow Model. J Rheol. 1991;35:477-96.

SUPPLEMENTAL MATERIALS

Appendix 3.1: Parameters Related to STFT Processing

Table S3.1.1: [a]Effects of overlap ratio and window size on the dispersion compensated axial resolution and compute time.

	M=1024			M=512			M=256		
Overlap ratio	K_{eval}	Axial resolution (μm)	Compute time (sec)	K_{eval}	Axial resolution (μm)	Compute time (sec)	K_{eval}	Axial resolution (μm)	Compute time (sec)
0.99	94	2.7	5.67	257	2.7	13.71	598	2.7	27.70
0.9	10	2.7	1.69	30	2.7	2.34	69	2.7	3.90
0.8	5	2.7	1.52	15	2.7	1.58	35	2.7	2.45
0.7	4	2.7	1.46	10	2.7	1.67	24	2.7	2.07
0.6	-	N.A.	-	8	2.7	1.40	18	2.7	2.10
0.5	-	N.A.	-	7	2.7	1.63	15	2.7	1.82
0.4	-	N.A.	-	5	2.7	1.48	12	2.7	1.62
0.3	-	N.A.	-	5	2.7	1.39	10	2.7	1.59
0.2	-	N.A.	-	4	2.7	1.56	9	2.7	1.46
0.1	-	N.A.	-	4	2.7	1.41	8	2.7	1.36
0	-	N.A.	-	4	2.7	1.55	8	2.7	1.52
	M=128			**M=64**			**M=32**		
Overlap ratio	K_{eval}	Axial resolution (μm)	Compute time (sec)	K_{eval}	Axial resolution (μm)	Compute time (sec)	K_{eval}	Axial resolution (μm)	Compute time (sec)
0.99	961	2.7	41.97	1985	2.7	83.28	2017	2.7	83.35
0.9	148	2.7	7.66	284	2.7	12.89	505	2.7	22.23
0.8	74	2.7	3.41	153	2.8	7.38	289	2.7	13.89
0.7	50	2.7	2.79	100	2.7	5.14	202	2.7	10.05
0.6	37	2.7	2.43	77	2.7	3.41	156	2.7	8.13
0.5	31	2.7	2.01	63	2.7	3.64	127	2.7	6.23
0.4	25	2.7	1.93	51	2.7	2.98	101	2.7	5.19
0.3	22	2.7	1.96	45	2.7	2.66	88	2.7	4.24
0.2	19	2.7	1.92	39	2.7	2.60	78	2.7	3.57
0.1	17	2.7	1.74	35	2.7	2.28	70	2.7	3.17
0	16	2.7	1.60	32	2.7	2.24	64	2.7	3.25

[a]The axial resolution being evaluated uses the same mirror data that the PSF was located at 200 μm from zero-delay. Compute time is defined as the total time that 10 independent resampled A-line spectral interferograms take through the algorithm. Both the compute time and dispersion compensated axial resolutions are averaged by three repeated measurements.

Appendix 3.2: Deriving The Measured and Theoretical a_2 Values of The Glass Dispersion Block

Assuming that each dispersion block includes the measured dispersion of $a_{2,meas}$ in the unit of $(\times 10^{-11} m^2)$ and the intrinsic dispersion of $a_{2,inc}$, though small, exists within the system before the introduction of any dispersion block. From Table 3.1 in main text, we have

$$a_{2,meas} + a_{2,inc} = -4.118 \quad \text{(S3.2.1)}$$

$$2 \cdot a_{2,meas} + a_{2,inc} = -8.5078 \quad \text{(S3.2.2)}$$

By solving the above equation set, we get

$$a_{2,meas} = -4.3898 \times 10^{-11} m^2 \quad \text{(S3.2.3)}$$

$$a_{2,inc} = 0.2718 \times 10^{-11} m^2 \quad \text{(S3.2.4)}$$

The '+' and '-' signs indicate that the dispersion tends to reside on the side of the sample or reference arm, respectively. The above calculation assumes that the algorithm is capable of extracting the dispersion perfectly in both, one, or two dispersion blocks. The other extreme possibility is that there is no system intrinsic dispersion but just the algorithm's limitations in small dispersion detection. The averaged ratio of the second-order dispersion coefficients of the two dispersion blocks to that of one dispersion block is measured to be $\frac{-8.5078}{-4.118} = 2.07$ using the proposed method, comparable to the theoretical value of 2. A possibility could be both the minor system intrinsic dispersion and the algorithm's imperfectability exist. A relatively low dispersion extraction capability of our algorithm in both one and two dispersion blocks indeed seems possible but it is excluded by the following discussions.

We attempt to analytically derive the theoretical a_2 value for the completeness of this paper. Since there is no theoretical formula for characterizing the wavelength-dependent refractive index, derivation of a perfect theoretical a_2 value is not achievable. Even though, an empirical Sellmeier equation can be used to describe the relationship between the refractive index n and wavelength λ for a particular transparent medium, where the Sellmeier coefficients for the N-BAK1 glass are $C_1 = 1.12365662, C_2 = 0.309276848, C_3 = 0.881511957, B_1 = 0.00644742752\ \mu m^2,\ B_2 = 0.0222284402\ \mu m^2, B_3 = 107.297751\ \mu m^2$ (https://refractiveindex.info/).

$$n^2 - 1 = \frac{C_1 \cdot \lambda^2}{\lambda^2 - B_1} + \frac{C_2 \cdot \lambda^2}{\lambda^2 - B_2} + \frac{C_3 \cdot \lambda^2}{\lambda^2 - B_3} \quad \text{(S3.2.5)}$$

From Eq. 3.1, we have

$$\Phi = k \cdot 2d = \frac{w}{c} \cdot 2d \cdot n_g + \Delta\Phi \quad \text{(S3.2.6)}$$

Below also defines the wavenumber k and the group refractive index n_g in a dispersive medium:

$$k = \frac{wn}{c} \quad \text{(S3.2.7)}$$

$$n_g = n + w\frac{\partial n}{\partial w} \quad \text{(S3.2.8)}$$

Therefore, the phase function or dispersion compensation term is calculated by:

$$\Delta\Phi = k \cdot 2d - \frac{2dw}{c} \cdot \left(n + w\frac{\partial n}{\partial w}\right) = -\frac{2dw^2}{c}\frac{\partial n}{\partial w} \quad \text{(S3.2.9)}$$

where the speed of light in vacuum $c = 299792458\ \frac{m}{s}$ and the thickness of the glass dispersion block $d = 19.6\ mm$. Note that the wavenumber k is angular frequency dependent, or the angular frequency w is wavenumber dependent, the refractive index n is wavelength dependent, and the wavenumber and the wavelength are related by $k = \frac{2\pi}{\lambda}$.

Comparing the second-order terms in Eq. 3.2 and Eq. 3.3 yields:

$$a_{2,theory} = -\frac{1}{2} \cdot \frac{\partial^2 \Delta\Phi(k)}{\partial k^2}\bigg|_{k_0} \quad \text{(S3.2.10)}$$

Therefore, it is straightforward that $a_{2,theory}$ is achievable by calculating the $\frac{\partial^2 \Delta\Phi(k)}{\partial k^2}$ term in theory, considering the definition of the partial derivative as well as the chain rule, the product and/or quotient rule. The full expression of $\frac{\partial^2 \Delta\Phi(k)}{\partial k^2}$ can be eventually evaluated as a function of n and λ, and these are directly accessible from the Sellmeier equation.

However, it is unpractical to manually derive $\frac{\partial^2 \Delta\Phi(k)}{\partial k^2}$, and even undoable to get its full expression in Mathematica online (Wolfram Mathematica, Wolfram Research, Inc., Champaign, Illinois) due to its high compute complexity. The Mathematica can indeed compute the value of $\frac{\partial^2 \Delta\Phi(k)}{\partial k^2}\Big|_{k_0}$ and related Mathematica code is provided in italics below, where $k_0 = 7581092.7\ m^{-1}$ (central k value after k-linearization during the OCT processing).

```
c1=1.12365662;
c2=0.309276848;
c3=0.881511957;
b1=0.000000000000000644742752;
b2=0.000000000000000222284402;
b3=0.000000000107297751;
c=299792458;
d=0.0196;
l[k_]:=2*Pi/k
n[k_]:=(1+c1*l[k]^2/(l[k]^2-b1)+c2*l[k]^2/(l[k]^2-b2)+c3*l[k]^2/(l[k]^2-b3))^(1/2)
w[k_]:=c*k/n[k]
Phi[k_]:=-2*d*(w[k])^2*n'[k]/(c*w'[k])
D[Phi[k],[171]]/.k->7581092.7
```

By hitting "shift+enter", the above code directly gives us an output of -3.28396×10^{-10}. Therefore, the theoretical a_2 value of the dispersion block is $a_{2,theory} = 1.64198 \times 10^{-10}\ m^2$, which is approximately 4 times compared to our absolute measured a_2 value. This discrepancy is not attributed to our algorithm's limitation in extracting the dispersion. As we test, the $a_{2,theory}$ value (or other values close to the a_2 measured value) for the dispersion compensation broadens PSFs and blurs the OCT images compared to that when the a_2 measured value is applied. We speculate that the assumption using the empirical fitting Sellmeier equation and the compute precision of small numbers in the commercial software might be responsible for this discrepancy.

Appendix 3.3: STFT Analysis for an Entire OCT Processing Workflow

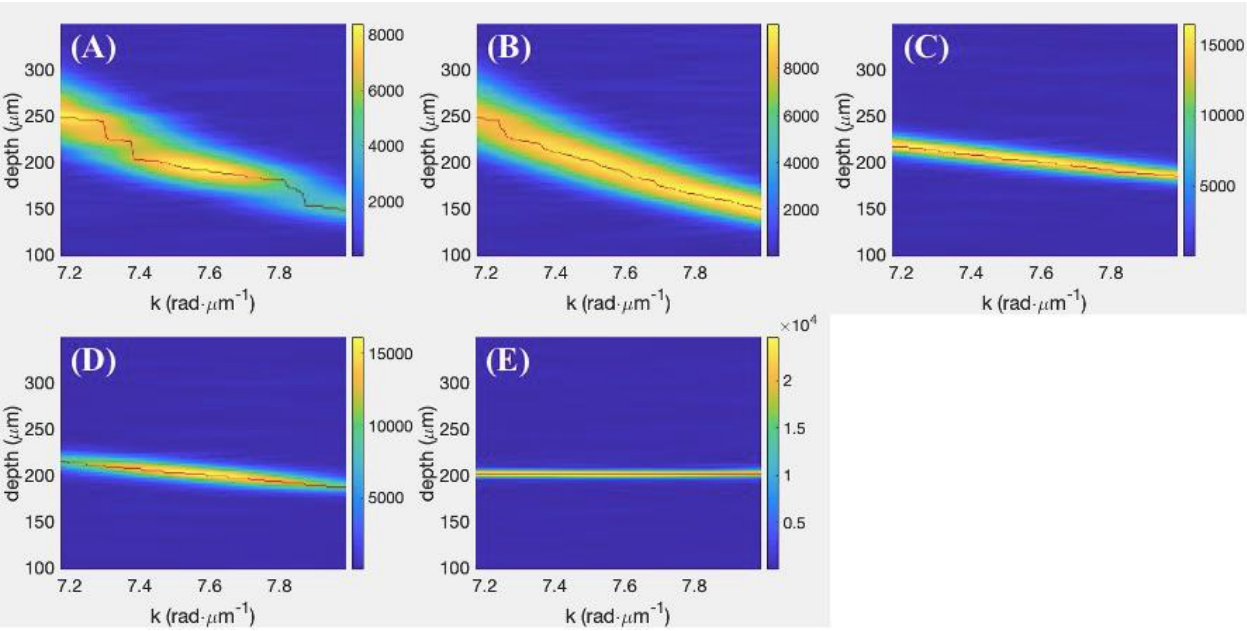

Figure S3.3.1. STFT of a mirror's spectral interferogram with (A) background subtraction, (B) normalization to reference spectrum, (C) resampling, (D) windowing, and (E) the proposed dispersion compensation. The color bar indicates the amplitude of the STFT.

The spatial-spectral plot provides direct access to the two-dimensional representation of the step-by-step signal processing of a spectral interferogram of a single reflection of a mirror, which illustrates how the spectral non-linearity and mismatch between the two arms changes over the entire image processing. The energy distribution is gradually changing as shown in Fig. S3.3.1A-E. The energy distribution band is downward sloping and locally concentrated at some k numbers after background subtraction (Fig. S3.3.1A), downward sloping and more uniformly distributed after normalization (Fig. S3.3.1B). The chirping issue was largely solved by the resampling step, but it still remained observable ridge variances (Fig. S3.3.1C). Therefore, our algorithm is applied to the resampled spectral interferograms to further extract the underlying dispersion that causes these ridge variances along the k-axis. To avoid unnecessary spectral leakage effects, a Hann

window was used to suppress the fringe signals at two ends (Fig. S3.3.1D). Little ridge variance was observed after the proposed dispersion compensation (Fig. S3.3.1E).

Appendix 5.1: A Brief Introduction to Bingham-Papanastasiou Model

The Bingham plastic model is widely used to describe the behavior of viscoplastic fluids, wherein deformation only occurs once a minimum yield stress τ_y is exceeded [172, 194].

$$\tau = \tau_y + \eta_p \dot{\gamma} \quad \text{(S5.1.1)}$$

Or equivalently,

$$\eta_a = \begin{cases} \infty, & |\tau| \leq \tau_y \\ \eta_p + \dfrac{\tau_y}{\dot{\gamma}}, & |\tau| > \tau_y \end{cases} \quad \text{(S5.1.2)}$$

where η_a is the apparent viscosity defined as the shear stress $\boldsymbol{\tau}$ applied to a fluid divided by the shear rate $\dot{\gamma}$. Additionally, η_p denotes the plastic viscosity, which corresponds to the viscosity of a fluid under infinite shear rate conditions. It specifically characterizes the portion of the overall viscosity of a non-Newtonian fluid that accounts for its internal friction. If the applied stress does not exceed the minimum yield stress, the apparent viscosity of the 'fluid' tends towards infinity, indicating the absence of fluid movement and solid-like behavior.

To facilitate computations in both the yielded and unyielded regions, the Papanastasiou continuous regularization method is employed for the viscosity function. It is represented by the equation [170]:

$$\eta_a = \eta_p + \frac{\tau_y}{\dot{\gamma}}\left(1 - e^{-m_p \dot{\gamma}}\right) \quad (S5.1.3)$$

where m_p is a material parameter that governs the exponential growth of stress, with a relatively high exponent m_p, enabling rapid stress growth at relatively low shear rates [170].

Appendix 5.2: A Simplified Physical Model Using Free Body Diagram

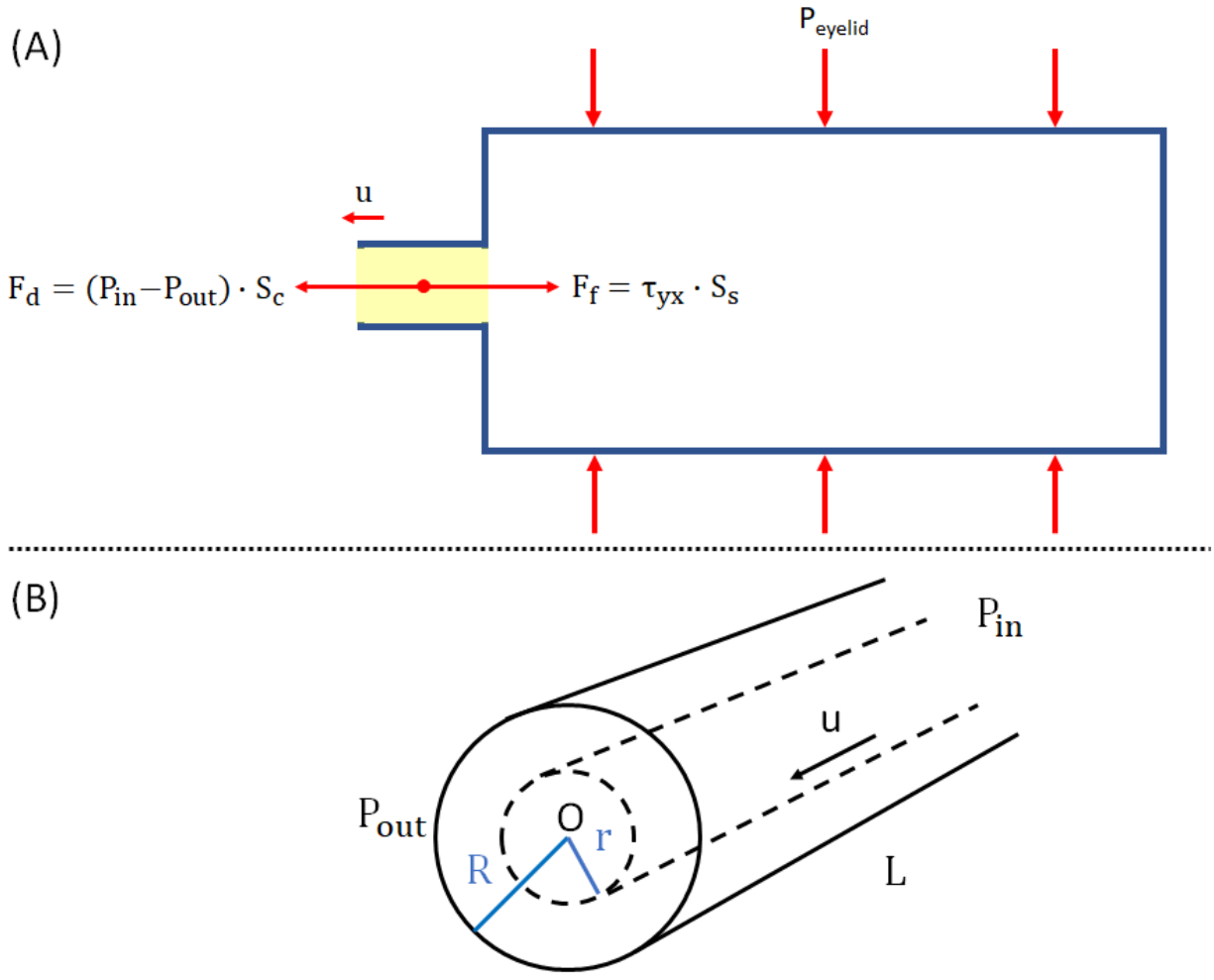

Fig. S5.2.1 Free-body diagram of the meibum within the terminal duct of the meibomian gland. Panel A depicts a 2D profile of the entire gland, while panel B provides a 3D illustration of the terminal duct only. The meibum flow occurs at a velocity u through the terminal duct, characterized by its radius R and length L. At equilibrium, the driving force F_d equals the frictional force Ff caused by the viscous meibum (A). For the detailed mechanical analysis of the meibum, a specific region of interest with a variable radius r is selected within the terminal duct of the gland (B).

To ensure comprehensive coverage in this paper, we also endeavored to derive expressions for meibum flow rate and the required eyelid pressure as functions of viscosity (refer to Fig. S5.2.1). This analysis enhances our understanding of the underlying mechanisms behind MGD, which are in line with the conclusions drawn from the simulation studies. Note that the following derivations were similar to the derivation of Poiseuille's law, which can be found in [172], but we have taken a more comprehensive approach considering the non-Newtonian flow of meibum through the glandular system.

A free body diagram is employed to analyze the meibum within the terminal duct, as depicted in Fig. S5.2.1A. To accomplish this, a specific region of interest (indicated by the dashed line) is selected, encompassing a length of L and a radius of r within the central portion of the terminal duct, as illustrated in Fig. S5.2.1B. The driving force responsible for squeezing out the meibum is determined by the product of the pressure reduction and the cross-sectional area of the selected region within the terminal duct:

$$F_d = (P_{in} - P_{out}) \cdot S_c' \quad (S5.2.1)$$

Here, $S_c' = \pi r^2$, and it should be noted that r is a variable representing the integral path starting from the origin O (r = 0) to the boundary of the duct (r = R). P_{in} and P_{out} refer to the pressures at the start of the terminal duct and the surrounding atmosphere, respectively.

To account for the presence of the orifice in the meibomian gland, a correction factor is introduced, resulting in the following equation:

$$P_{in} = \alpha \cdot P_{eyelid} \quad (S5.2.2)$$

where α represents the correction factor that reflects the pseudo 'enclosed' nature of the system. The range of α lies between 0 and 1, with α = 1 indicating perfect pressure transduction according to Pascal's law in an enclosed system. Values other than 1 indicate a reduction in pressure transduction from the central gland's wall to the terminal duct. It should be noted that there may be other factors contributing to pressure reduction. For instance, as the meibum enters a narrower constriction in the terminal duct, its velocity increases in accordance with the continuity of volumetric flow rate, resulting in a decrease in pressure due to Bernoulli's principle [172]. Additionally, the viscosity of meibum causes an additional pressure drop along the flow direction from the acini and central ducts to the terminal duct, which is directly proportional to the distance traveled.

On the other hand, the frictional force, denoted as F_f, is calculated by multiplying the shear stress τ_{yx} with the lateral surface area of the selected region within the terminal duct ($S_s = 2\pi rL$).

$$F_f = \tau_{yx} \cdot S_s \quad \text{(S5.2.3)}$$

The shear stress can be expressed as follows [172]:

$$\tau_{yx} = \tau_y - \eta_p \frac{du}{dr} \quad \text{(S5.2.4)}$$

It should be noted that the negative sign in the term $-\eta_p \frac{du}{dr}$ is due to the fact that the velocity gradient $\frac{du}{dr}$ is negative.

For a steady state flow, the driving force is equal to the frictional force caused by the viscous meibum, which can be expressed as:

$$F_d = F_f \quad (S5.2.5)$$

By combining Eqs. S5.1.1-S5.1.3, S5.2.1-S5.2.5, we obtain the following differential equation:

$$du = \frac{\tau_y}{\eta_p} dr - \frac{\alpha P_{eyelid} - P_{out}}{2\eta_p L} r dr \quad (S5.2.6)$$

Integrating both sides of Eq. S5.2.6 yields:

$$u = \frac{\tau_y}{\eta_p} r - \frac{\alpha P_{eyelid} - P_{out}}{4\eta_p L} r^2 + C \quad (S5.2.7)$$

where C is a constant that needs to be determined. Considering the no-slip conditions at the boundaries:

$$u|_{r=R} = \frac{\tau_y}{\eta_p} R - \frac{\alpha P_{eyelid} - P_{out}}{4\eta_p L} R^2 + C = 0 \quad (S5.2.8)$$

Therefore, C can be calculated as $\frac{(\alpha P_{eyelid} - P_{out})R^2}{4\eta_p L} - \frac{\tau_y R}{\eta_p}$. Finally, the complete analytical solution for the flow velocity as a function of r is given by:

$$u = \frac{\alpha P_{eyelid} - P_{out}}{4\eta_p L}(R^2 - r^2) - \frac{\tau_y}{\eta_p}(R - r) \quad (S5.2.9)$$

In Eq. S5.2.9, the flow velocity consists of two components: a parabolic term and a linear term. The parabolic term is reminiscent of the velocity profile observed in steady-state, laminar, incompressible flows of Newtonian fluids, characterized by a parabolic shape. The linear term, on the other hand, is attributed to the non-Newtonian properties of the fluid, causing deviations from the typical parabolic profile.

We further calculated the flow rate Q to examine how the proposed mechanisms would explain the cause of obstructive MGD. The average velocity can be determined by performing an integration across the cross-sectional area of the duct:

$$\bar{u} = \frac{1}{\pi R^2}\int_0^R 2\pi r u \, dr = \frac{(\alpha \cdot P_{eyelid} - P_{out})R^2}{8\eta_p L} - \frac{\tau_y R}{3\eta_p} \quad (S5.2.10)$$

According to the flow rate definition by Eq. 5.2,

$$Q = \frac{\pi(\alpha \cdot P_{eyelid} - P_{out})R^4}{8\eta_p L} - \frac{\tau_y R}{3\eta_p} \quad (S5.2.11)$$

Notably, the first term on the right of Eq. S5.2.11 bears resemblance to Poiseuille's Law, which is typically applicable to steady-state, laminar, incompressible, Newtonian flows. However, our analysis of non-Newtonian meibum reveals that the second term also exerts a significant influence on both the flow behaviors. Based on Eq. S5.2.11, it is evident that the meibum flow rate positively correlates with the eyelid pressure, the fourth power of the duct radius, and inversely correlates with the minimum yield stress and plastic viscosity. These findings align with our modeling studies, which suggest that the force exerted by the eyelid, as well as hyperproliferation of the terminal excretory ductal epithelium and changes in the melting state of meibum from fluid to solid, can lead to dramatic decreases in meibum flow.

Finally, we derive the relationship between eyelid pressure and viscosity properties, as one would expect that increased viscosity would lead to a more challenging meibum expression. Rewriting Eq. S5.2.11, the pressure P_{eyelid} required by the eyelid muscle to squeeze out meibum can be expressed as:

$$P_{eyelid} = \frac{8\tau_y L}{3\alpha R} + \frac{8\eta_p Q L}{\alpha\pi R^4} + \frac{P_{out}}{\alpha} = C_1 \cdot \tau_y + C_2 \cdot \eta_p + C_3 \quad \text{(S5.2.12)}$$

Here, $C_1 = \frac{8L}{3\alpha R}$, $C_2 = \frac{8QL}{\alpha\pi R^4}$, and $C_3 = \frac{P_{out}}{\alpha}$ are constants that depend on various factors such as gland morphology, non-Newtonian fluid properties, and the flow rate of meibum secretion.

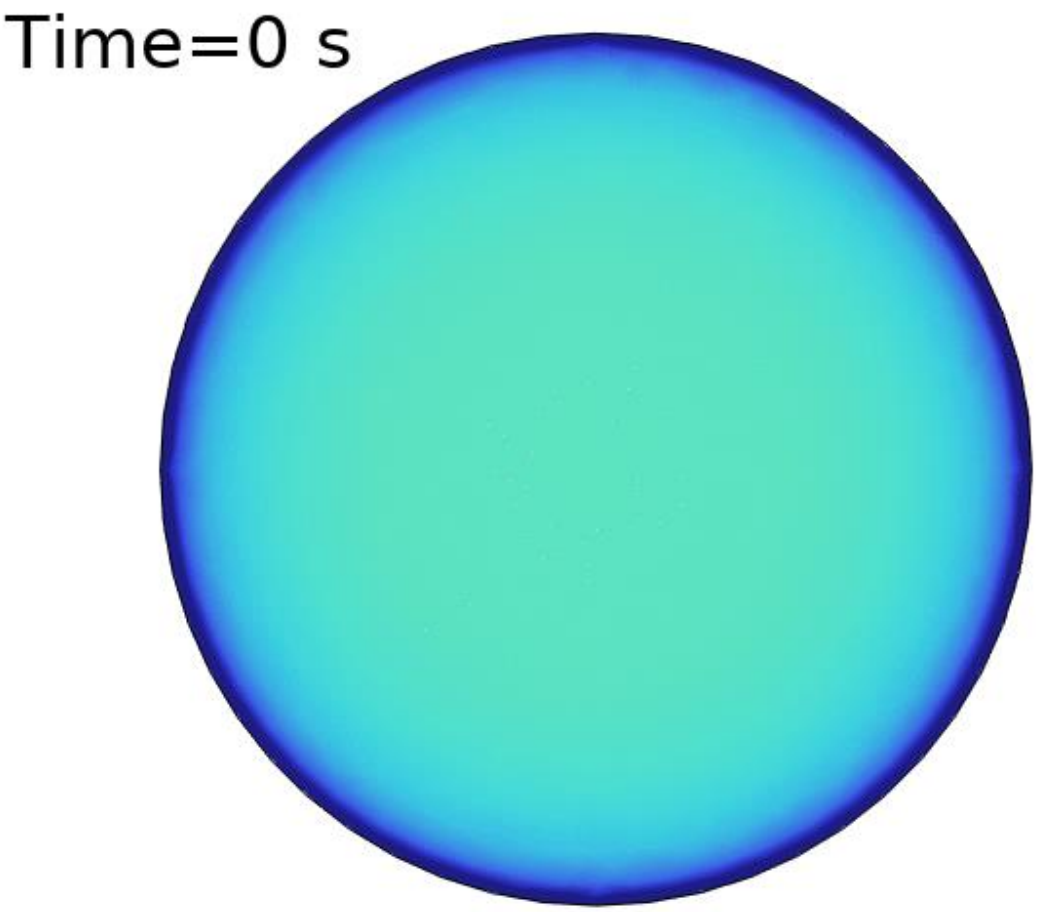

Video. S5.1 The meibum flow velocity observed during a typical blink period of 5 seconds demonstrates a significant increase in meibum expression during a blink that lasts approximately 1/3 of a second. The color bar is the same as in Fig. 5.5.